



UNIVERSIDADE D
COIMBRA

Susana Raquel Fonseca Castanheira

**STUDY OF THE SENSITIVITY OF THE LUX-
ZEPLIN DETECTOR TO THE DOUBLE ELECTRON
CAPTURE DECAY OF ^{124}Xe**

Dissertação no âmbito do Mestrado em Física, ramo de Física Nuclear e de Partículas orientada pelos Professores Doutores Alexandre Miguel Ferreira Lindote e Cláudio Frederico Pascoal da Silva e apresentada ao Departamento de Física da Faculdade de Ciências e Tecnologia.

Outubro de 2021

**Study of the sensitivity of the
LUX-ZEPLIN detector to the
double electron capture decay in
 ^{124}Xe**

Susana Raquel Fonseca Castanheira

A thesis submitted for the degree of
Master in Physics



Department of Physics
University of Coimbra
Portugal

October 2021

Abstract

The Standard Model (SM) of particle physics is an extremely successful theory which is capable of describing the vast majority of data from particle physics experiments. However, it fails to account for massive neutrinos bringing into question if neutrinos are Majorana or Dirac particles.

If neutrinos are Majorana fermions, then neutrinoless double beta decays would be a possible way of some isotopes to decay, although such decays violate the conservation of total lepton number. A first approach to understand the neutrinoless double beta decays is starting to study the two neutrino double beta decays. Therefore, in this work we study the double electron capture of ^{124}Xe with simulated data provided by the LUX-ZEPLIN experiment.

This experiment consists in 7 active tonnes of liquid xenon, monitored by a time projection chamber, in an ultra-low background environment due to the surrounding water shield and its underground placement. The LZ experiment will run for 1000 days.

A set of cuts is applied to the simulated data, which is then normalized to measured radioactivity levels or expected interaction rates in the detector in order to create the background model for this study. This model is then used to estimate the 90% CL sensitivity, observation and discovery potentials, for each decay mode of the double electron capture of ^{124}Xe , through the Rolke statistical approach. The LZ experiment is expected to reach the 3σ observation significance for the KK-mode after 13_{+8}^{-6} days, while for the KL-mode it takes 98_{+61}^{-47} days and reach a 5σ discovery for the KK and KL-mode after 38_{+22}^{-17} days and 275_{+172}^{-133} days, respectively. Given its low branching ratio, it is not expected that LZ will be able to observe the LL decay mode.

Keywords: Rare decays, Double electron capture, Xenon, LUX-ZEPLIN, Background Model, Sensitivity Projections.

Resumo

O Modelo Padrão da física de partículas é uma teoria extremamente bem-sucedida, pois consegue descrever a grande maioria dos dados provenientes de experiências de física de partículas. Contudo, este não tem em conta neutrinos massivos surgindo, assim, dúvidas sobre se os neutrinos são partículas de Majorana ou de Dirac.

Se os neutrinos forem fermiões de Majorana, então decaimentos beta duplos sem emissão de neutrinos seriam uma maneira viável de alguns isótopos decaírem. Contudo, tais decaimentos violam a conservação do número leptônico total. Uma primeira abordagem para compreender os decaimentos beta duplos sem emissão de neutrinos é começar por estudar os decaimentos beta duplos com emissão de dois neutrinos. Assim sendo, neste trabalho estudamos a captura eletrônica dupla do ^{124}Xe através de simulações geradas pela experiência de LZ.

Esta experiência consiste em 7 toneladas ativas de xénon líquido, monitorizadas por uma Câmara de Projeção Temporal, num ambiente de fundo ultrabaixo devido à blindagem que a água envolvente fornece e ao seu posicionamento debaixo de terra. O tempo de exposição da experiência de LZ será 1000 dias.

Um conjunto de cortes é aplicado aos dados simulados que, posteriormente, são normalizados em função dos níveis de radioatividade medidos ou das taxas de interação esperadas no detetor, a fim de criar o modelo de fundo para o presente estudo. Este modelo é então usado para estimar a sensibilidade com um intervalo de confiança de 90%, e os potenciais de observação e descoberta, para cada modo da captura eletrônica dupla do ^{124}Xe , através da abordagem estatística do Rolke. Espera-se que a experiência de LZ alcance uma significância de observação 3σ para o modo KK depois de 13_{-8}^{-6} dias, enquanto que para o modo KL demora 98_{+61}^{-47} dias e que alcance uma significância de descoberta 5σ para o modo KK e KL depois de 38_{+22}^{-17} dias e 275_{+172}^{-133} dias, respetivamente. Tendo em conta a sua baixa razão de ramificação, não se espera que a experiência de LZ seja capaz de observar o modo de decaimento LL.

Palavras-chave: Decaimentos raros, Captura eletrônica dupla, Xénon, LUX-ZEPLIN, Modelo de fundo, Projeções de sensibilidade.

Acknowledgements

First and foremost, i would like to thank my supervisors, Prof. Dr. Alexandre Lindote and Prof. Dr. Cláudio Silva, for their guidance, support, wise advices and patience throughout the conceiving of this thesis.

I would like to thank to my mother, my father, my sisters and my grandparents for all the support; a special thanks also to Henrique, whom has accompanied and helped me for the past years. I dedicate this thesis to my family, but especially to my grandfather António who I already miss a lot and almost saw me finish this step.

I also want to give a big thanks to the LIP Dark Matter Group for welcoming me so well helping me whenever I needed.

Contents

List of Figures	xi
List of Tables	xvii
List of Abbreviations	xix
1 General Introduction	1
2 Standard Model and Neutrino Physics	4
2.1 The Standard Model	4
2.1.1 Conserved quantities in the SM	6
2.1.2 Limitations of the SM	9
2.2 Neutrino Physics	9
2.3 Double Beta Decays	16
2.3.1 Half-life Calculations	26
3 The LUX-ZEPLIN Experiment	30
3.1 The LZ Detector	31
3.1.1 The Xenon Skin and Dual-Phase TPC	32
3.1.2 The Outer Detector	35
3.2 Particle Detection in liquid xenon	36
3.3 Monte Carlo Simulations of the LZ Detector	45
4 Signal and Background Models	50
4.1 Signal Model	50
4.2 Background Expectations	54

4.2.1	External Backgrounds	55
4.2.2	Internal Backgrounds	57
4.2.3	Irreducible Physical Background	62
4.3	Event Selection Criteria	63
5	Statistical analysis and discovery potential projections	73
5.1	The Rolke Method	73
5.2	Statistical Analysis of KK, KL and LL modes of ^{124}Xe Double Electron Capture	75
6	Conclusions	82
	References	84
A	Parameters of a root tree	103

List of Figures

2.1	Diagram of the elementary particles in the SM. The first, second, and third columns show the three generations of fermions, the fourth column shows the vector bosons, and the fifth column shows the Higgs boson. The quarks (purple) and leptons (green) make up matter, the gauge bosons (red) mediate the interactions among the elementary fermions and the Higgs Boson (yellow) gives mass to all particles.	5
2.2	Energy spectrum of the flux of the various neutrino sources, at earth, as a function of their energy. Figure from [38].	12
2.3	Two possible neutrino mass orderings. Left and right images show, respectively, the normal and inverted mass orderings and the neutrino masses increase from bottom to top. The electron, muon and tau flavour contents of each neutrino mass eigenstate are shown via the red, blue and green fractions, respectively. Figure from [44] . . .	16
2.4	Representation of the semi-empirical mass formula, for isobaric nuclei, as a function of the proton number, Z , for odd-odd and even-even mass number, A . An odd-odd nucleus has an odd number of neutrons and an odd number of protons, while, an even-even nucleus has an even number of neutrons and an even number of protons. This double parabola shows energetically possible single and double beta decays. Double beta decay is possible between (c) and (e) and also between (g) and (e). (c) can not decay for example to (d) because the mass of (d) is greater than of the (c). (e) has the lowest mass so is stable. Figure from [45].	18

2.5	Feynman diagram for the $2\nu 2\beta^-$ decay process. Diagram created with [46].	19
2.6	Feynman diagram for the $0\nu 2\beta^-$ decay process. Diagram created with [46].	20
2.7	Electrons energy spectrum for the $2\nu 2\beta^-$ and $0\nu 2\beta^-$ decays, represented by the number of expected events as a function of the electrons energy. Figure from [48].	20
2.8	Feynman diagram for the $2\nu 2EC$ decay process. Diagram created with [46].	21
2.9	Feynman diagram for the $0\nu 2EC$ decay process. Diagram created with [46].	22
2.10	Feynman diagrams for the $2\nu\beta^+ EC$ and $0\nu\beta^+ EC$ decay processes. Diagrams created with [46].	25
2.11	Feynman diagrams for the $2\nu 2\beta^+$ and $0\nu 2\beta^+$ decay processes. Diagrams created with [46].	26
2.12	Schematic representation of a general $0\nu 2EC$ decay. Figure from [68].	29
3.1	Location of the LZ experiment at the SURF in South Dakota. Figure from [76].	31
3.2	Schematic representation of the LZ detector. Figure from [77].	32
3.3	Section view of the TPC of LZ, with the liquid-gas interface region shown with more detail. Figure from [78].	33

3.4	Schematic illustration of the four high-voltage grids inside the TPC. The drift field, which pushes the ionized electrons to the top of the tank, is created by the cathode and gate grid. There, the electrons are extracted through a field created by the anode and gate grids. At the bottom of the tank, the shield grid protects the bottom PMT array from the high electric fields above. Figure from [80].	34
3.5	The four types of PMTs employed in the LZ experiment. The R11410-22 PMTs were assembled to view the scintillation light produced in the active region of the TPC, the R8520 and R8778 PMTs in the xenon skin and the R5912 PMTs in the water tank to view the OD scintillation light. Figures from [78, 80].	36
3.6	Basic schematic representation of the processes following an interaction in xenon, leading to the production of scintillation light and ionization electrons.	37
3.7	Representation of an interaction in the liquid xenon inside a dual-phase xenon TPC. Figure from [77].	38
3.8	Graphical representation of $\log_{10}(S2/S1)$ as a function of S1 photons detected for calibrations of the LUX detector response in the fiducial volume. The upper graphic, a), shows the ER calibration using tritium, and the bottom one, b), the NR calibration using mono-energetic neutrons from the D-D generator. The solid blue and red lines represent the ER and NR band means, respectively. The dashed blue and red lines represent the $\pm 1.28 \sigma$ contours for the ER and NR bands, respectively. The dot-dashed magenta line represents the S2 threshold in analysis. The gray lines are the contours of constant energy deposition for an ER, in units of kilo electron-volts electron-equivalent (keV_{ee}), or an NR, in units of kilo electron-volts nuclear-equivalent (keV_{nr}). See [89] for more details.	40

3.9	Graphical representation of the light yield (a) and charge yield (b) of the CH ₃ T events in LUX for two field strengths: 105 V/cm and 180 V/cm which are represented by the blue and black squares, respectively. The blue and grey bands indicate the 1σ systematic uncertainties on the data, while the statistical uncertainties are negligible in comparison. NEST is a package which provides a model for the scintillation light and ionization charge yields as a function of electric field and energy or stopping power [96]. The NEST predictions for the 105 V/cm and 180 V/cm are shown the green dashed and solid red lines. Figure from [95].	44
3.10	Representation of the LZ detector in BACCARAT. The water tank, instrumented with the PMTs, is shown in blue. On the inside of the water tank, the gadolinium loaded organic liquid scintillator OD is shown in yellow, the cryostat in light green and the innermost part, the TPC, is shown in magenta. Figure from [93].	45
3.11	NEST predictions of the light (a) and charge (b) yield of ER interactions in several field strengths. Figure from [99].	47
3.12	NEST predictions of the light (a) and charge (b) yield of an NR interaction in several field strengths. Figure from [99].	48
3.13	The two possible processing chains for the simulations used to obtain the sensitivity analyses and also the fake dataset used in the Mock Data Challenges. Figure from [93].	49
4.1	Decay scheme of ¹²⁵ I. Figure from [122].	59
4.2	Rate of the several sources of neutrinos that interact in xenon via the elastic scattering with electrons. The main contribution comes from the pp reaction, ⁷ Be and CNO chain. These event rates were calculated assuming that the electrons are free. Binding effect corrections are only relevant at very low energy, and in this study would effect only the LL decay mode. Figure from [139].	63
4.3	Total background and individual components in the region of interest.	65

4.4	Decay scheme for ^{214}Pb , (a), and ^{212}Pb , (b).	67
4.5	Graphical representation of the background coming from the ^{222}Rn chain depending on the quadratic radial direction, R^2 , vs the vertical direction, z . The effects of applying the single scatter and veto cuts are visible in subfigures b)-e). Note the significant reduction in the (z) color scale with the successive application of the cuts. The fiducial volume cut is represented by the red dashed line.	68
4.6	Decay scheme for ^{85}Kr	69
4.7	Spatial disposition of all ER backgrounds which survived to the single scatter and also the veto cuts, with energies up to 100 keV. The dashed black line represents the fiducial volume. Figure from [141].	70
4.8	Effect of applying successive analysis cuts.	71
4.9	Total background and individual components.	72
5.1	Gaussian distribution of the required number of signal events to claim a discovery of the LL-mode, for 75 days of exposing.	75
5.2	Energy resolution as a function of the energy for the LUX (blue) [145] and XENON1T (red) detectors. Uncertainties in the XENON1T data are statistical only and thus too small to be seen. The full black line corresponds to a fit using XENON1T data points with $\frac{a}{\sqrt{E}} + b$, where $a=(31.3\pm 0.7)$ and $b=(0.17\pm 0.02)$ [144]. The purple, blue and green dashed lines represent the expected energy peak of the LL-mode, the KL-mode and the KK-mode of the double electron capture of ^{124}Xe , respectively.	76

5.3	Event rate of the expected signals for the LL, KL and KK modes represented by the solid blue, pink and green lines, respectively. The vertical blue, pink and green dashed lines illustrate the 2σ energy windows. The horizontal black solid line represents the total expected spectrum, including all the background sources and the decay modes for the double electron capture of ^{124}Xe	77
5.4	The blue, green and red lines represent the evolution of the 90% CL sensitivity, (3σ) observation potential and (5σ) discovery potential, respectively, for the KK-mode over the exposure time of LZ. The blue, green and red bands represent the $\pm 1\sigma$ uncertainty for the sensitivity, observation and discovery potentials, respectively. The half-life for the KK-mode, measured by XENON1T, is represented by the dashed black horizontal line and the respective uncertainty by the gray shaded area.	79
5.5	The blue, green and red lines represent the evolution of the 90% CL sensitivity, (3σ) observation potential and (5σ) discovery potential, respectively, for the KL-mode over the exposure time of LZ. The blue, green and red bands represent the $\pm 1\sigma$ uncertainty for the sensitivity, observation and discovery potentials, respectively. The expected half-life for the KL-mode, obtained from the XENON1T measurement of the KK-mode [106] with $f_x = 0.23$, is expressed by the dashed black horizontal line and the respective uncertainty, obtained through Equation 5.2, by the gray shaded area.	80
5.6	The blue, green and red lines represent the evolution of the 90% CL sensitivity, (3σ) observation potential and (5σ) discovery potential, correspondingly, for the LL-mode over the exposure time of LZ. The blue, green and red bands represent the $\pm 1\sigma$ uncertainty for the sensitivity, observation and discovery potentials, respectively. The expected half-life for the LL-mode, obtained from the XENON1T measurement of the KK-mode [106] with $f_x = 0.017$, is expressed by the dashed black horizontal line and the respective uncertainty, obtained through Equation 5.2, by the gray shaded area.	81

List of Tables

2.1	The fundamental forces in particle physics with the fermions they act on and the gauge bosons that mediate the forces.	6
2.2	Neutrino mixing parameters according to the most recent oscillation analysis by González-García where $\Delta m_{3i}^2 \equiv \Delta m_{31}^2$ for the normal ordering and $\Delta m_{3i}^2 \equiv \Delta m_{32}^2$ for the inverted one. Table from [42]. .	17
2.3	The phase-space factors, the expected matrix elements (according to the assumptions presented in Equation 2.25) and the measured or predicted half-lives for the $2\nu 2EC$, $2\nu EC\beta^+$ and $2\nu 2\beta^+$ decay modes of ^{124}Xe . The half-lives were predicted based in the measured half-life of ^{124}Xe $2\nu 2EC$ decay, by XENON1T, and according to Equations 2.26 and 2.27. Each phase-space factor is presented in a range of values, since in [67] there is a collection of different values obtained with different methods for each one. The half-lives of the decay modes $2\nu EC\beta^+$ and $2\nu 2\beta^+$ were predicted using the central value of this range and for the uncertainty it was used half of this range. Table from [61].	27
3.1	LZ Calibration sources, their deployment mode, interaction type and energy lines (or range).	43
5.1	Expected counts in the different regions of interest, for the three different decay modes, of the main background sources. The presented counts corresponds to a 1000 days of exposure of the LZ experiment in the 5.6 tonnes fiducial volume. All the analysis cuts, described in the Section 4.3, have already been applied to the counts of each background source.	78

A.1 List of the variables and the respective type, units and meaning, of a root tree.	103
--	-----

List of Abbreviations

BACCARAT Basically A Component-Centric Analog Response to AnyThing

CL Confidence level

DAQ Data Acquisition

DER Detector Electronics Response

ER Electron Recoil

HPGe High Purity Germanium

ICP-MS Inductively-Coupled Plasma Mass Spectrometry

LAB Linear Alkylbenzene

LUX Large Underground Xenon

LZ LUX-ZEPLIN

LZap LZ Analysis Package

NAA Neutron Activation Analysis

NEST Noble Element Scintillation Technique

NR Nuclear Recoil

OD Outer Detector

PHE Photoelectron

PMT Photomultiplier Tube

PTFE Polytetrafluoroethylene

SM Standard Model

SURF Sanford Underground Research Facility

TPC Time Projection Chamber

VUV Vacuum-ultraviolet

Chapter 1

General Introduction

The SM of particle physics, which describes the fundamental particles and their interactions, is one of the most successful theories in physics.

In the SM there are seventeen named fundamental particles organized in two groups, the fermions and the bosons, the latter being the carriers of the four fundamental forces. The fermion sector in the SM includes all quarks and leptons. Quarks come in six different types, known as flavours: up, down, charm, strange, top, and bottom. Leptons are divided into two main classes: the charged leptons (electrons, muons and taus) and the neutral ones (electron-neutrinos, muon-neutrinos and tau-neutrinos).

Neutrinos, as far as we know, are observed to be only left-handed, which would result in neutrinos being massless. This is not the case since, in 1998, the Super-Kamiokande collaboration announced the observation of oscillations between neutrino flavours, the first evidence that neutrinos have a tiny but not zero mass.

The incompatibility between the observation that only left-handed neutrinos participate in weak interactions and their flavour oscillation could be solved if instead of trying to build a Dirac mass term we build a Majorana one. A Dirac mass term assumes that the neutrino and the anti-neutrino are distinct particles, while a Majorana one presumes that the neutrino and the anti-neutrino are the same particle. Since the neutrino is electrically neutral, there is always the possibility that it might be a Majorana particle, which would imply the existence of a right-handed neutrino.

At the same time, the existence of Majorana neutrinos opens the possibility of the occurrence of decays where the conservation of the total lepton number is violated. Even though this is an accidental symmetry in the SM, decays where the total lepton number is not conserved have never been observed.

One of the interesting channels in which the total lepton number is violated is the neutrinoless double electron capture of ^{124}Xe due to its potential detectability via resonant enhancement. The resonance effect can occur when, during the captures, the released mono-energetic photon has an energy equals to the 2P-1S transition or when there is a mass degeneracy between the initial and the final (excited) nucleus. The half-life of the double electron capture can be enhanced up to six orders of magnitude and it also has a unique signature. The expected signal experimental signature is a coincidence de-excitation of the atomic shell and nucleus, making it easier to discriminate between background and the signal.

In this thesis, we study the two neutrino double electron capture ($2\nu 2EC$) of ^{124}Xe in the LUX-ZEPLIN (LZ) experiment, since studying the two neutrino modes of double beta decays is an asset to understand the neutrinoless ones. Moreover, it is also very useful to compare the experimental data of the $2\nu 2EC$ decay with theoretical predictions of the current nuclear models and analyze its accuracy; to contribute to the calculation of nuclear matrix elements of proton-rich elements, and to evaluate the accuracy of the current nuclear models.

The LZ experiment, installed 1478 m underground at the Sanford Underground Research Facility (SURF) in Lead (USA), consists in a dual-phase (liquid-gas) time projection chamber (TPC) loaded with 7 tonnes of liquid xenon, which is surrounded by a large water tank for shielding against environmental radiation. In order to ensure that unwanted events are not misread as the actual searched signals, the TPC is surrounded by an additionally layer of xenon, which sits inside an outer detector (OD) filled with liquid scintillator. The water tank is instrumented with several arrays of photomultiplier tubes (PMTs) in order to veto false signals by looking at these two veto systems. The decay we are studying, the double electron capture of ^{124}Xe , is an extremely rare decay and thus the low background environment provided by the LZ detector is essential.

The $2\nu 2EC$ decay has three main modes depending on the shells from which the electrons are captured. The most probable is the KK-mode, with both electrons being captured from the K shell, followed by the KL-mode (one electron from the K shell and the other from the L shell) and, the least likely, the LL-mode with both electrons being captured from the L shell. So far, only for one, the most probable, of these three modes was it possible to measure the half-life. The current most accuracy value of the $2\nu KK$ half-life is $T_{1/2} = (1.8 \pm 0.5_{stat} \pm 0.1_{sys}) \times 10^{22}$ years, with a significance of 4.4σ , and was measured by XENON1T.

In this analysis, we use simulated data to which we apply realistic analysis cuts in order to minimize the background in the region of interest of each of these decay modes, and then we use the frequentist statistical approach of Rolke to determine the 90% C.L. sensitivity, as well as the (3σ) observation and (5σ) discovery potentials of LZ to each mode.

This thesis is divided into six chapters. Chapter 2 covers a theoretical introduction that addresses the SM of particle physics, neutrino physics and finally double beta decays. Next, in chapter 3, we introduce the LZ experiment by showing the detector structure, the physics behind the detection of signals in the xenon, and also describe the employed Monte Carlo simulations. Chapter 4 presents the analysis of the double capture of ^{124}Xe , starting by the signal model, the expected background events and finally the analysis cuts applied in the simulations in order to reduce the background as much as possible. Chapter 5 discusses the statistical approach used to obtain the sensitivity, observation and discovery potentials of each decay mode. Finally, chapter 6 presents the final conclusions of this work.

Chapter 2

Standard Model and Neutrino Physics

2.1 The Standard Model

The SM of particle physics is the current description of the fundamental constituents of the universe and interactions between them. It is a gauge theory based on the gauge group $SU(3) \times SU(2) \times U(1)$ [1] where all elementary particles are arranged in irreducible representations of this gauge group. Its framework unifies the description of the electromagnetic and weak interactions, combined in an electroweak interaction, and the strong interaction [2]. Electroweak interaction governs radioactive decays and electromagnetism, with an associated $SU(2) \times U(1)$ gauge symmetry [2], while the strong interaction is responsible for binding the quarks together, that make up hadrons, and also holds together atomic nuclei.

A summary of the particle content of the SM is given in Figure 2.1. In the SM the fundamental particles are grouped into fermions, spin $\frac{1}{2}$ particles obeying Fermi-Dirac statistics [3], and the force carrier particles that have an integer spin and are called bosons, obeying Bose-Einstein statistics [3]. Bosons with spin 1 are called vector bosons while those with spin 0 are called scalar bosons, like the Higgs particle. The fermion sector is organized in three generations [4]. Each one includes two quarks, which interact through the strong force and so they have color charge, and two leptons, which do not have color. Therefore, there are 6 quarks

and 6 leptons, plus their antiparticles.

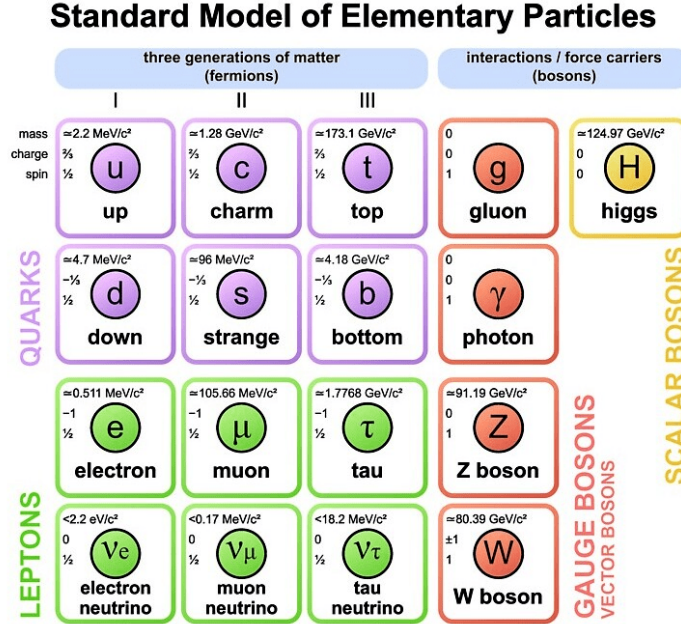


Figure 2.1: Diagram of the elementary particles in the SM. The first, second, and third columns show the three generations of fermions, the fourth column shows the vector bosons, and the fifth column shows the Higgs boson. The quarks (purple) and leptons (green) make up matter, the gauge bosons (red) mediate the interactions among the elementary fermions and the Higgs Boson (yellow) gives mass to all particles.

The interactions are modeled by the exchange of bosons. For instance, the electromagnetic interaction is described by the exchange of photons, the strong interaction by the exchange of gluons, and the weak interaction by the exchange of massive vector bosons [5]. Table 2.1 summarizes the three fundamental forces, its mediators, and each of the particles they interact with.

By construction, the bosons and fermions in the SM are massless. However, from observations, we know that many of the particles in the SM do have masses. Therefore, the SM also includes a mechanism for generating these masses through a process known as the Higgs mechanism, where the masses arise due to interactions with a Higgs field with a non-zero vacuum expectation value [6]. The stronger the coupling between a particle and the Higgs field, the more massive that particle is.

Table 2.1: The fundamental forces in particle physics with the fermions they act on and the gauge bosons that mediate the forces.

Force	Works on	Mediated by
Strong	Quarks	g
Electromagnetic	Charged leptons	γ
Weak	Quarks	W^\pm, Z^0
	Charged leptons	
	Quarks	
	Neutrinos	

One important property of particles undergoing weak interactions is their chirality. The weak force only interacts with left-chiral particles or right-chiral antiparticles [7].

The chirality property indicates how the quantum mechanical wave function of a particle behaves when the particle is rotated and is intrinsic to each particle. By contrast, the weak force interacts with both left and right helicity particles.

A particle has a right-handed helicity if its spin points in the direction of its momentum, while it has a left-handed helicity if its spin points in the opposite direction of its momentum. Therefore, the helicity is not an inherent property of a particle because it depends on the choice of the reference frame relative to the particle. However, regardless of the choice of reference frame, the particle will still have the same chirality. In the limit of massless particles, the helicity coincides with the chirality because massless particles travel at the speed of light and so it is impossible to boost the reference frame.

2.1.1 Conserved quantities in the SM

In the SM, specific quantities are conserved in certain processes. Each lepton generation has an associated quantum number called lepton number. Therefore, there are four different lepton numbers: the electron-lepton number, L_e , the muon-

lepton number, L_μ , the tau-lepton number, L_τ , and the total lepton number, L .

The electron-lepton number is +1 for electrons and electron neutrinos and -1 for their antiparticles; Identically, the muon-lepton number is +1 for the muons and muon neutrinos and -1 for their antiparticles; Lastly, the tau-lepton number is +1 for the taus and tau neutrinos. Other non-leptonic particles have a 0 lepton number.

The conservation of the total lepton number, the number of leptons minus the number of antileptons, is based on experiments and observations. Since no violation has been observed so far, this conservation law is included in the SM as an empirical fact. According to Noether's theorem, every symmetry leads to a conservation law, but no symmetry associated with the conservation of the total lepton number has been discovered yet [8].

Moreover, it is impossible to write a gauge invariant, renormalizable operator in the Lagrangian that breaks the conservation of total lepton number, it is an accidental symmetry of the SM [9]. The value of each lepton number was also believed to be individually conserved until its violation was observed in neutrino oscillations [10]. Even though neutrino oscillations do not conserve individual lepton numbers, the total lepton number is still conserved [11].

Another conserved quantity in the SM is the baryon number, requiring that the total baryon number of a reaction is the same before and after the reaction occurs. Each baryon has a baryon number $B=1$, their antiparticles have $B=-1$ and all mesons have $B=0$. This can be interpreted as assigning to each quark, q , a baryon number of $B=\frac{1}{3}$ and each antiquark, \bar{q} , $B=-\frac{1}{3}$ [12]. Thus, the baryon number is defined by:

$$B = \frac{N(q) - N(\bar{q})}{3}, \quad (2.1)$$

where $N(q)$ is the number of quarks and $N(\bar{q})$ is the number of antiquarks.

Since all mesons are composed of an equal number of quarks and antiquarks their baryon number is always $B=0$. For the strong and electromagnetic forces, it is also required that each quark number is conserved, which means that the strong and electromagnetic forces can only create quark-antiquark pairs of the same flavour. The weak force can violate quark number, but not baryon number.

Similarly to the conservation of the total lepton number, the conservation of baryon number is accidental, and does not have an associated known symmetry [9].

The helicity of any particle can be reversed through a parity transformation. In spherical coordinates, parity transformation corresponds to $r \rightarrow r$, $\theta \rightarrow \pi - \theta$, $\phi \rightarrow \pi + \phi$. It is defined as a spatial inversion around the origin.

Therefore, a parity transformation transforms the helicity of a particle from left-handed into right-handed, and vice versa, by reversing the momentum while the angular momentum and spin remain the same. For most interactions reversing the spatial coordinates makes no fundamental differences to the interaction.

Parity symmetry is conserved in electromagnetism, strong interactions and gravity but not in weak interactions. As already said, the chirality property is a Lorentz invariant quantity so a left-chiral particle is not transformed into a right-chiral particle through parity transformations. Thus, the chiral identity of weak interactions provides a means for the parity violation [13].

Weak interactions are mediated by the W^+ , W^- and Z^0 bosons. Two different types of interactions can occur considering which boson is mediating the interaction. The W^+ and W^- bosons mediate the charged current interactions, in which the interacting particles form a current with a nonzero total electric charge, and the Z^0 boson mediates neutral current interactions where the formed current has a zero electric charge [14].

The parity violation in weak interactions was first theorized by Lee and Yang [15]. In 1956, while studying the radioactive decay of ^{60}Co , in Wu's experiment, it was first observed the parity violation in the charged current interactions [16]. Then, the parity violation of neutral charge current interactions was discovered by Charles Prescott, in 1978, while studying the scattering of electrons from protons in a liquid deuterium target [17].

Finally, some conserved quantities such as energy, angular momentum, electric charge, among others, are so well established that the SM is already built to obey them automatically.

2.1.2 Limitations of the SM

Even though the SM successfully describes the fundamental particles and their interactions, until the TeV scale, it can not be a complete description of the inner workings of nature because there are still some observed phenomena that are not accounted for in the SM. In fact, the SM still has several unanswered questions:

- Does not provide a viable dark matter candidate [18] (even though dark matter is estimated to be about 27% [19] of the total mass-energy content of the universe);
- Does not incorporate gravity [20];
- Does not unify the four fundamental forces (gravity, weak force, electromagnetism and strong force) [20];
- Does not explain the observed matter-antimatter asymmetry in the universe [18];
- Can not incorporate massive neutrinos (which are essential to describe the observed neutrino oscillations, a lepton flavour violating process not allowed in the SM) [18].

That being said, even though the SM describes the nature extremely well, it must be extended in order to be a theoretical model completely consistent with observations.

2.2 Neutrino Physics

Neutrinos were first postulated by Wolfgang Pauli in 1930, in order to explain the observed continuous energy spectrum of the electrons emitted in beta decays and to solve the spin statistic problem [21]. The spin-statistics theorem specifies which statistics a particle obeys depending on its intrinsic spin. Particles with half-integer spin obey Fermi-Dirac statistics while integer spin particles Bose-Einstein statistics [22].

At the time there was, in some atoms, an incongruence between the expected and observed statistics that they obeyed. For instance, as mentioned in Pauli's

letter of the 4th of December 1930, ^{14}N (which from the point of view of the old electron-proton model is a bound state of 14 protons and 7 electrons and thus would have a half-integer spin) was expected to obey the Fermi-Dirac statistics [21]. Since following the Pauli exclusion principle, which says that two identical fermions can not be in the same quantum state, the spin of the nucleus have to be half-integer [23]. However, ^{14}N obeys Bose-Einstein statistics. Therefore, Pauli suggested that in addition to electrons and protons an unknown neutral particle, very light with spin $\frac{1}{2}$ also constitutes the nuclei so that the spin is integer.

Later, in 1934, neutrinos were labeled as such by Enrico Fermi who made them the basis of his theory of weak interactions. Since the beginning, it was very clear that these particles would be very difficult to observe taking into account the smallness of their cross section (for neutrinos with energies of a few MeV $\sigma \approx 10^{-44}\text{cm}^2$). However Frederick Reines and Clyde Cowan convincingly proved their existence [24] through the observation of the inverse beta decay process (Equation 2.2) of the interaction of electron antineutrinos from reactors with protons in the detector



In 1988, muon neutrinos were discovered [25] by the Nobel prize winners Leon M. Lederman, Melvin Schwartz and Jack Steinberger. The discovery of tau lepton implied the existence of the third neutrino, the tau neutrino, although its existence was just proven in 2000 by the DONUT collaboration [26].

There are many neutrino sources in the Universe, either terrestrial or extraterrestrial. Terrestrial neutrinos can come from both natural sources, in the form of geoneutrinos, or artificial sources, such as nuclear reactors and particle accelerators. There are three different extraterrestrial neutrino sources: neutrinos from the Sun, from astrophysical objects and relic neutrinos from the Big Bang. They can produce a huge amount of neutrinos in the form of solar neutrinos, atmospheric neutrinos, supernovae neutrinos, cosmological neutrinos and cosmogenic neutrinos.

- The solar neutrinos are produced through the nuclear fusion process in the core of Sun. The evolution, activity and processes inside the Sun are well

described by the Standard Solar Model, which was mainly developed by John Bahcall [27, 28]. Solar neutrinos are mainly produced in the pp chain, in which two protons form deuterium with positron and electron neutrino emission, and in the CNO chain, in which electron neutrinos are released when four protons fuse using either carbon, nitrogen or oxygen as catalysts [29].

- The atmospheric neutrinos come from the interaction of cosmic-rays in the upper atmosphere [30]. These interactions result in pions and kaons which decay into muons and muon neutrinos. A vast majority of the muons also decay into electrons and pairs of muon electron neutrinos.
- Supernovae events are one of the most energetic events occurring in our universe and which produce incredible amounts of neutrinos and antineutrinos in all three flavours. They are generated through the thermonuclear explosion of white dwarfs and in the core collapse of massive stars [31].
- Cosmological neutrinos are the ones that were created in the early Universe, immediately after the Big Bang, and are the most intense natural neutrinos source. These relic neutrinos constitute the current cosmic neutrino background. The SM of cosmology predicts that neutrinos were in thermal equilibrium with protons, neutrons and electrons until they decoupled from the thermal bath, approximately one second after the Big Bang. Neutrinos decoupled when the temperature of the universe was ≈ 2 MeV, and have since redshifted to 10^{-4} eV [32]. Due to their extremely low energy and consequently their tremendously small cross section (in the order of 10^{-56} cm² to non-relativistic neutrinos and in the order of 10^{-63} cm² for relativistic neutrinos [33]), they are very difficult to detect because the detectors would need to have an extraordinarily low energy threshold.
- Cosmogenic neutrinos are generated by the photohadronic interactions of ultra-high energy cosmic rays (protons and heavy nuclei) with the cosmic microwave background and the extragalactic background light [34]. There is a minimum proton/heavy nuclei energy that can interact with the photon background to produce mesons that decay to gamma-rays and neutrinos.

- Geoneutrinos are electron antineutrinos that come from the beta decays of long lived radioactive elements present in the core of earth (^{238}U , ^{232}Th and ^{40}K) [35].
- Nuclear reactors and particle accelerators are human-made neutrino sources. In nuclear reactors, huge fluxes of antineutrinos are generated through nuclear fission reactions of heavy nuclei, usually ^{235}U . The resulting fragments have way too many neutrons which results in a series of alpha and beta decays into stable nuclei with a lower ratio of neutrons to protons [36]. In particle accelerators beams of protons are accelerated and collide with targets producing pions and kaons which subsequently decay emitting neutrinos [37]. Figure 2.2 [38] illustrates the flux and energy range of each neutrino source.

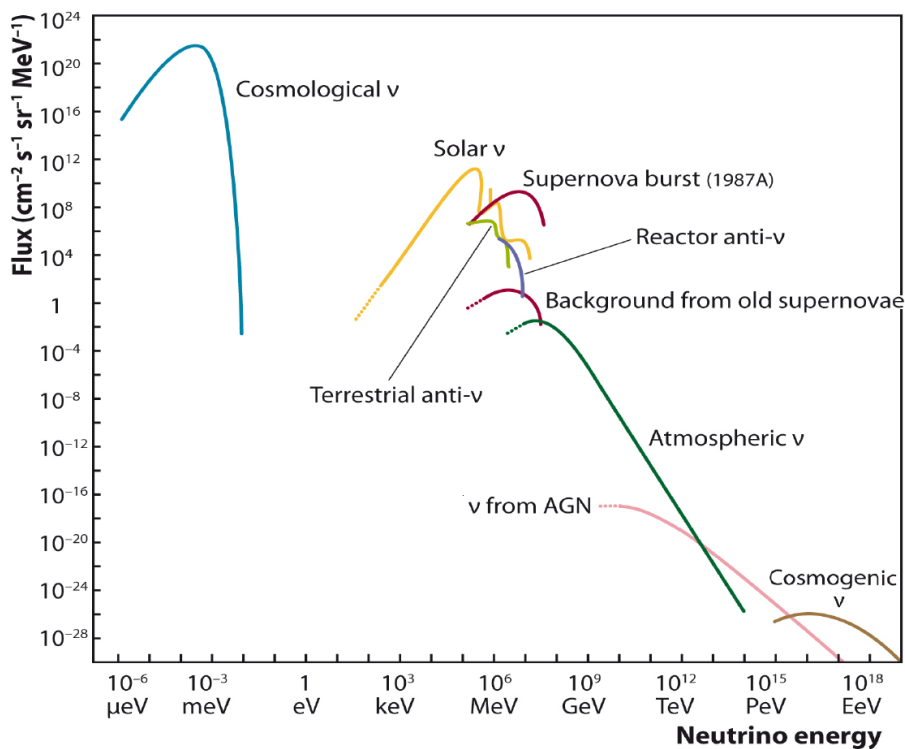


Figure 2.2: Energy spectrum of the flux of the various neutrino sources, at earth, as a function of their energy. Figure from [38].

In the SM, neutrinos were initially classified as massless particles since only left-handed neutrinos were observed. Being massless particles, neutrinos would travel

at the velocity of light [39]. It has also been stated that neutrinos are particles with spin $\frac{1}{2}$, and thus fermions, exclusively carrying weak charge. Therefore, they are not affected by the electromagnetic or the strong interaction, nor the gravitational force, only by weak interactions.

However, experimental observations of neutrino oscillations in atmospheric, solar and reactor neutrinos proved that at least two of the three neutrinos must have mass. Neutrino oscillations were first theorized by Maki, Nakagawa, and Sakata, in 1962 [40]. The observation of these flavour oscillations requires that all three masses involved can not be equal to each other.

The oscillation phenomenon arises because the neutrino flavour eigenstates ν_α are a superposition of its mass eigenstates ν_i

$$|\nu_\alpha\rangle = \sum_{i=1}^{N=3} U_{\alpha i}^* |\nu_i\rangle, \quad (2.3)$$

where $U_{\alpha i}$ is the Pontecorvo-Maki-Nakagawa-Sakata (PMNS) matrix [41, 42]

$$U_{\alpha i} = \begin{pmatrix} c_{13}c_{12} & c_{13}s_{12} & s_{13}e^{-i\delta} \\ -c_{23}s_{12} - s_{23}s_{13}c_{12}e^{i\delta} & c_{23}c_{12} - s_{23}s_{13}s_{12}e^{i\delta} & s_{23}c_{13} \\ s_{23}s_{12} - c_{23}s_{13}c_{12}e^{i\delta} & -s_{23}c_{12} - c_{23}s_{13}s_{12}e^{i\delta} & c_{23}c_{13} \end{pmatrix} \begin{pmatrix} e^{i\phi_1} & 0 & 0 \\ 0 & e^{i\phi_2} & 0 \\ 0 & 0 & 1 \end{pmatrix}, \quad (2.4)$$

with $c_{ij} \equiv \cos \theta_{ij}$ and $s_{ij} \equiv \sin \theta_{ij}$.

Given the uncertainty between the nature of neutrinos, whether they are Dirac particles, in which the particle and antiparticle are different objects ($\nu \neq \bar{\nu}$), or Majorana particles, where a particle is its own antiparticle ($\nu = \bar{\nu}$), the PMNS matrix is parameterized in two different ways.

If neutrinos are Dirac particles, the neutrino mixing matrix can be parameterized in terms of three Euler angles θ_{12} , θ_{13} , θ_{23} and a physical CP-violating phase, which refers to the violation of the combined conservation laws associated with charge conjugation and parity. However, if neutrinos are Majorana particles, there are two additional physical phases, ϕ_1 and ϕ_2 . [41]

Neutrino Oscillations in Vacuum

The mass eigenstates can be expressed as a linear combination of the flavour eigenstates,

$$|\nu_i\rangle = \sum_{\alpha=e,\mu,\tau} U_{\alpha i} |\nu_\alpha\rangle. \quad (2.5)$$

Since the mass eigenstates are eigenstates of the Hamiltonian that describes the propagation of neutrinos in vacuum, solving the Schrödinger equation, we can obtain the time evolution of a neutrino state as [43]:

$$|\nu_\alpha(t)\rangle = \sum_{i=1}^3 U_{\alpha i}^* e^{-iE_i t} |\nu_i\rangle = \sum_{\beta} \left(\sum_{i=1}^3 U_{\alpha i}^* e^{-iE_i t} U_{\beta i} \right) |\nu_\beta\rangle. \quad (2.6)$$

where $E_i = \sqrt{p^2 + m_i^2}$ is the energy of the i -th mass eigenstate ($\hbar = c = 1$).

The latter equation explicitly shows that as time passes there is a non-zero probability that the initial neutrino can oscillate and be detected in a flavour different from the initial. The probability of an initial flavour state α change into a flavour state β , is defined as the transition probability and can be expressed as [43]:

$$P_{\nu_\alpha \rightarrow \nu_\beta}(t) = |\langle \nu_\beta | \nu_\alpha(t) \rangle|^2 = \sum_{i,j} U_{\alpha i}^* U_{\beta i} U_{\alpha j} U_{\beta j}^* e^{-i(E_i - E_j)t}. \quad (2.7)$$

Since neutrinos are ultra-relativistic particles, the energy eigenvalues can be approximated as

$$E_i \approx \frac{m_i^2}{2E_\nu}, \quad (2.8)$$

with $E_\nu = |\vec{p}|^2$. Thus, the energy difference between the initial and final eigenvalues can be represented by

$$E_i - E_j = \frac{\Delta m_{ij}^2}{2E_\nu}, \quad (2.9)$$

where $\Delta m_{ij}^2 = m_i^2 - m_j^2$ is the mass splitting. Combining Equations 2.9 and 2.7 we can rewrite the transition probability as

$$P_{\nu_\alpha \rightarrow \nu_\beta}(t, E_\nu) = \sum_{i,j} U_{\alpha i}^* U_{\beta i} U_{\alpha j} U_{\beta j}^* e^{-i \left(\frac{\Delta m_{ij}^2}{2E_\nu} \right) t}. \quad (2.10)$$

In summary, neutrinos are created as pure flavour eigenstates which are specific combinations of the different mass eigenstates. However, as the state evolves over time the different mass eigenstates, which correspond to different mass values, propagate at different speeds resulting in an interference between flavour eigenstates.

The interference process, which exhibits an oscillatory behaviour, allows neutrinos to change from one flavour to another during their propagation. Thus, neutrino oscillations prove that neutrinos do have mass, because if the mass eigenstates had equal masses (all zero) they all propagated at the same speed and would not produce flavour oscillations. In fact, the only requirement is that the eigenstates have different masses, meaning that one of them may even be zero. Experiments observing neutrino oscillations are only sensitive to the mass squared differences, as shown in Equation 2.10, of three neutrino mass states, $\Delta m_{ij}^2 \equiv m_i^2 - m_j^2$, and not the absolute mass scale.

Experiments using solar neutrinos have measured the squared mass difference between m_2 and m_1 , the so called solar mass splitting: $\Delta m_{sol}^2 \simeq 7.42_{-0.20}^{+0.21} \times 10^{-5} \text{eV}^2$ [42]. While experiments using atmospheric neutrinos have measured the squared mass difference between m_3 and m_2 , the so called atmospheric mass splitting: $|\Delta m_{atm}^2| \simeq 2.517_{-0.028}^{+0.026} \times 10^{-3} \text{eV}^2 \gg \Delta m_{sol}^2$ [42].

In experiments studying neutrino oscillations, the absolute value of m_1 , m_2 and m_3 is not obtainable and it is also impossible to know whether or not m_2 is heavier than m_3 . The "neutrino mass hierarchy problem" comes from the uncertainty of which of the two masses, m_2 and m_3 , is bigger. Therefore, there are two possibilities: m_3 is larger than m_2 , which is called the normal hierarchy, or m_3 is lighter than m_2 , which is called inverted hierarchy. While we do not know at present whether ν_3 is heavier or lighter than ν_1 , we do know, from the solar neutrino experiments, that ν_2 is heavier than ν_1 since $\Delta m_{sol} \equiv \Delta m_{21}$ is greater than zero. Given that $\Delta m_{21}^2 \ll |\Delta m_{32}|^2$, the sign of Δm_{31}^2 and Δm_{32}^2 must be the same. Figure 2.3 summarizes the current knowledge on neutrino masses and mixings provided by neutrino oscillations experiments. It is illustrated Δm_{sol}^2 and Δm_{atm}^2 in both normal and inverted hierarchies.

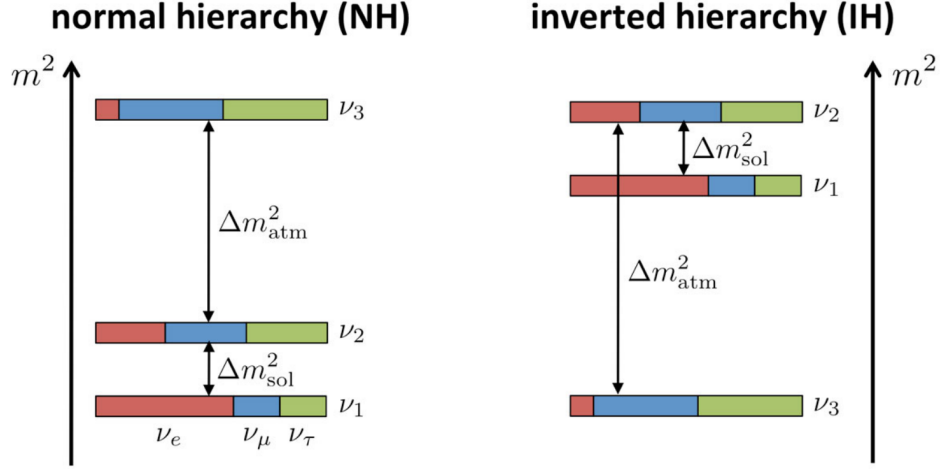


Figure 2.3: Two possible neutrino mass orderings. Left and right images show, respectively, the normal and inverted mass orderings and the neutrino masses increase from bottom to top. The electron, muon and tau flavour contents of each neutrino mass eigenstate are shown via the red, blue and green fractions, respectively. Figure from [44]

Our current knowledge of neutrino masses and mixings provided by neutrino oscillations data is summarized in Table 2.2.

2.3 Double Beta Decays

Double beta decay is a second-order process, extremely rare, in which a nucleus with charge Z and mass A decays into a nucleus with charge $(Z + 2)$ or $(Z - 2)$, depending on the decay mode as will be discussed later, and mass A .

This process occurs when the first-order beta decay is either energetically forbidden or suppressed by selection rules. In first order beta decay, there are three different modes of decay: beta minus decay, β^- , where a neutron changes into a proton while emitting an electron and an electron antineutrino,

$$n \rightarrow p + e^- + \bar{\nu}_e, \quad (2.11)$$

beta plus decay, β^+ , where a proton changes into a neutron, while emitting a positron and an electron neutrino,

Table 2.2: Neutrino mixing parameters according to the most recent oscillation analysis by González-García where $\Delta m_{3i}^2 \equiv \Delta m_{31}^2$ for the normal ordering and $\Delta m_{3i}^2 \equiv \Delta m_{32}^2$ for the inverted one. Table from [42].

Parameter	Normal ordering	Inverting ordering
	best fit $\pm 1\sigma$	best fit $\pm 1\sigma$
$\theta_{12}(\circ)$	$33.44^{+0.77}_{-0.74}$	$33.45^{+0.78}_{-0.75}$
$\theta_{23}(\circ)$	$49.2^{+0.9}_{-1.2}$	$49.3^{+0.9}_{-1.1}$
$\theta_{13}(\circ)$	$8.57^{+0.12}_{-0.12}$	$8.60^{+0.12}_{-0.12}$
$\delta_{CP}(\circ)$	197^{+27}_{-24}	282^{+26}_{-30}
$\Delta m_{21}^2 (10^{-5} \text{ eV}^2)$	$7.42^{+0.21}_{-0.20}$	$7.42^{+0.21}_{-0.20}$
$\Delta m_{3i}^2 (10^{-3} \text{ eV}^2)$	$+2.517^{+0.026}_{-0.028}$	$-2.498^{+0.028}_{-0.028}$

$$p \rightarrow n + e^+ + \nu_e, \quad (2.12)$$

and the final mode is electron capture, *EC*. An electron, frequently from the K shell, is absorbed into the nucleus, which changes a proton into a neutron emitting a neutrino. This leaves the atom in an excited state, and the process is accompanied by the emission of X-rays and/or Auger electrons:

$$p + e^- \rightarrow n + \nu_e. \quad (2.13)$$

These processes only occur if the mass of the parent nuclei is greater than that of the daughter nuclei, as illustrated in Figure 2.4.

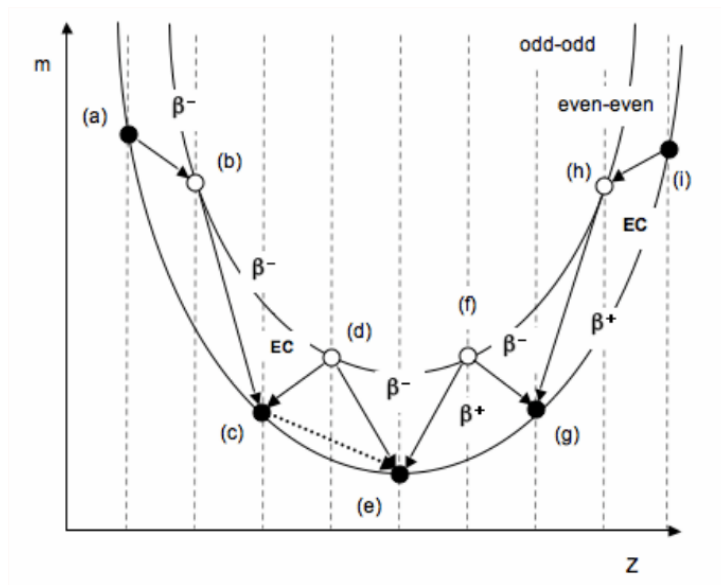


Figure 2.4: Representation of the semi-empirical mass formula, for isobaric nuclei, as a function of the proton number, Z , for odd-odd and even-even mass number, A . An odd-odd nucleus has an odd number of neutrons and an odd number of protons, while, an even-even nucleus has an even number of neutrons and an even number of protons. This double parabola shows energetically possible single and double beta decays. Double beta decay is possible between (c) and (e) and also between (g) and (e). (c) can not decay for example to (d) because the mass of (d) is greater than of the (c). (e) has the lowest mass so is stable. Figure from [45].

Figure 2.4 represents several possible decays for even-even and odd-odd nuclei with an even mass number, A . The isotopes from the left side decay via β^- decay while the ones from the right side decay either by β^+ decay or electron capture. Both of them decay towards the one stable isotope (e), at the bottom of the parabola, which has the lower mass.

The parabola of the odd-odd nuclei is shifted upwards due to the same nuclear pairing energy being added in both parabolas but with a positive sign in the even-even one and with a negative sign in the odd-odd. As can be seen in Figure 2.4, the parabola of the odd-odd isotopes is more unstable because the lower the binding energy, the more unstable the isotope will be.

Certain nuclei, from the even-even parabola, can decay into the second nearest neighbour via a double beta decay. For instance, in Figure 2.4, the isotope in the (c) position can not decay to (d) position since its mass is lower, but it can decay to (e) position via a double beta decay, since its mass is higher than that of the isotope

at (e) position. This double beta decay, $2\beta^-$, can occur when $M(Z,A) > M(Z+2,A)$ and the β^- decay is either highly suppressed or forbidden ($M(Z,A) < M(Z+1,A)$).

The $2\nu 2\beta^-$ and $0\nu 2\beta^-$ processes

Two neutrino double beta decay ($2\nu 2\beta^-$) is a second order weak process that conserves electric charge, total lepton number, and is an allowed process in the standard electroweak model. During this process, two neutrons simultaneously decay to two protons emitting two electrons and two electron antineutrinos, as shown in Figure 2.5,

$$(A, Z) \rightarrow (A, Z + 2) + 2e^- + 2\bar{\nu}_e. \quad (2.14)$$

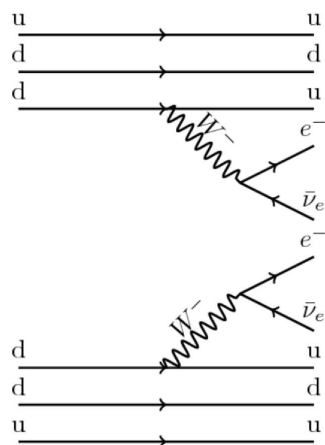


Figure 2.5: Feynman diagram for the $2\nu 2\beta^-$ decay process. Diagram created with [46].

Neutrinoless double beta decay ($0\nu 2\beta^-$) is a similar process, with two neutrons simultaneously decaying into two protons and two electrons, but no neutrino is in the final state, as seen in Figure 2.6. This process violates total lepton number conservation by two units, $\Delta L = 2$, and as such it is forbidden in the standard electroweak model. It has not yet been conclusively observed for any nuclei,

$$(A, Z) \rightarrow (A, Z + 2) + 2e^-. \quad (2.15)$$

The $0\nu 2\beta^-$ decay process is illustrated in Figure 2.6, showing that this process can only occur if $\nu_e \equiv \bar{\nu}_e$, *i.e.* if the neutrino is a Majorana particle. A virtual right-handed neutrino is emitted from one vertex and a virtual left-handed antineutrino

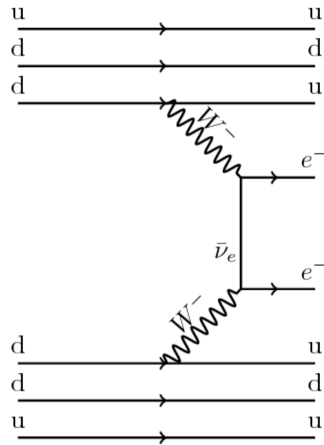


Figure 2.6: Feynman diagram for the $0\nu 2\beta^-$ decay process. Diagram created with [46].

is absorbed by the second vertex. Essentially, the virtual right-handed neutrino flips helicity to a virtual left-handed antineutrino. This helicity flip can only occur if the neutrino was massive. It would be impossible if the neutrino was massless as there would be no reference frame where the direction of momentum is reversed [47].

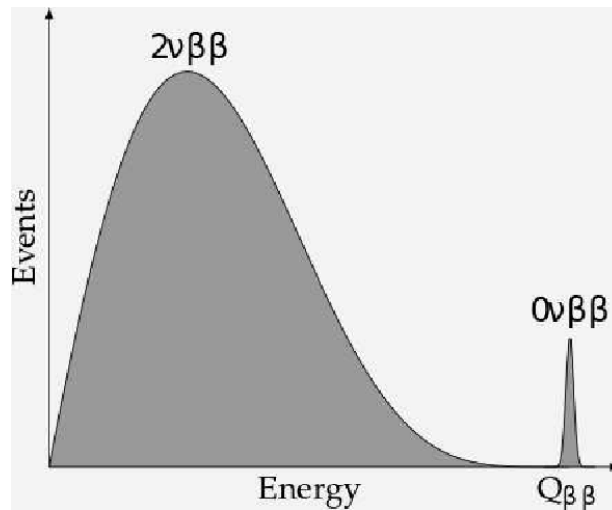


Figure 2.7: Electrons energy spectrum for the $2\nu 2\beta^-$ and $0\nu 2\beta^-$ decays, represented by the number of expected events as a function of the electrons energy. Figure from [48].

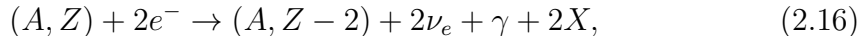
In the $2\nu 2\beta^-$ decay process, neutrinos will take away some of the kinetic energy of the electrons, which results in the electrons having a continuum energy spectrum from the start to the Q-value (see Figure 2.7). The end point of the spectrum, the

maximum possible total energy for the two electrons, is determined by the Q-value, *i.e.* the energy difference of the parent and the daughter nucleus of the decay.

By contrast, in the $0\nu 2\beta^-$ decay process, the emitted electrons must carry all the kinetic energy (the nucleus will also have some kinetic energy but negligible comparable to that of the electrons), and the two electron energy sum spectrum is a narrow line, at the endpoint $Q_{\beta\beta}$ -value of the decay process (see Figure 2.7). Nevertheless, the expected delta function will turn into a Gaussian distribution around the $Q_{\beta\beta}$ -value considering a realistic energy resolution of any detector.

The $2\nu 2EC$ and $0\nu 2EC$ processes

The double electron capture with emission of neutrinos ($2\nu 2EC$) is a SM allowed process in which two protons in the nucleus capture two orbital electrons, accompanied by the emission of two neutrinos. The final atom is left in an excited state, with two vacancies in the shells from which the electrons were captured. It then de-excites through the emission of gamma-rays, and the atomic vacancies are filled by outer electrons with emission of X-rays and/or Auger electrons. This process is represented by the Feynman diagram in Figure 2.8,



where γ represents the emitted gamma-rays and X the X-rays and Auger electrons.

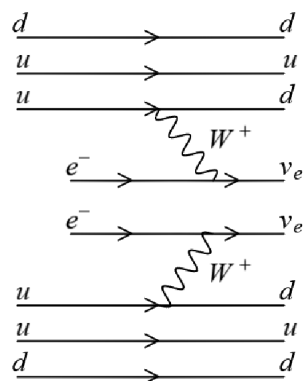


Figure 2.8: Feynman diagram for the $2\nu 2EC$ decay process. Diagram created with [46].

By reducing the atomic number by two, double electron capture transforms the nuclide into a different element. For a nuclide (A, Z) with number of nucleons A and atomic number Z , double electron capture is only possible if the mass of the daughter nucleus $(A, Z - 2)$ is lower than that of the parent (A, Z) .

The most common channel to investigate the nature of neutrinos is the $0\nu 2\beta^-$ decay, but $0\nu 2EC$ is an interesting alternative. The double electron capture can happen without emission of neutrinos, as shown in Figure 2.9, if a Majorana neutrino is exchanged the total lepton number conservation is violated by two units,

$$(A, Z) + 2e^- \rightarrow (A, Z - 2) + \gamma + 2X. \quad (2.17)$$

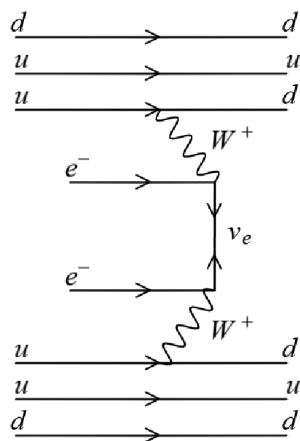


Figure 2.9: Feynman diagram for the $0\nu 2EC$ decay process. Diagram created with [46].

With no emitted particles to carry the energy of the decay, the neutrinoless double electron capture leaves the nucleus in an excited state and can lead either to a resonant decay [49] or a radiative process with or without a resonance condition [50, 51].

The resonant decay, $R0\nu 2EC$, occurs when there is a close degeneracy between the initial atomic state and the final excited state and it is depicted by [52, 53]

$$e^- + e^- + (A, Z) \rightarrow (A, Z - 2)^* \rightarrow (A, Z - 2) + \gamma + 2X, \quad (2.18)$$

where two orbital electrons are captured leaving the final nucleus in an excited state that decays through the emission of one or even several gamma-rays, γ , and the atomic vacancies would be filled by outer electrons with emission of X-rays and/or Auger electrons, X.

In this process, the energy of the excited state needs to fulfil two requirements: the resonance condition and also the energy conservation, so it needs to be approximately [53]

$$E_{exc} = Q - E_H - E_{H'}, \quad (2.19)$$

where E_H and $E_{H'}$ are the binding energies of the two captured electrons.

Therefore, the expected signal of this decay are several X-ray photons and/or Auger electrons, from the atomic shell de-excitation, in coincidence with one or more gamma-rays from the nucleus de-excitation [53]. An enormous difficulty has been to determine an accurate value of the difference between masses of the parent and daughter atoms, *i.e.* the Q-values [54]. The resonant decay, $R0\nu2EC$, motivated several experiments [55–59] since the resonance condition can enhance the decay rate by up to six orders of magnitude [49].

However, there is a particularly interesting case where the excess energy from the $0\nu2EC$ decay can be carried away by a photon, leading to a radiative process, which obeys or not to the resonance condition. Since, the angular momentum needs to be conserved, the captured electrons can not be both from the 1S orbital. Therefore, there are two possible transitions: the magnetic type, where the two electrons are captured from the 1S and 2S, and the electric type, in which the capture electrons are from the 1S and 2P [60]. The latter is the interesting one because the possible atomic resonance occurs when the photon energy equals to the energy of atomic 2P-1S transition.

The reason why $0\nu2\beta^-$ decay is preferred over $0\nu2EC$ is that the lifetime of the latter is generally expected to be several orders of magnitude larger than of the former. This is mainly true for the radiative process. However, a close degeneracy of the initial and final (excited) atomic states, characteristic of the resonant $0\nu2EC$, could enhance the rate of this decay by up to six orders of magnitude [49], making it competitive with $0\nu2\beta^-$.

The $2\nu\beta^+EC$ and $0\nu\beta^+EC$ processes

The electron capture with coincident positron emission occurs when a nucleus absorbs one orbital electron and simultaneously emits one positron and two neutrinos. Following the thermalization, the positron annihilates with an atomic electron which results in two back-to-back gamma-rays with 511 keV each one. Therefore, its experimental signature consists in a cascade of X-rays and/or Auger electrons, a beta-like spectrum from the positron and two back-to-back gamma-rays emitted after the annihilation of the positron with an electron. This decay, $2\nu\beta^+EC$, can be written as shown in Equation 2.20 and has the Feynman diagram illustrated in Figure 2.10a,

$$(A, Z) + e^- \rightarrow (A, Z - 2) + e^+ + 2\nu_e + X. \quad (2.20)$$

As we can see in Table 2.3, the half-life of the ^{124}Xe $2\nu\beta^+EC$ decay is expected to be $T_{1/2}^{2\nu\beta^+EC} = (1.7 \pm 0.6) \times 10^{23}$ yr. Due to its distinct experimental signature, it is expected to be detected in this generation of Dark Matter experiments, such as XENONnT and LZ, $\mathcal{O}(10 \text{ t})$.

In order to explore positron emission decays it is extremely important to have a detector with a remarkable position and energy resolution. Thus, the background can be highly suppressed using coincidence techniques depending on the expected signal. Moreover, with a high position resolution we can tag the gamma-rays emitted by positron-electron annihilation and reject the gamma-rays and beta decays backgrounds coming from natural radioactivity.

However, if the neutrino is a Majorana particle a neutrinoless electron capture with positron emission is possible and has the Feynman diagram illustrated in Figure 2.10b. Both the $2\nu\beta^+EC$ and $0\nu\beta^+EC$ processes can only happen for high Q-value decays, at least a Q-value higher than 1022 keV. While the energy spectrum for the positron in the $2\nu\beta^+EC$ decay would be a beta-like spectrum, the energy spectrum for the positron emitted in $0\nu\beta^+EC$ would be, roughly, a single peak,

$$(A, Z) + e^- \rightarrow (A, Z - 2) + e^+ + X. \quad (2.21)$$

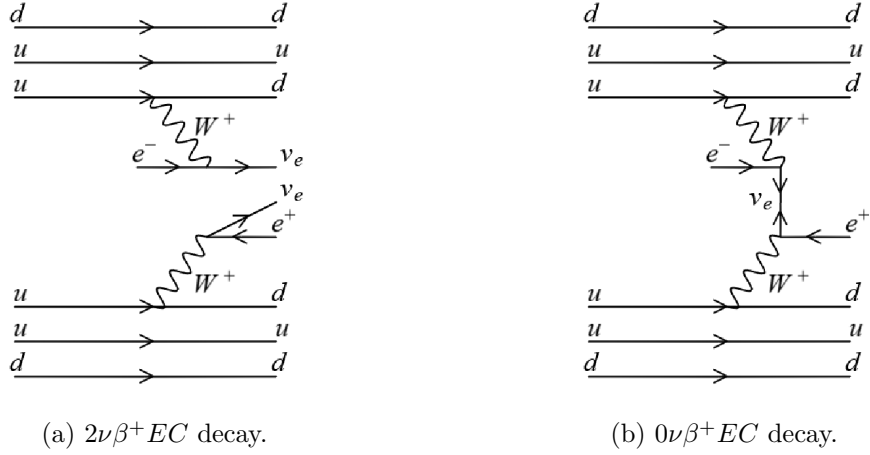


Figure 2.10: Feynman diagrams for the $2\nu\beta^+EC$ and $0\nu\beta^+EC$ decay processes. Diagrams created with [46].

The $2\nu2\beta^+$ and $0\nu2\beta^+$ processes

The double positron emission decay occurs when a pair of protons decay into a pair of neutrons producing a pair of positrons, accompanied by the emission of two neutrinos, as shown in Equation 2.22. The $2\nu2\beta^+$ can only occur for very high Q-values, for at least a Q-value of 2044 keV, which makes it much rarer. The expected half-life for the ^{124}Xe $2\nu2\beta^+$ decay is $T_{1/2}^{2\nu2\beta^+} = (2.2 \pm 0.7) \times 10^{28}$ years which, for this generation of Dark Matter detectors, is experimentally inaccessible. As in the $2\nu\beta^+EC$ decay, upon thermalization, the two positrons annihilate with two atomic electrons which results in two pairs of back-to-back gamma-rays with 511 keV each one,

$$(A, Z) \rightarrow (A, Z - 2) + 2e^+ + 2\nu_e. \quad (2.22)$$

Once again, if the neutrino is a Majorana particle the neutrinoless double positron emission decay is possible and the energy spectrum of the positrons for the two neutrino mode would be beta like instead of the neutrinoless mode that would be, approximately, a single peak. The neutrinoless double positron emission decay can be written as shown in Equation 2.23 and the Feynman diagram is illustrated in Figure 2.11b,

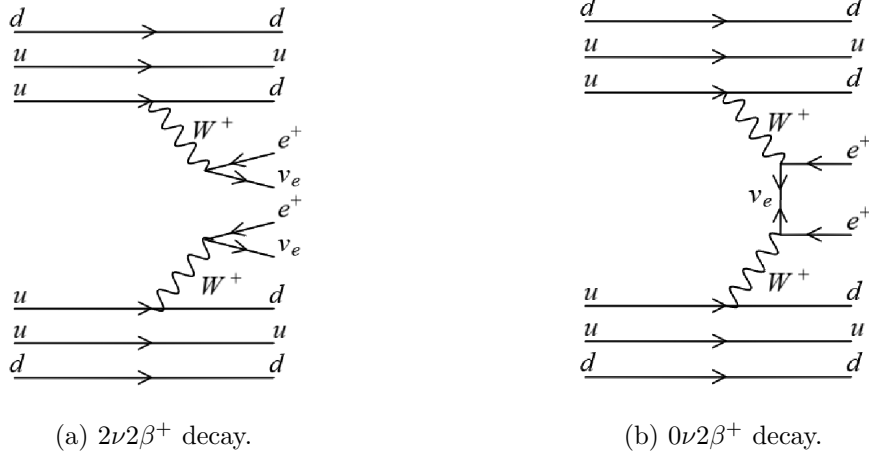


Figure 2.11: Feynman diagrams for the $2\nu 2\beta^+$ and $0\nu 2\beta^+$ decay processes. Diagrams created with [46].

$$(A, Z) \rightarrow (A, Z - 2) + 2e^+. \quad (2.23)$$

2.3.1 Half-life Calculations

Two Neutrino Decays

The half-life, $T_{1/2}^{2\nu}$, for the two-neutrino decay modes can be written in the form [61]

$$(T_{1/2}^{2\nu})^{-1} = G_{2\nu} |M_{2\nu}|^2, \quad (2.24)$$

where $G_{2\nu}$ is the phase space factor, which is defined as the number of states per unit of energy and per unit of volume and the $M_{2\nu}$ is the nuclear matrix element which gives the strength of the interaction between initial and final states. The phase space factor is different for each decay mode [62–64] but the nuclear matrix element for the $2\nu 2EC$ and the $2\nu\beta^+EC$ decays are very similar, while that of the $2\nu 2\beta^+$ decay [65, 66] is approximately half of the former. The predicted phase space factors, $G_{2\nu}$, for these three decays are summarized in Table 2.3. These relations can be expressed as [61]

$$M_{2\nu 2EC} = M_{2\nu\beta^+ EC} = 2 \times M_{2\nu 2\beta^+}. \quad (2.25)$$

Equation 2.25 can be useful to estimate $T_{1/2}^{2\nu\beta^+ EC}$ and $T_{1/2}^{2\nu 2\beta^+}$ as a function of $T_{1/2}^{2\nu 2EC}$, as shown in Equations 2.26 and 2.27, which is the only decay observed until now,

$$T_{1/2}^{2\nu\beta^+ EC} = \frac{G_{2\nu 2EC}}{G_{2\nu\beta^+ EC}} \times T_{1/2}^{2\nu 2EC}, \quad (2.26)$$

$$T_{1/2}^{2\nu 2\beta^+} = \frac{4 \times G_{2\nu 2EC}}{G_{2\nu 2\beta^+}} \times T_{1/2}^{2\nu 2EC}. \quad (2.27)$$

The predicted phase-space factor for the $2\nu EC\beta^+$ decay is approximately one order of magnitude lower than the one for $2\nu 2EC$ decay. Since, the half-life is inversely proportional to the phase-space factor, its half-life is expected to be one order of magnitude longer than the one for $2\nu 2EC$ decay and, thus, very likely to be detected in this generation of Dark Matter detectors. However, due to the smallness of the phase-space factor for the $2\nu 2\beta^+$ decay, its expected half-life is five orders of magnitude longer than the one for $2\nu 2EC$, making it unapproachable.

Table 2.3: The phase-space factors, the expected matrix elements (according to the assumptions presented in Equation 2.25) and the measured or predicted half-lives for the $2\nu 2EC$, $2\nu EC\beta^+$ and $2\nu 2\beta^+$ decay modes of ^{124}Xe . The half-lives were predicted based in the measured half-life of ^{124}Xe $2\nu 2EC$ decay, by XENON1T, and according to Equations 2.26 and 2.27. Each phase-space factor is presented in a range of values, since in [67] there is a collection of different values obtained with different methods for each one. The half-lives of the decay modes $2\nu EC\beta^+$ and $2\nu 2\beta^+$ were predicted using the central value of this range and for the uncertainty it was used half of this range. Table from [61].

Decay mode	$G_{2\nu}$ [yr^{-1}]	$M_{2\nu}$	Half-life [yr]	
			Measured	Predicted
$2\nu 2EC$	$(1.5-2.0) \cdot 10^{-20}$	$M_{2\nu 2EC}$	$(1.4 \pm 0.4) \cdot 10^{22}$	
$2\nu EC\beta^+$	$(1.2-1.7) \cdot 10^{-21}$	$M_{2\nu 2EC}$		$(1.7 \pm 0.6) \cdot 10^{23}$
$2\nu 2\beta^+$	$(4.3-4.9) \cdot 10^{-26}$	$\frac{1}{2} M_{2\nu 2EC}$		$(2.2 \pm 0.7) \cdot 10^{28}$

Neutrinoless Decays

In the case of the neutrinoless decay modes, the half-life can be factorized as [61]

$$(T_{1/2}^{0\nu})^{-1} = G_{0\nu} |M_{0\nu}|^2 |f(m_i, U_{ei})|^2. \quad (2.28)$$

Once again, $G_{0\nu}$ is a phase space factor, $M_{0\nu}$ is the nuclear matrix element (both are different from the two neutrino mode) and $f(m_i, U_{ei})$ is an additional factor that contains physics beyond the SM. If the decay proceeds via light neutrino exchange, we have [61]

$$f(m_i, U_{ei}) = \frac{\langle m_\nu \rangle}{m_e} = \frac{\sum_{k=light} (U_{ek}^2 m_k)}{m_e}, \quad (2.29)$$

where $\langle m_\nu \rangle$, the effective Majorana neutrino mass, is a linear combination of the neutrino masses, m_i , and elements of the PMNS matrix U_{ei} of neutrino species [54].

However, for example, for the $0\nu 2EC$ resonance case, assuming the captured electrons are both from the K-shell (Equation 2.30), an additional factor is needed, R .

$$(A, Z) + 2e^- \rightarrow (A, Z - 2)^* \rightarrow (A, Z - 2) + \gamma + 2X_{KK}. \quad (2.30)$$

This R factor is defined by the mismatch between the available energy and the energy of the daughter nucleus in the excited state [68], $\Delta = |Q - E_{KK} - E_{exc}|$,

$$R = \frac{m_e c^2 \Gamma}{\Delta^2 + \Gamma^2/4}. \quad (2.31)$$

where $\Gamma = \Gamma_{e_{K1}} + \Gamma_{e_{K2}}$ is the two-hole width [68] and, in this case, is determined by the dipole emission rate leading to the de-excitation of the electrons shell [69]. The resonance decay must occur through the tail of the width of the atomic initial state [68], as shown in Figure 2.12.

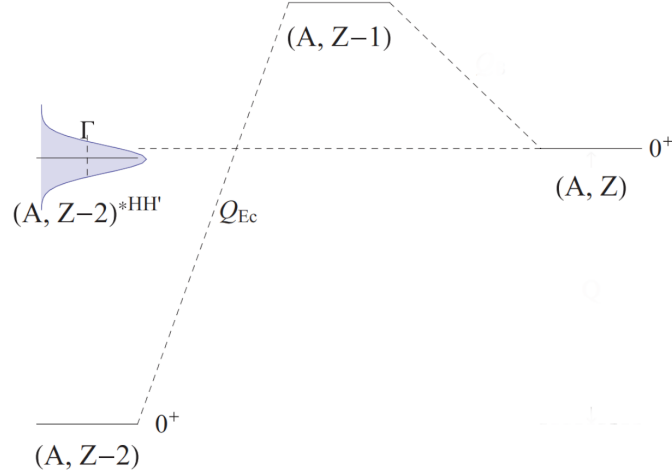


Figure 2.12: Schematic representation of a general $0\nu 2EC$ decay. Figure from [68].

For the electronic transitions between the innermost shells and very large Z , the Auger effect is less likely than the emission of X-rays [70]. Therefore, in the case of electron vacancies in ^{124}Xe we expect X-ray dipole emissions to be dominant.

For a K vacancy, the dipole transition $2p \rightarrow 1s$ has a probability of $\Gamma = 4 \times 10^{-7} Z^4$ eV [69]. Thus, for a K vacancy in ^{124}Xe the probability is $\Gamma \approx 3.4$ eV and for a double K vacancy is $\Gamma \approx 6.8$ eV.

The half-life for the $R0\nu 2EC$ decay can be written as

$$(T_{1/2}^{R0\nu 2EC})^{-1} = G_{0\nu} |M_{0\nu}|^2 |f(m_i, U_{ei})|^2 \frac{m_e c^2 \Gamma}{\Delta^2 + \Gamma^2/4}. \quad (2.32)$$

Since the half-life for $R0\nu 2EC$ decay is inversely proportional to the R factor (Equation 2.32), the higher the R factor is the more likely it is to see the decay. The maximum value of R is reached for a $\Delta = 0$ (Equation 2.31), and it rapidly decreases with the increasing of Δ so it needs to be as small as possible.

Chapter 3

The LUX-ZEPLIN Experiment

The LZ experiment is a next generation dark matter direct detection experiment based on xenon TPC technology, which provides a complete 3D picture of the deposited energy by interactions with the gas and liquid xenon volume. It is a second generation detector (G2), in the hunt for dark matter in the form of cosmic Weakly Interacting Massive Particles (WIMPs). It emerged from the combination of LUX (Large Underground Xenon) [71] and ZEPLIN (ZonEd Proportional scintillation in LIquid Noble gases) [72] experiments.

It is installed in the Davis cavern of the SURF, in the old Homestake gold mine, at a depth of 4850 feet (1478 m), as shown in Figure 3.1, in Lead, South Dakota, USA. This is the same laboratory where the famous solar neutrino experiment of Raymond Davis ran in the late 1960s [73], which provided one of the first pieces of evidence for the neutrino flavour oscillation and later made him receive the 2002 Nobel Prize [74].

The detector design and experimental strategy of LZ derive strongly from the LUX experiment, which was a very similar experiment, also searching for WIMPs, but the amount of xenon used was much smaller, only about 370 kg. The LUX experiment also ran in the same laboratory as LZ, between 2013 and 2016 [75], and in neither of its two runs, the first one during 95 live-days and the last one during 332 live-days, did it find more events than the expected from the backgrounds. Hence, no evidence of WIMPs interactions with the liquid xenon target was observed.

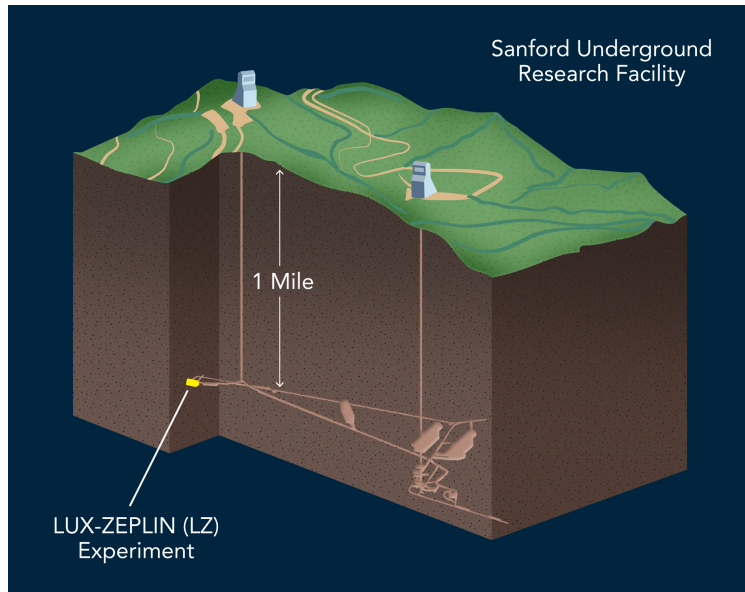


Figure 3.1: Location of the LZ experiment at the SURF in South Dakota. Figure from [76].

3.1 The LZ Detector

A three-dimensional model of the LZ detector is shown in Figure 3.2. The LZ detector consists in a TPC filled with 7 tonnes of liquid xenon surrounded by a xenon layer (skin). All of the liquid xenon is surrounded by an outer detector of gadolinium loaded liquid scintillator and a layer of ultra-pure water. The main systems of the detector are the described in the following subsections.

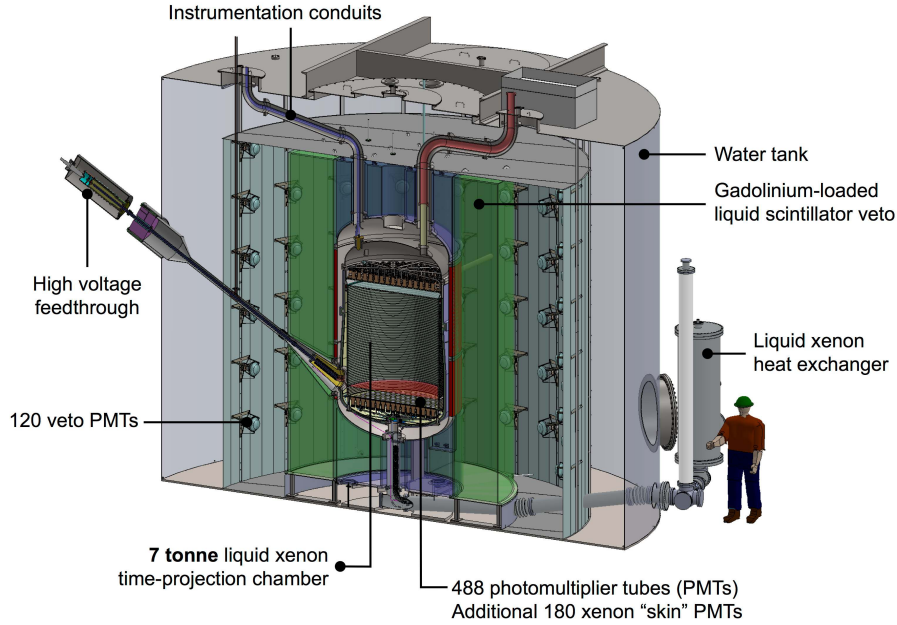


Figure 3.2: Schematic representation of the LZ detector. Figure from [77].

3.1.1 The Xenon Skin and Dual-Phase TPC

As in the LUX experiment, the TPC is surrounded by highly reflective polytetrafluoroethylene (PTFE) panels, with a reflectance of $R=(96.5 \pm 1.5)\%$ [78] at the scintillation wavelength of liquid xenon ($\lambda=178$ nm), aiming to maximize light collection.

All the signals produced within the active region of the TPC are detected by 494 Hamamatsu (R11410-22 with 3"-diameter) PMTs which are assembled in two arrays viewing the liquid xenon from above and below, with 253 and 241 PMTs, respectively [78].

In order to maintain the TPC thermally isolated it is placed inside a double walled titanium cryostat [79]. The cryostat is a vessel designed to contain 10 tonnes of liquid xenon, at 175.8 K (-97.4 °C), and it is divided into two main parts: the inner cryostat and the outer cryostat, between which a vacuum is maintained so as to achieve thermal insulation.

Between the PTFE reflectors and the cryostat an additional volume of xenon

with approximately 2 tonnes, referred to as the xenon skin, is used to shield the TPC and veto background. In order to view the scintillation light emitted in the side xenon skin, it was instrumented a ring of 93 smaller PMTs (R8520 with 1"-square) and to view the bottom of the detector another set of 38 PMTs (R8778 with 2"-diameter) that were recycled from LUX.

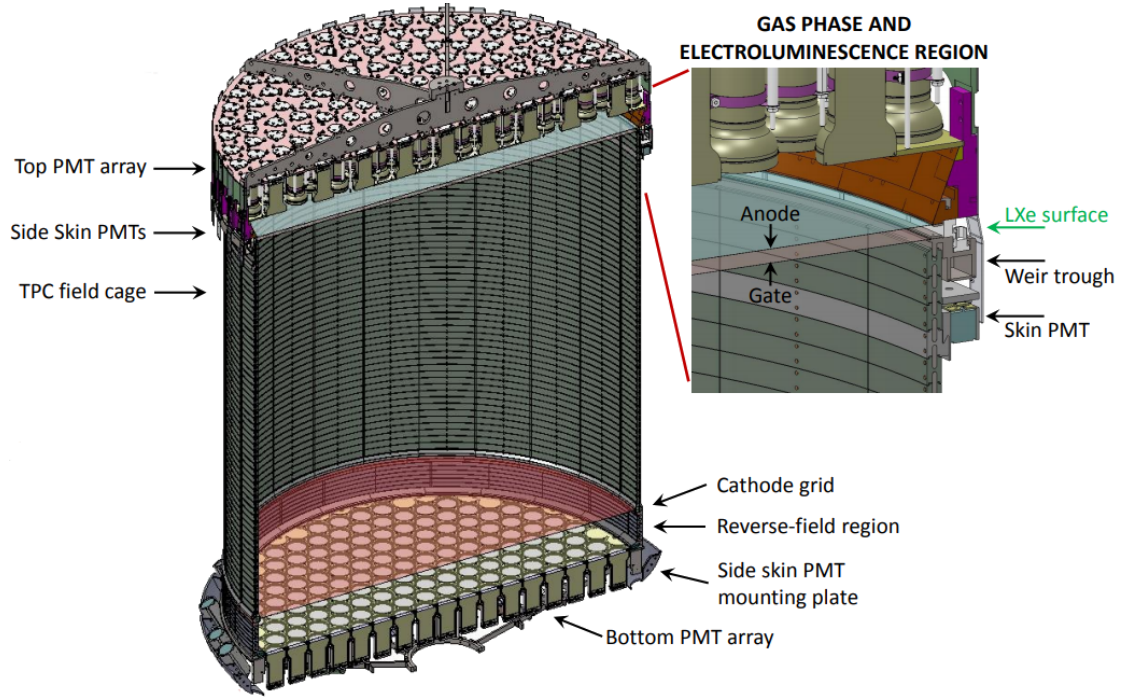


Figure 3.3: Section view of the TPC of LZ, with the liquid-gas interface region shown with more detail. Figure from [78].

In the active region of the TPC, the most important region of the detector, between the cathode and the gate grids an electric field (see Figure 3.3) with a design strength of 310 V/cm [78] is created so that the ionization electrons produced by interactions with the liquid xenon drift upwards. In order to ensure a uniform drift field several field shaping rings, spaced by 2 cm and connected via a resistor chain, were mounted inside the PTFE walls [78].

Then, in the region above the gate grid and below the anode a stronger field extracts these electrons into the gas phase, and accelerates them to create a proportional scintillation signal. The extraction field has a strength of 10200 V/cm [78] in the xenon gas and roughly half of this value in the liquid xenon due

to the relative permittivity of the liquid phase being $\epsilon_r = 1.96$ [78].

Furthermore, in order to protect the bottom PMTs from the high cathode voltage another field, with a design strength of 2900 V/cm [78], is created in a small region, the reverse field region (RFR), below the cathode and above the bottom PMT array. Thus, the electric field is parted in three regions: the RFR region, the drift region and the electroluminescence region, see Figure 3.4.

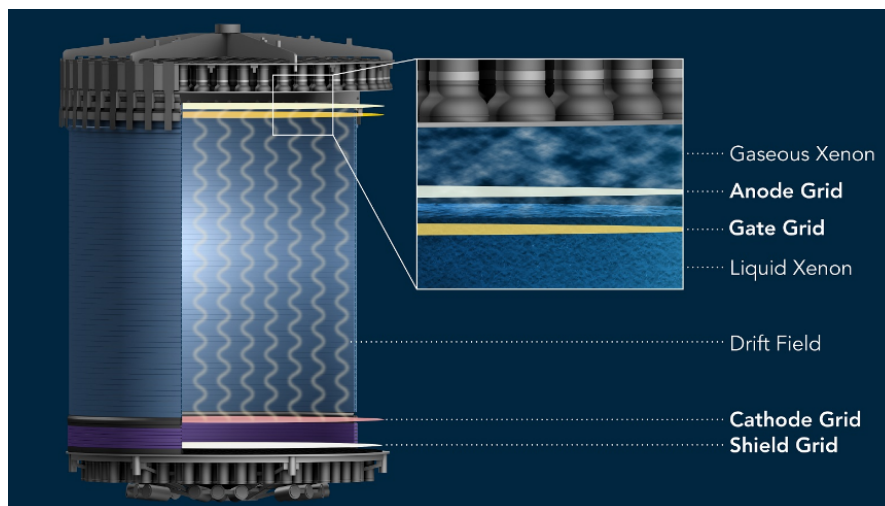


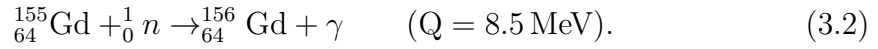
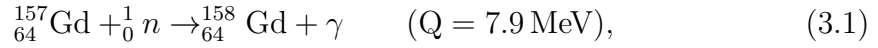
Figure 3.4: Schematic illustration of the four high-voltage grids inside the TPC. The drift field, which pushes the ionized electrons to the top of the tank, is created by the cathode and gate grid. There, the electrons are extracted through a field created by the anode and gate grids. At the bottom of the tank, the shield grid protects the bottom PMT array from the high electric fields above. Figure from [80].

Starting from the top to the bottom: The gaseous xenon is located from the upper PMTs up to the liquid xenon surface, which is located between the anode and gate grids; The anode, which is placed 8 mm below the upper PMTs, and the gate grids are 13 mm apart. The extraction field is created between the anode and the gate grids; the liquid xenon present in the drift field region is placed between the gate and cathode grids which are 1.456 m apart; the reverse field region, which is placed between the cathode and bottom shield grid, has a height of 0.1375 m; the distance between the latter and the bottom PMTs is about 2 cm.

3.1.2 The Outer Detector

The cryostat vessel is surrounded by the OD, a set of acrylic vessels which provide a near 4π coverage of LZ. They contain 17.3 tonnes of gadolinium loaded linear alkylbenzene (LAB) which is a liquid scintillator with good optical transparency, high light yields and low contamination with radioactive impurities [81, 82].

Gadolinium is one of the elements with highest cross section to capture thermal neutrons and the main contribution comes from ^{155}Gd and ^{157}Gd isotopes, which have an estimated cross section of 62.2(2.2) kb and 239.8(8.4) kb [83], respectively. Consequently, the LAB is loaded with gadolinium at 0.1% by mass in order to increase the probability of neutron capture and thus identify events in which neutrons may have interacted in the TPC. Gadolinium can capture a neutron mainly through these next processes [84]:



The cascade of high energy gamma-rays makes these captures easy to detect by the OD, skin or the TPC itself.

The entire LZ assembly is placed inside a water tank aiming to shield it from external gamma-rays and thermalize fast neutrons from the rock. A set of 120 PMTs (R5912 with 8"-diameter) were mounted on the water tank, arranged in a cylindrical array of 20 ladders equally spaced, aiming to view the scintillation light produced inside the acrylic vessels.

The OD and the skin provide an extremely efficient veto system, rejecting most of the background events that could be mistaken with the signal of the decay we are looking for.

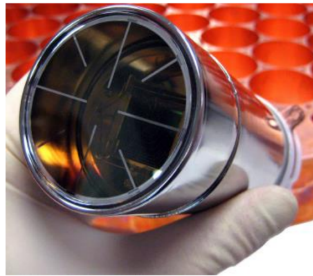
Figure 3.5 shows the four types of PMTs that were designed in order to make the recorded data as accurate as possible. Therefore, some requirements need to be fulfilled such as a good spectral response for the xenon scintillation light, good



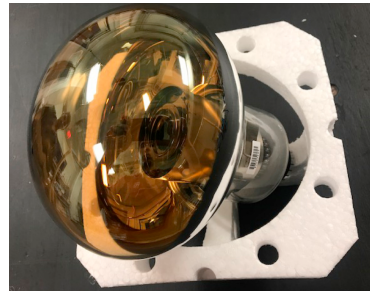
(a) R11410-22 PMT.



(b) R8520 PMT.



(c) R8778 PMT.



(d) R5912 PMT.

Figure 3.5: The four types of PMTs employed in the LZ experiment. The R11410-22 PMTs were assembled to view the scintillation light produced in the active region of the TPC, the R8520 and R8778 PMTs in the xenon skin and the R5912 PMTs in the water tank to view the OD scintillation light. Figures from [78, 80].

single-photoelectron (phe) definition, low dark noise, ultra-low levels of radioactivity and the ability to operate at extremely low temperatures.

3.2 Particle Detection in liquid xenon

The process of energy deposition in liquid xenon is shown in Figure 3.6. After an interaction with a xenon atom, the energy deposit from the interaction is split along three different paths: excitation, heat and ionization [85]. The ionization branch yields electrons, which can either be drifted away via an applied electric field or recombine with ionized xenon atoms resulting in a return to the excitation branch. The excited xenon atoms decay via the formation of an excited xenon dimer, Xe_2^* , which emits a VUV photon (175 nm [86]) as it decays back to the ground state xenon atoms [87]. The energy lost in the form of heat do not produce any visible signal in the chamber, and thus is undetectable. So, the total number

of VUV photons, N_{ph} , is [88]:

$$N_{ph} = a \cdot N_{ex} + b \cdot r \cdot N_i, \quad (3.3)$$

where N_{ph} is the number of produced scintillation photons, N_{ex} is the number of produced excited xenon atoms not produced by recombination, N_i is the number of ions produced, r is the recombination fraction (the fraction of ions that recombine) and a and b represent the efficiencies for direct excited xenon atoms and recombined ions to produce scintillation photons with the expectation that $a \approx b \approx 1$ [88]. So, if an electric field is applied, the electrons that do not recombine can be extracted from the event site, with the amount of extracted charge being:

$$N_q = (1 - r)N_i. \quad (3.4)$$

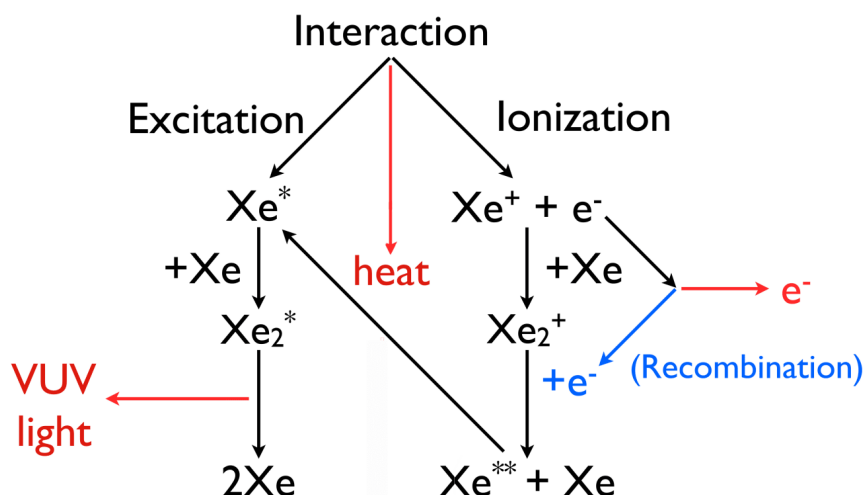


Figure 3.6: Basic schematic representation of the processes following an interaction in xenon, leading to the production of scintillation light and ionization electrons.

After a particle interaction with a xenon atom, in the liquid xenon, a prompt scintillation signal, called S1, is created. Simultaneously, electrons may be liberated due to ionization processes. Some of these electrons may recombine with the xenon ions which results in fewer free electrons but more scintillation light. Therefore, prompt scintillation signal (S1) is the result of both excitation and recombination of initial electrons and xenon ions.

The electrons that do not recombine drift towards the top of the detector

through the electric field created by the voltage difference between the cathode and the gate grids. There they are extracted by the high electric field produced by the voltage difference between the gate and anode grids into the gas region, at the top of the chamber. Once extracted, these electrons accelerate vertically in the gas and produce secondary scintillation (electroluminescence), which is proportional to the electric field strength, the number of extracted electrons, the pressure of the gaseous xenon and its gap size, see Figure 3.7. Thus, the secondary scintillation signal (S2) is the result of the electroluminescence in the gas phase caused by the ionization produced by the electrons which did not recombine in the liquid xenon.

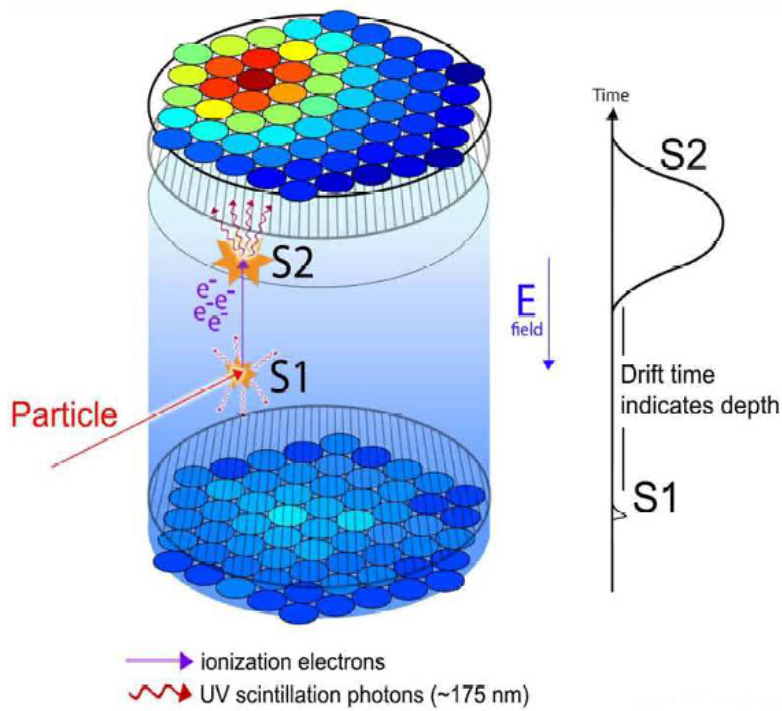


Figure 3.7: Representation of an interaction in the liquid xenon inside a dual-phase xenon TPC. Figure from [77].

In LZ, the 241 PMTs in the bottom array are arranged in a close-packed hexagonal pattern to maximize the light collection efficiency for S1, while the 253 top PMTs are arranged in a hybrid pattern that transitions from hexagonal near the center to nearly circular at the perimeter, thereby optimizing the (x, y) position reconstruction using the S2 signal for interactions near the TPC walls [78].

The relative intensity of S2 light in each PMT of the top array is used to

reconstruct the event position in the horizontal (x, y) plane and the time difference between the S1 and S2 pulses is proportional to the free electron drift distance and it is used to determine the depth (z) of the interaction. Furthermore, it is possible to infer the nature of the interaction from the ratio of the delayed and prompt signals, $S2/S1$.

Interactions in the liquid xenon can be divided into two categories: electron recoils (ERs), in which the interaction is with an electron of a xenon atom or when an electron from a beta decay deposits energy into the liquid xenon, and nuclear recoils (NRs), in which the interaction is with the entire nucleus, causing it to recoil in the medium. The latter can be caused by neutrons and is the expected interaction by dark matter WIMP particles, while the former is caused by electromagnetic interactions from gamma-rays, X-rays and beta particles.

Another difference between ERs and NRs, and the main way to discriminate one from the other, is how much energy is lost in the xenon per unit length, dE/dx , *i.e.* the stopping power. For ERs and NRs of the same energy the ER recoil goes further than the NR. Consequently, in an NR event the local charge density is higher providing a higher recombination, which results in the reduction of S2/S1 ratio. As seen in Figure 3.8 the ERs, represented by blue lines, have a higher mean S2/S1 ratio than the NRs, represented by red lines.

In the case of ERs, the energy is distributed in the ionization and scintillation channels preferentially, and only a very small amount of energy is lost to the heat, while in the case of NRs much more energy is lost to the heat channel, and thus it is undetected. Figure 3.8 illustrates this effect: the top plot shows the behaviour of an ER population in the S2/S1 discrimination variable, which is consistently higher than the corresponding NR population shown in the bottom plot. This type of detector can achieve a $> 99.5\%$ ER/NR discrimination for a 50% NR acceptance, event at modest drift fields.

In the case of ERs, it is useful to define a new parameter in Equation 3.3 which is the energy calibration factor, W_{ph} , in an event with full recombination ($N_q = 0$, $r = 1$).

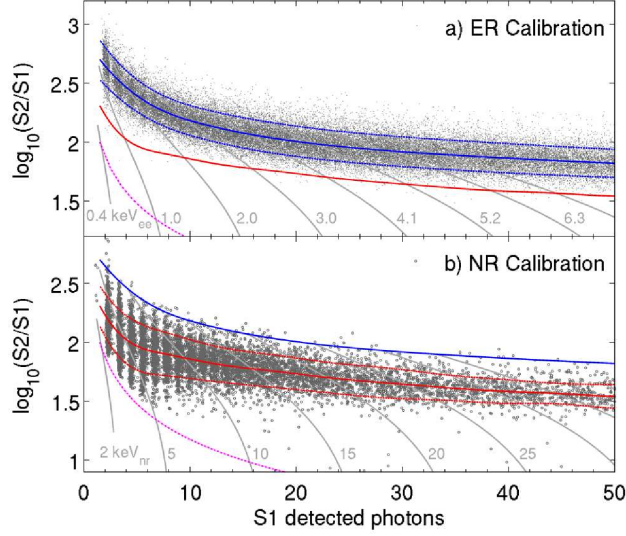


Figure 3.8: Graphical representation of $\log_{10}(S2/S1)$ as a function of S1 photons detected for calibrations of the LUX detector response in the fiducial volume. The upper graphic, a), shows the ER calibration using tritium, and the bottom one, b), the NR calibration using mono-energetic neutrons from the D-D generator. The solid blue and red lines represent the ER and NR band means, respectively. The dashed blue and red lines represent the $\pm 1.28 \sigma$ contours for the ER and NR bands, respectively. The dot-dashed magenta line represents the S2 threshold in analysis. The gray lines are the contours of constant energy deposition for an ER, in units of kilo electron-volts electron-equivalent (keV_{ee}), or an NR, in units of kilo electron-volts nuclear-equivalent (keV_{nr}). See [89] for more details.

$$\frac{E}{W_{ph}} = a \cdot N_{ex} + b \cdot N_i, \quad (3.5)$$

where E is the deposited energy and the other variables have already been defined previously.

Redefining the parameters $W = W_{ph} \cdot b$, $n_e = N_q$ and $n_\gamma = \frac{N_{ph}}{b}$ we come to three new Equations:

$$E = (n_e + n_\gamma) \cdot W, \quad (3.6)$$

$$n_e = (1 - r) \cdot N_i, \quad (3.7)$$

$$n_\gamma = \left(\frac{a \cdot N_{ex}}{b \cdot N_i} + r \right) \cdot N_i, \quad (3.8)$$

where W is the average energy to produce a quanta (either a photon or an electron), n_e is the number of drifted electrons and n_γ is the number of emitted primary scintillation photons.

As shown in Equation 3.6, the energy is insensitive to the number of electrons that undergo recombination and is only dependent on the sum of the quanta in the two channels.

While for the ERs, most of the energy is lost through ionization and some also to scintillation, for NRs, a significant fraction of energy is lost through heat. This relative loss of energy, as compared to an ER of equivalent initial energy, is parameterized through the Lindhard factor, \mathcal{L} [90]. The Lindhard factor estimates the amount of energy from an NR available to produce ionization and excitation in xenon and can be defined by [91]:

$$\mathcal{L} = \frac{kg(\epsilon)}{1 + kg(\epsilon)}, \quad (3.9)$$

following [91], with

$$k = 0.133 \cdot Z^{2/3} \cdot A^{1/2}, \quad (3.10)$$

$$g(\epsilon) = 3\epsilon^{0.15} + 0.7\epsilon^{0.6} + \epsilon \quad \text{and}, \quad (3.11)$$

$$\epsilon = 11.5E_{nr} \cdot Z^{-7/3}, \quad (3.12)$$

where Z is the atomic number ($Z = 54$ in the case of xenon), A is the atomic mass ($A = 131.293(6)$ u [92]) and E_{nr} is the energy of the NR. Due to this loss of energy into heat, relatively to ERs, Equation 3.6 for NRs is redefined as:

$$E_{nr} = \mathcal{L}^{-1} \cdot (n_e + n_\gamma) \cdot W. \quad (3.13)$$

where the Lindhard factor is expected to be $\mathcal{L} \approx 1/5$ [77].

Energy Reconstruction Calibration

In order to determine the deposited energy, as can be seen in Equations 3.6 and 3.13 for electron and nuclear recoils, respectively, it is essential to analyze how to reconstruct the number of extracted electrons, n_e , and the number of scintillation photons emitted, n_γ , from the raw data.

Thus, we can correlate the number of scintillation photons detected, the S1 signal, with the number of emitted photons, n_γ , through the g_1 factor, which represents the detection probability of an emitted scintillation photon. The number of detected electrons, the S2 signal, is related with the number of drifted electrons, n_e , by the g_2 factor, which represents the number of detected photons for each electron extracted to the gas multiplied by the probability that an electron reaching the surface is extracted to the gas. Consequently, the S1 and S2 signals can be translated into

$$S1 = g_1 \cdot n_\gamma, \quad (3.14)$$

$$S2 = g_2 \cdot n_e, \quad (3.15)$$

It is worth mentioning that both S1 and S2 signals need to be corrected due to the variation of light collection with position and the effect of finite electron lifetime, which is the mean time/distance an electron survives in the liquid xenon before being attached to an impurity. The corrected S1 and S2 signals are denoted by S1c and S2c, respectively.

Combining Equations 3.14 and 3.15 with Equation 3.6 we rewrite the combined energy equation for ERs as,

$$E = \left(\frac{S1}{g_1} + \frac{S2}{g_2} \right) \cdot W, \quad (3.16)$$

and for NRs as,

$$E = \frac{1}{\mathcal{L}(E)} \left(\frac{S1}{g_1} + \frac{S2}{g_2} \right) \cdot W. \quad (3.17)$$

The Lindhard factor, \mathcal{L} , and W are intrinsic properties of xenon while the factors g_1 and g_2 must be determined from calibration data because both depend on each

detector and g_2 additionally depends on the intensity of the extraction field since it affects the quantity of electrons that are extracted from the liquid to gaseous xenon.

To calibrate the detector response to the interactions, LZ will use a set of sources that produce both ERs and NRs in the TPC, skin and OD. These calibration sources can be internal or external. The internal sources are dissolved in the liquid xenon while the external ones are encapsulated and placed near the detector via one of three source tubes or even through beam sources that fire energetic particles from outside the detector.

It is extremely important to calibrate the detector response in order to achieve the most accurate results possible. Hence, these calibrations are very useful to correct the S1 and S2 signals, measure the number of detected photons and emitted electrons as a function of the deposited energy, calculate the g_1 and g_2 factors, estimate the Lindhard factor and also to obtain the energy resolution. Table 3.1 (ref.[82, 93]) presents the list of sources that will be used to calibrate the response of LZ to ERs (the first seven) and NRs (the last three).

Table 3.1: LZ Calibration sources, their deployment mode, interaction type and energy lines (or range).

Source	Deployment	Type	Source Energy (keV)
CH ₃ T	Internal	β	[0,18.6]
^{131m} Xe	Internal	γ	163.93
^{83m} Kr	Internal	IC and Auger electrons	32.1/9.4
²²⁰ Rn	Internal	α	6404.67
²² Na	External	β^+/γ	511/1275
⁵⁷ Co	External	γ	122
²²⁸ Th	External	γ	2615
AmLi	External	Neutron (α, n)	[0,1500]
⁸⁸ YBe	External	Neutron (γ, n)	153
D-D	Beam	Neutron	2450

One of the sources used to study the ER response of the detector is the beta emitter tritium (³H), in the form of tritiated methane (CH₃T), which has a 12.3 years half-life and spans an energy range from 0 keV to the 18.6 keV endpoint [94]. It will

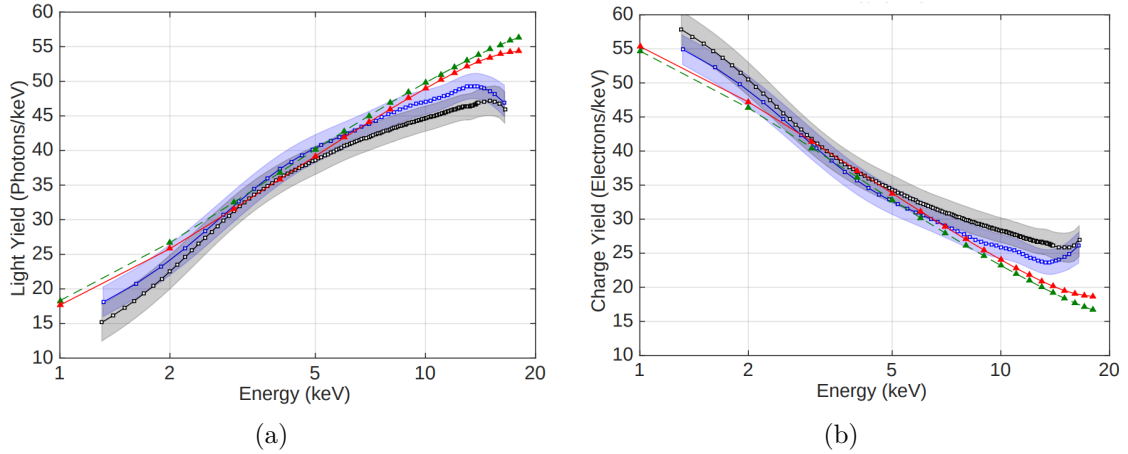


Figure 3.9: Graphical representation of the light yield (a) and charge yield (b) of the CH_3T events in LUX for two field strengths: 105 V/cm and 180 V/cm which are represented by the blue and black squares, respectively. The blue and grey bands indicate the 1σ systematic uncertainties on the data, while the statistical uncertainties are negligible in comparison. NEST is a package which provides a model for the scintillation light and ionization charge yields as a function of electric field and energy or stopping power [96]. The NEST predictions for the 105 V/cm and 180 V/cm are shown the green dashed and solid red lines. Figure from [95].

be dissolved in the liquid xenon and will be particularly useful to calibrate the low energy ER band thanks to its low energy endpoint [95]. Due to its long half-life it is extremely important to completely extract all the CH_3T from the liquid xenon. Thus the decision to use CH_3T instead of pure ^3H , because the getters in the purification system are extremely effective at absorbing methane, and because the methane has a low absorptivity into PTFE detector components relative to ^3H [95].

As shown in Figure 3.9, the light yield increases very quickly between 1 keV and 6 keV, while the charge yield has the inverse behaviour, as was expected since their sum is a constant. The complementary behaviour between the light and charge yields comes from the recombination process, in which an electron is captured by Xe^+ ions, creating Xe^* excitations, and eventually photons. Therefore, the greater the light yield is, the lower the charge yield will be, and so conversely. As can also be seen in Figure 3.9, a higher field leads to a lower light yield and a larger charge yield as expected, since it suppresses the recombination.

3.3 Monte Carlo Simulations of the LZ Detector

For any large scale physics experiment, it is paramount to have a reliable and robust simulation framework. Monte Carlo simulations are a fundamental tool for the analysis and prediction of the expected backgrounds depending not only on the external environment, but also on the components of the detector itself.

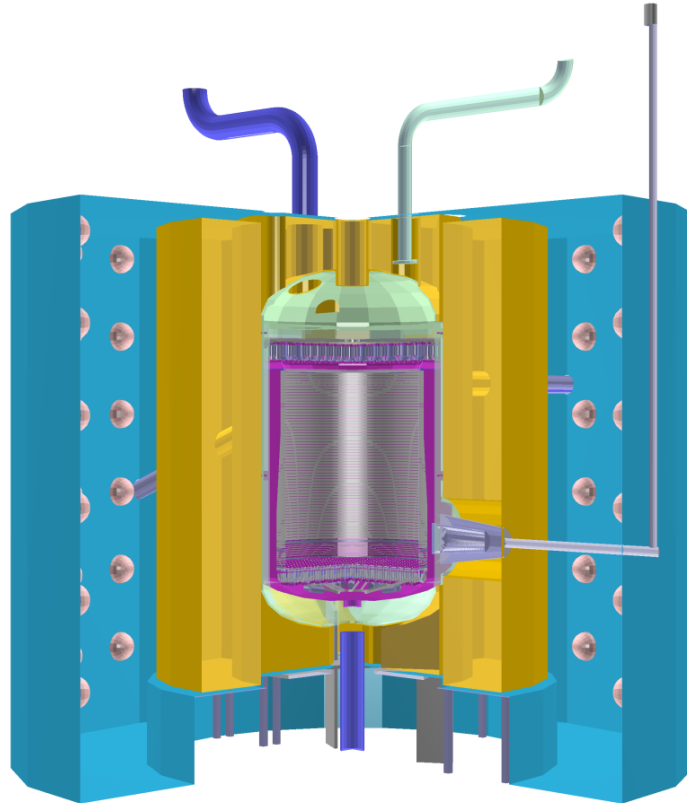


Figure 3.10: Representation of the LZ detector in BACCARAT. The water tank, instrumented with the PMTs, is shown in blue. On the inside of the water tank, the gadolinium loaded organic liquid scintillator OD is shown in yellow, the cryostat in light green and the innermost part, the TPC, is shown in magenta. Figure from [93].

LZ uses the simulation package BACCARAT (Basically A Component-Centric Analog Response to Anything) which evolved from LUXSim [97], a previous simulation package conceived for the LUX experiment.

BACCARAT is built on the GEANT4 toolkit which models the interactions of particles with matter. GEANT4 is used in several domains like medical imaging

and treatment, high energy physics experiments and the assessment of radiation effects on satellites [98].

It provides a set of functionalities including tracking, geometry and physics models. The physics models are able to describe electromagnetic and hadronic interactions, and also include decay and optical processes. GEANT4 also enables the users to create and implement their own personalized configuration of physics models according to their requirements.

Therefore, in BACCARAT, it is necessary to define the detector geometry, the materials used in each component alongside with its radioactive contamination, and the physics models that describe the physics within the detector. Figure 3.10 illustrates the geometry of the LZ experiment used in GEANT4 [93].

Once the information regarding the interactions with and within the detector is simulated it can be processed by two distinct chains, see Figure 3.13 [93]. In the first one, the values of energy depositions, obtained with GEANT4, are parameterized into primary scintillation photons and ionization electrons, originating S1 and S2 values respectively, through the NEST (Noble Element Scintillation Technique) package [96].

The NEST package can be understood as a collection of models that predict the response of noble gas elements, modeling the scintillation, ionization and electroluminescence processes as a function of the particle and interaction type, electric field and energy. These predictions are made based on calibrations and science data from different detectors as well as theoretical models.

The light yield, in Figure 3.11 and Figure 3.12, is exhibited in photons/keV and the charge yield in electrons/keV and both yields are shown as a function of the total energy and the electric field. Figure 3.11 shows the predictions of NEST to the light and charge yields of a gamma-ray interaction with the liquid xenon, while in Figure 3.12 it is of a neutron interaction with the liquid xenon. In Figure 3.11, the light and charge yields are anti-correlated as expected, and their sum is a constant. As the field increases the recombination is suppressed which results in more electron/keV and less photons/keV. Thus, the scintillation light is maximized when no electric field is applied. In the NR case, Figure 3.12, the light and charge yields are still modeled as anti-correlated, but unlike the ER case, their sum is not a constant, due to loss of energy into the heat channel.

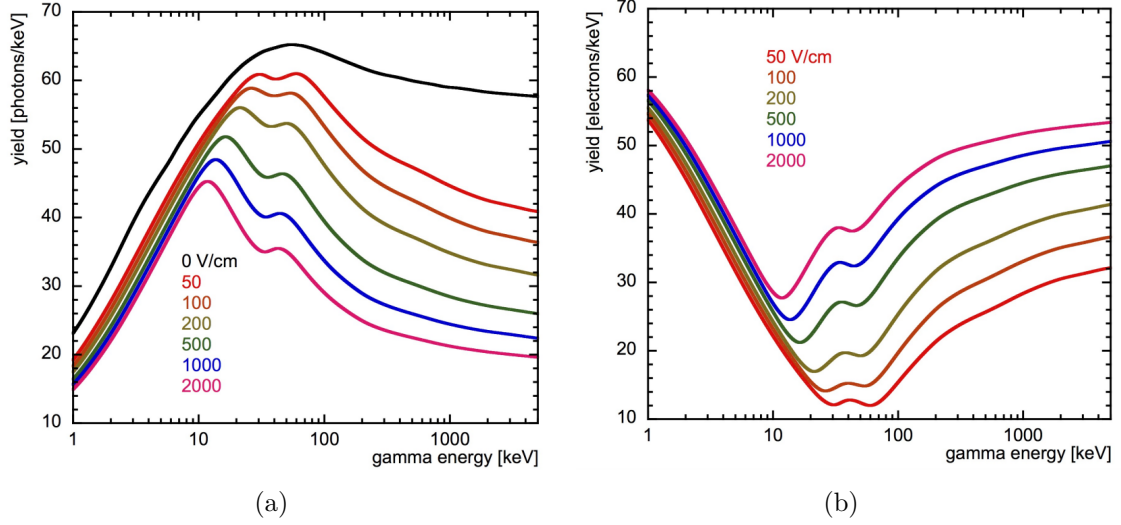


Figure 3.11: NEST predictions of the light (a) and charge (b) yield of ER interactions in several field strengths. Figure from [99].

This way of processing the information has the advantage of speed, allowing to simulate large sets of statistical data to predict the background rate and also the sensitivity of the experiment to various physical processes.

The other way of processing the information coming from BACCARAT is to create a full simulation of all the resulting signals of an interaction, namely, the VUV photons, the ionization electrons, and the scintillation light created in the OD. Like in the previous chain, the NEST package is employed to calculate the number of primary photons and ionization electrons resulting from the interactions. The QuickField model [100] is also employed with the aim of predict the drift time and the radial locations of the ionized electrons because the S2 hit pattern tightly depends on their trajectory.

The OD optical simulation is not trivial due to the complex geometry of the acrylic tanks, which is divided into 10 segments and the scintillation properties of the GdLS. Therefore, a modified version of GEANT4 called G4Scintillation was employed. In order to fine-tune this modified version the data of a small prototype detector was used, the liquid scintillator Screener [101], which was calibrated for several alpha decays, beta decays and gamma-rays.

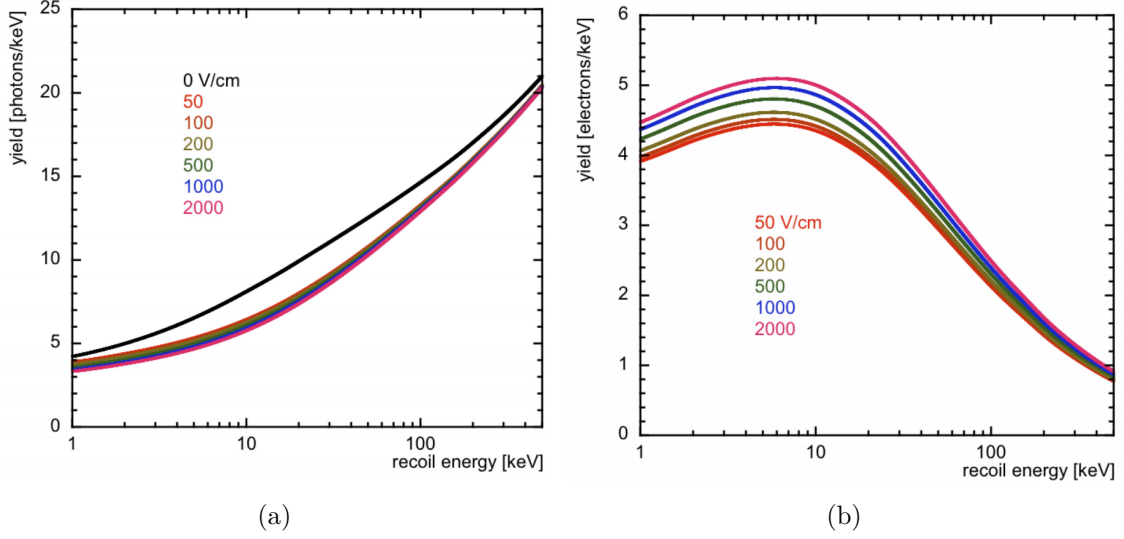


Figure 3.12: NEST predictions of the light (a) and charge (b) yield of an NR interaction in several field strengths. Figure from [99].

The information of the photons detected in each PMT is recorded and then translated into mock digitized waveforms through the Detector Electronics Response, DER, which is a package software that reads the file coming from BACCARAT and simulates the signal processing that is done by the frontend electronics and digitizers of LZ. All of the resulting simulations are intentionally organized and saved in the data acquisition system (DAQ) format to be as similar as possible to the actual data when they are analyzed through the LZ Analysis Package, LZap. LZap consists in a set of packages that processes and reconstructs the raw detector data so it can be used for physics analysis. LZap extracts the PMT charge and time information, applies some calibrations, identifies the type of interaction according to the S1 and S2 signals, performs the event reconstruction, and produces the reduced quantity, RQ, files for higher level analysis. Even though this second chain is much more elaborated and computationally heavy, it makes the analysis of the simulated data far more realistic. Both of these two chains are summarized in Figure 3.13 [93].

In our analysis, we used the first method. It included radioactive decays throughout the several components of the detector and in the liquid xenon. The simulations of uniform backgrounds, such as the ^{136}Xe double beta decay, the ^{85}Kr

beta decay and the solar neutrino rate, are obtained directly from a deposited energy spectrum passed to NEST, do not derive from BACCARAT. It was used, mostly, the 9.5 version of GEANT4. However, for some more recent simulations, like the radon ones, it was used version 10.2.

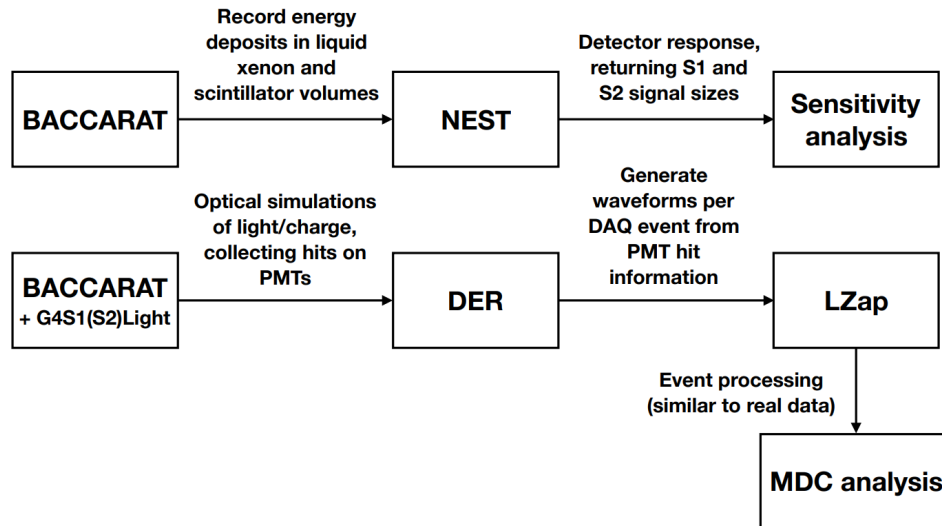


Figure 3.13: The two possible processing chains for the simulations used to obtain the sensitivity analyses and also the fake dataset used in the Mock Data Challenges. Figure from [93].

Chapter 4

Sinal and Background Models

In the present chapter, we will begin by understanding the signal model of the various decay modes of ^{124}Xe , followed by the description of the several background sources (internal, external and irreducible) to which the LZ detector is exposed.

For each event, GEANT4 simulates the values of energy deposited in the various parts of the detector and then, with NEST, it is calculated the respective S1 and S2 signals associated to the event.

Lastly, the analysis cuts applied to the simulated data in order to maximize the signal to background ratio are presented.

4.1 Signal Model

The stability band represents the elements that have a 1:1 ratio of the number of neutrons to the number of protons in the nucleus, for low atomic masses. As the atomic number increases so does the repulsion of the protons from electrostatics, then we need more neutrons to overcome it. Due to this, the ratio grows to approximately 1,5:1 for the very heavy elements. This band can be used as a criteria whether an element is stable or not.

When a nucleus lies below the band stability, is proton-rich [102], it will decay so as to reduce the number of protons and increase the number of neutrons. Therefore, it can decay by electron capture - combining an inner shell electron with a proton resulting in a neutron accompanied by a neutrino (represented by Equation 2.13)-, or by positron emission, when the nucleus emits one positron accompanied by a

neutrino (represented by Equation 2.12).

For some rich-proton nuclei, the transition $(A,Z) \rightarrow (A,Z-1)$ is not energetically favorable or even not possible, so the transition $(A,Z) \rightarrow (A,Z-2)$ can happen, namely, the double electron capture, electron capture with positron emission or double positron emission [61]. These decay modes were already explained in Chapter 2.3 and are represented by Equations 2.16, 2.20 and 2.22, respectively. The fact that these are second order processes means that the decays are expected to be extremely rare and so have very long half-lives. For example, so far, the double electron capture has been observed only in ^{78}Kr ($T_{1/2}^{2\nu KK} = (9.2_{-2.6}^{+5.5} \text{stat} \pm 1.3_{\text{syst}}) \times 10^{21}$ years) [103], ^{130}Ba ($T_{1/2}^{2\nu 2EC} = (2.2 \pm 0.5) \times 10^{21}$ years) [104, 105] and recently in ^{124}Xe ($T_{1/2}^{2\nu KK} = (1.8 \pm 0.5_{\text{stat}} \pm 0.1_{\text{syst}}) \times 10^{22}$ years) [106].

Natural occurring xenon, a heavy rare gas, is made of five stable isotopes, ^{128}Xe , ^{129}Xe , ^{130}Xe , ^{131}Xe , ^{132}Xe , and four slightly radioactive, ^{136}Xe , ^{124}Xe , ^{134}Xe , ^{126}Xe , with extremely long half-lives. The main decay channel of the isotope ^{124}Xe is the double electron capture. However, as it only has an abundance of 0.095% [107], meaning that a large volume of natural xenon is needed to obtain a significant mass of ^{124}Xe . Therefore, the LZ detector contains a total of 10 tonnes of liquid xenon within the cryostat, of which 7 tonnes are inside the TPC being an active mass. Consequently, there are about 9.5 kg of ^{124}Xe to study its possible decays, but only 6.65 kg in the active region at any given moment.

Given its high Q-value, the ^{124}Xe nucleus can decay by the three different two neutrino double beta decay channels available: the double electron capture ($2\nu 2EC$); electron capture with coincident positron emission ($2\nu EC\beta^+$); and double positron emission ($2\nu 2\beta^+$).

The double electron capture of ^{124}Xe can be written as,



The ^{124}Xe double electron capture itself can occur, mainly, via three different modes depending from which shells the electrons are captured. The most probable one is the KK-mode in which both electrons are captured from the K-shell, leaving the ^{124}Te daughter atom with two vacancies in the K-shell. The ^{124}Te nucleus

de-excites by emitting atomic X-rays and/or Auger electrons, releasing an energy of 64.6 keV [107]. The KL-mode happens when one of the captured electrons is from the K-shell and the other from the L-shell, releasing 36.7 keV, by contrast the LL-mode takes place when both electrons are captured from the L-shell and the released energy is roughly 9.8 keV [108].

The KK-mode happens roughly about 75% [108] of the time. The other two modes have much lower branching ratios which means that they are less likely to take place, the KL-mode happens roughly in 23% [108] of the double electrons captures and the LL-mode in 1.7% [108].

So far, the only mode of the ^{124}Xe double electron capture observed was the one in which both electrons are captured from the K-shell ($2\nu\text{KK}$). Its experimental half-life measurement was obtained by the XENON1T experiment and it is $T_{1/2}^{2\nu\text{KK}} = (1.8 \pm 0.5) \times 10^{22}$ years [106], which is in agreement with the current theoretical predictions [109–111]. The XENON1T experiment, located at the Laboratori Nazionali del Gran Sasso (LNGS) in Italy, operated from 2016 to 2018. It was designed to detect dark matter utilizing a dual-phase (liquid-gas) xenon time projection chamber. The detector was filled with 3.2 tonnes of liquid xenon, of which 2.0 tonnes served as a target for the particle interactions [112].

It is nearly impossible to detect the nuclear binding energy Q released in the process, $Q=2864$ keV, carried by the two neutrinos which easily escape the detector. Moreover, the NR energy of the recoiling ^{124}Te is about 30 eV, which is well below the LZ detector threshold (~ 1 keV). Consequently, only the X-rays and Auger electrons can be measured. Thus, the total energy deposits are 64.6 keV, 36.7 keV and 9.8 keV, which corresponds to the binding energies of the respective shells. In the particular case in which both electrons are captured from the K-shell only 64.3 keV can be detected because the energy depositions at the end of the cascade are too small to produce ionization or scintillation in the xenon [107]. The same is expected for the other two modes and the energy will be measured when these signals are observed.

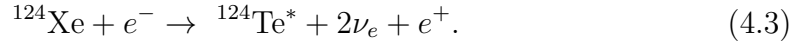
The half-life of each mode, $T_{1/2}^{2\nu x}$, can be obtained by simply rescaling the half-life of the double electron capture, $T_{1/2}^{2\nu 2EC}$, depending on the probability of each mode,

$$T_{1/2}^{2\nu x} = \frac{T_{1/2}^{2\nu 2EC}}{f_x}. \quad (4.2)$$

where $T_{1/2}^{2\nu 2EC} = (1.4 \pm 0.4) \times 10^{22}$ years [61] and f_x is the branching ratio of each mode.

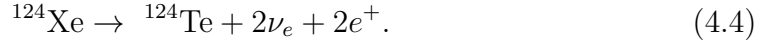
Combining the measured half-life of the KK-mode ($T_{1/2}^{2\nu KK} = (1.8 \pm 0.5) \times 10^{22}$ years [106]) and its branching ratio ($f_x = 0.75$ [108]) we can obtain the half-life of the double electron capture, through Equation 4.2, as being $T_{1/2}^{2\nu 2EC} = (1.4 \pm 0.4) \times 10^{22}$ years [61].

The ^{124}Xe $2\nu EC\beta^+$ decay can be written as,



Assuming that the captured electron is from the K-shell, which is the most likely to happen, the energy will be released by the production of X-rays and/or Auger electrons with a total energy of 31.8 keV [113]. But in this case this small signal will be accompanied by the positron energy spectrum and the consequent two back-to-back 511 keV gamma-rays from its annihilation.

The last possible decay of ^{124}Xe is the double positron emission decay, $2\nu 2\beta^+$, which can be written as,



Upon thermalization, both emitted positrons annihilate with two atomic electrons leading to the creation of four 511 keV gamma-rays which are emitted as back-to-back pairs.

In this work we focused on the study of the double electron capture modes only, but LZ is expected to be competitive in the search for the other two decay modes.

It is worth mentioning that ^{126}Xe , which has a natural abundance of 0.089% [107], can only decay via double electron capture, as shown in Equation 4.5 with a Q-value of 919 keV [107]. Since its Q-value is much smaller than the 2864 keV Q-value of ^{124}Xe decay, it is expected to be much less likely to occur,



The total decay rates, and hence the inverse half-lives, are strongly correlated with the Q-value and proportional to the phase space factor as shown in Equation 2.24. In the case of double electron captures with emission of two neutrinos the phase space factor varies with Q^5 [107]. Due to the high Q-value of the ^{124}Xe double electron capture and the Q^5 dependence, the total decay rate in the signal region will be dominated by this decay.

4.2 Background Expectations

In a rare event experiment, the background levels have to be reduced as much as possible in order to maximize the sensitivity of the detector. Thus, the main concern in LZ, and in all rare event detection experiments, is to reduce or reject the backgrounds.

The backgrounds present in LZ can be divided in two main categories: those coming from the outside towards the inner liquid xenon (e.g. cosmic-rays, gamma-rays from the cavern rocks or the detector materials); and impurities mixed in the liquid xenon.

To minimize the cosmic-ray background as much as possible, the detector is installed 1478 m underground [78], as shown in Figure 3.1, at the SURF, South Dakota, USA. One of the main reasons to locate the detector underground is the reduction of the muon flux, which is generated by the interaction of cosmic-ray particles in the upper atmosphere producing muon showers. The placement of the detector underground attenuates the muon flux by about five orders of magnitude in comparison to the sea level [114, 115]. The detector is also surrounded by a water tank of 6.1 m high and 7.6 m diameter, with ultra-pure water, providing a powerful shielding from the environment radiation, namely radioactivity in the cavern rock which leads to the emission of gamma-rays and neutrons. Additionally, 6 octagonal steel plates of 5 cm thickness, embedded between the concrete floor and the bottom of the water tank, and a top steel plate help to further reduce

these external backgrounds [78].

Another source of shielding comes from the self-shielding property of xenon which arises from the large number of protons ($Z = 54$) and its high density ($\rho = 2.942 \text{ g/cm}^3$ [116]). Therefore, the inner volume of the detector is very low in external background, because the gamma-rays coming from the outside travel only a few centimeters or even millimeters, depending on their energy. Xenon TPC technology provides an accurate position reconstruction, with centimeters resolution in the horizontal plane and millimeters precision in the vertical axis, even for low energy depositions, which allows for the discrimination of most of the external background based on the position of the interaction. The fiducialization process defines the fiducial volume in order to maximize the fraction of the overall target volume while suppressing the background as much as possible, maximizing sensitivity. Due to the self-shielding property of xenon this fiducial volume is fixed in the innermost region, as will be seen in Section 4.3. Furthermore, the active veto systems of the LZ (the outer layer of 2 tonnes of liquid xenon known as the liquid xenon skin and the 17 tonnes of gadolinium-doped organic liquid scintillator), help reduce backgrounds even further.

As can be seen in Figure 3.8, the several sources of background either produce ER or NR events. The ER background events are generated by gamma-rays or beta particles and the NR ones come from neutrons. For our study, the latter are irrelevant since we are searching for the ^{124}Xe double electron capture through its X-rays and/or Auger electrons (ER interactions) only.

4.2.1 External Backgrounds

Detector Materials

A substantial part of the total background comes from the construction materials which contain traces of ^{238}U , ^{232}Th , ^{40}K and ^{60}Co . The decay chains of ^{238}U and ^{232}Th are particularly threatening, since they contain several alpha, beta and gamma decays. The gamma-rays may have energies up to 2447.7 keV (^{214}Bi) and 2614.5 keV (^{208}Tl) in the ^{238}U and ^{232}Th chains, respectively, and can reach the inner xenon target and generate ER backgrounds even in the fiducial volume [117].

The alpha particles can interact with the materials and produce neutrons through (α , n) reactions leading to NRs. However, due to the small mean attenuation length of the liquid xenon, these neutrons do not produce a significant background, as they are very likely to produce multiple scatters in the detector and are thus easily identified. The OD veto further reduces the remaining single scatter neutrons by >95% [118].

Furthermore, these decay chains include isotopes with half-lives ranging from milliseconds to billions of years, and thus will be a constant background throughout the lifetime of the experiment. To a greater or lesser quantity all detector materials are contaminated with these isotopes. The most dangerous components are the ones closest to the active region of the detector. As such, the dominant background rates come from the cryostat, due to the large amount of material required and its proximity to the liquid xenon target, and from the PMT systems, also because of the closeness to the target.

In order to suppress the background coming from these contaminations, an extensive material screening campaign was carried out with the intention of choosing the purest materials for the detector components. This campaign used various techniques with the intention of identifying and characterizing the radioactive species, in particular, gamma-ray spectroscopy with High Purity Germanium detectors (HPGe), Inductively-Coupled Plasma Mass Spectrometry (ICP-MS) [119] and Neutron Activation Analysis (NAA). [78, 120]

The contamination levels determined for all the materials, used in the detector during this campaign, are used to normalize the simulations for each source.

The rock in the Davis cavern also contains ^{238}U , ^{232}Th and ^{40}K . Actually, the gamma-ray flux from the surrounding rock is $1.6 \pm 0.4 \text{ cm}^{-2}\text{s}^{-1}$ for gamma-rays with energies up to 1 MeV, $0.30 \pm 0.08 \text{ cm}^{-2}\text{s}^{-1}$ for 1 to 2 MeV and $0.05 \pm 0.01 \text{ cm}^{-2}\text{s}^{-1}$ above 2 MeV [121]. The water tank prevents most of these gamma-rays from reaching the active region, reducing its flux by several orders of magnitude. However, due to the large mass of rock and its high radioactivity, although only a small fraction interacts in the active region, it is still a relevant background source.

4.2.2 Internal Backgrounds

Internal backgrounds can be produced by neutron activation of xenon isotopes and by contaminants present in the xenon itself.

Activation Products

Radioactive isotopes can be produced through activation of xenon by environment neutrons from natural radioactivity and cosmic-ray muons [78], which can generate neutrons through the interaction with the laboratory rocks and the water tank, and their decays constitute a source of background. Neutrons from the cosmic-ray muons can be produced by the following processes:



where X and X' are different nuclei. The last four simplified reactions represent, respectively: a spallation reaction induced by a high energy muon, which results in nuclear disintegration; a muon capture by a proton; a photo-disintegration process, in which an atomic nucleus absorbs a high energy gamma-ray, from the electromagnetic showers that were triggered by a muon (the nucleus enters in an excited state, and immediately decays by emitting a neutron); a similar process to the last one but in hadronic cascades that were initiated by a muon.

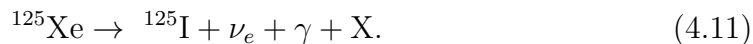
Thanks to the detector being situated 1478 m underground and also inside the water tank, the flux of muon induced neutrons is highly reduced, and as a result xenon activation inside the TPC is negligible. The xenon in the circulation system can be activated because it is outside the water tank. However, these backgrounds are negligible since the xenon mass is small (<70 kg at any given moment in the xenon tower).

Another source of activation comes from the calibrations performed using neutron sources (AmBe, AmLi and ^{88}YBe [93]) and the deuterium-deuterium neutron generator to study the response of the detector to NRs.

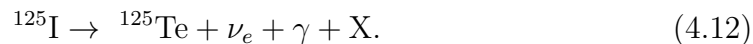
Due to all the processes described above, several unstable isotopes, like ^{125}Xe ($T_{1/2} = 16.9$ hours), ^{127}Xe ($T_{1/2} = 36.4$ days), ^{129m}Xe ($T_{1/2} = 8.9$ days), ^{131m}Xe ($T_{1/2} = 11.9$ days) and ^{133}Xe ($T_{1/2} = 5.3$ days) are produced [78]. All of these isotopes will decay away quickly, and do not produce energy depositions close to our signals. The most concerning for our study is the ^{125}Xe originated from [107]:



The decay process of ^{125}Xe is an electron capture to an excited state of ^{125}I which results in an orbital vacancy followed immediately by the decay of ^{125}I to its ground state. Electron transitions will fill the vacancy and produce X-rays and/or Auger electron cascades, represented by X in Equation 4.11,



^{125}I then disintegrates by electron capture via the excited level of 35.5 keV of ^{125}Te into the ground state of ^{125}Te [122], as illustrated in Figure 4.1 and represented in Equation 4.12 with a half-life of approximately 59.39 days [122],



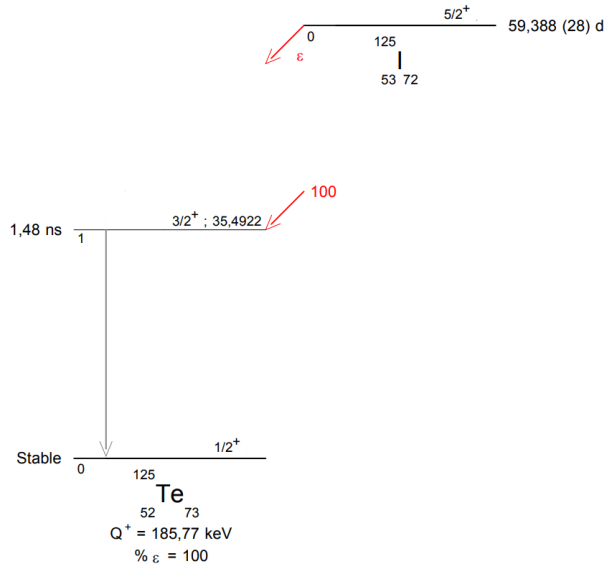


Figure 4.1: Decay scheme of ^{125}I . Figure from [122].

About 80% of electron captures come from the K shell. The resulting atomic de-excitation together with the gamma-ray from the nuclear de-excitation, leads to a total energy deposit of 67.3 keV, very close to the energy deposit of the double electron capture from the K shell of ^{124}Xe (64.3 keV). With its long half-life, ^{125}I could become a very serious background for this study. Fortunately, as already observed in LUX [107], ^{125}I is removed by the purification system with a time constant of only a few days, making this a negligible background, shortly after the neutron calibrations.

Contaminants Mixed in the Xenon

As already mentioned, all detector materials contain small traces of the ^{238}U and ^{232}Th isotopes that contain in their chains ^{222}Rn ($T_{1/2} = 3.8232$ days [123]) and ^{220}Rn ($T_{1/2} = 55.8$ seconds [124]). Hence, radon is constantly being produced in the detector materials. Being a gas, it can diffuse in the materials, and for materials in contact with the internal TPC can enter the liquid xenon reservoir and distribute itself [125].

If the radon is produced directly on or below the surface, the received recoil energy in the alpha decay of its mother nuclide, radium, is enough to eject it out of the material and consequently entering the liquid xenon. Besides that, the entry

of radon into liquid xenon can also occur due to its diffusion through the material. Radon diffusion is highly dependent on the properties of the material, namely the chemical and lattice structures, density, surface roughness, and temperature. The diffusion length is defined as $L = \sqrt{D\lambda}$ where L is the average distance traveled by the nucleus before decaying, D is the diffusion coefficient and λ the decay constant [126]. Since the half-life of ^{222}Rn is significantly longer than that of ^{220}Rn , the amount of ^{220}Rn atoms that reach the liquid xenon before they decay is highly suppressed.

In both of these cases, the radon emanates gets mixed with the xenon, and produces background events throughout its decay chain, which, unlike the external backgrounds, is not reduced by the self-shielding property of xenon. There is yet another source of radon emanation coming from the environmental dust deposited on detector surfaces which may produce daughter decays into the liquid xenon [126].

In order to achieve an estimation of the concentration activity of ^{220}Rn and ^{222}Rn due to emanation all the materials interact with xenon were assayed in dedicated setups at room temperature. The expected equilibrium activities are $1.8 \mu\text{Bq/kg}$ and $0.09 \mu\text{Bq/kg}$ for ^{222}Rn and ^{220}Rn , respectively [118]. The emanation decreases as the temperature drops and this effect is already considered in the estimates for radon emanation.

Two major sources of background, for our study of ^{124}Xe double electron capture, are originated due to radon emanation into the liquid xenon. One important source of background is the beta decay of ^{214}Pb into the ground state of ^{214}Bi (in the ^{222}Rn chain), with a 1019 keV endpoint and a branching ratio of 9.2% [127]. Since no gamma-ray is emitted, it is a naked beta decay, and it is not possible to reject it through the multiple scatter cut that will be described in Section 4.3. Nevertheless, decays to other energy levels, even if accompanied by gamma-ray emissions, can also be dangerous, since the gamma-ray can leave the detector undetected if it has enough energy to escape and the decay happens close enough to the detector borders.

The same thing can happen when the beta decay of ^{212}Pb to the ground state of ^{212}Bi occurs [128], which has a branching ratio of 13.3% and a 569.9 keV endpoint

[128]. However, the background coming from this decay is much lower than the previous one because the concentration activity is much smaller due to the shorter half-life of the ^{220}Rn .

Finally, the other source of background due to radon derives from the ^{222}Rn daughters being able to plate-out on the surfaces of the detector during its construction (particularly ^{210}Pb which has a long half-life of $T_{1/2} = 22.23$ years [129]). In this case, the most concerning daughter is the metal ^{210}Po since the alpha particle resulting from its decay can cause (α, n) reactions in the detector materials. As in the case of PTFE, which due to its high flourine content has a neutron yield of 9.48×10^{-6} neutrons/ α [78, 130]. Moreover, the decay of ^{210}Pb on the surfaces may release its daughter ^{210}Bi into the liquid xenon, where it may create naked beta decays to the ground state of ^{210}Po . Since the ^{220}Rn chain does not include such long-lived isotopes, like the ^{210}Pb in ^{222}Rn chain, ^{220}Rn daughters will not contribute to the surface contamination.

Natural xenon contains trace levels of ^{39}Ar and ^{85}Kr . Both dissolve in the liquid xenon and are beta emitters: ^{39}Ar has an endpoint energy of 565 keV and a half-life of 268 years [131], while ^{85}Kr has an endpoint energy of 687.1 keV and a half-life of 10.752 years [132]. These decays lead to ER events, that either can or can not be accompanied by gamma-rays. Even though their long half-lives, they can be quite dangerous. Since the ^{39}Ar beta minus decay is purely a naked beta decay [131], *i.e.* no gamma-ray is emitted, and the ^{85}Kr beta minus decay mode, in which a gamma-ray, is emitted has a 0.438% branching ratio. Of these two, the ^{85}Kr is the one that produces more background events due to its half-life being smaller than the one of ^{39}Ar .

In the case that no gamma-ray is emitted or it escapes the active volume and the vetoes, it is not possible to tag these events and they become a source of background. In order to remove Krypton and Argon from xenon, LZ has installed a xenon purification system using chromatography ([133]), which filters xenon before it enters the detector. Commercial xenon typically contains up to hundreds of ppb of ^{nat}Kr but after being processed by the chromatography system this contamination is expected to reduce the $^{nat}\text{Kr}/\text{Xe}$ concentration to 0.3 ppt g/g.

4.2.3 Irreducible Physical Background

Given its extremely high sensitivity, physics processes that until recently were considered rare and very difficult to detect now constitutes significant backgrounds to LZ.

Despite its very long half-life ($T=2.165 \times 10^{21}$ years [134]), the double beta decay of ^{136}Xe , with an endpoint $Q=2457.83$ keV [135], is one of the most important background sources in LZ.

Neutrinos can interact in xenon either via elastic interactions with the electrons, creating ER events, or through coherent neutrino nucleus interactions, producing NR events. As mentioned earlier, for our study, we are only interested in ER backgrounds, which are dominated by neutrinos from the pp reaction, ^7Be and CNO chain [136]. Since the other sources of neutrinos have much lower fluxes their contribution to the ER background is negligible, as shown in Figure 4.2. The predicted event rate of each neutrino source, in Figure 4.2, was calculated assuming the oversimplification of reality that the electrons are free. Due to the existing binding effect it is expected the suppression of the cross section, mostly the cross section of solar neutrinos with lower averaged energy [137], and consequently their event rates. Corrections to the binding effect only become relevant at very low energies, in this study it would only affect the LL decay mode.

Some sources produce neutrinos with enough energy to produce NR events with energies above the detector threshold [138], but these are not included in our background model. The NR events from neutrinos are mainly from solar hep and ^8B , diffuse supernova neutrinos and atmospheric neutrinos.

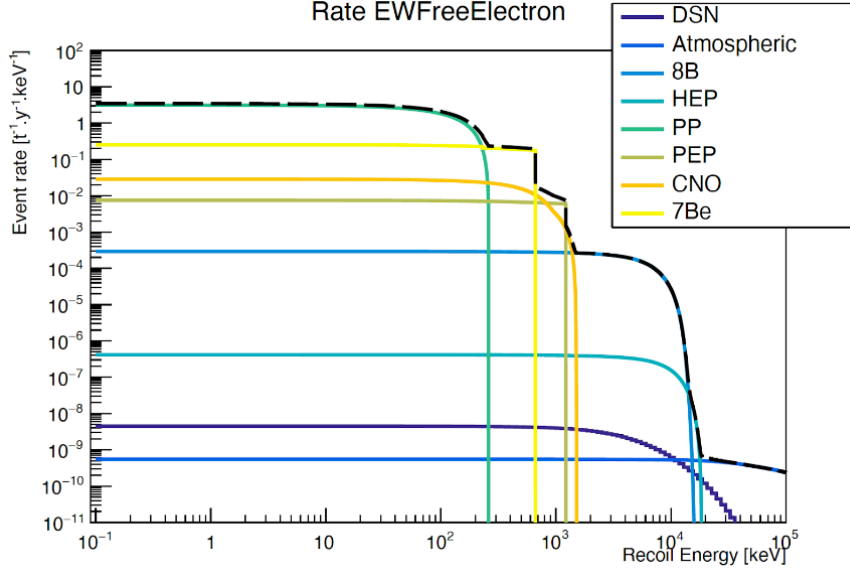


Figure 4.2: Rate of the several sources of neutrinos that interact in xenon via the elastic scattering with electrons. The main contribution comes from the pp reaction, ${}^7\text{Be}$ and CNO chain. These event rates were calculated assuming that the electrons are free. Binding effect corrections are only relevant at very low energy, and in this study would effect only the LL decay mode. Figure from [139].

4.3 Event Selection Criteria

As discussed in Section 3.3, the simulations of the background events that reach the LZ detector were obtained through the GEANT4-based BACCARAT software. It simulates the energy depositions, produced by the several background sources, throughout the detector. Then, the energy depositions are translated, through the NEST package, in primary scintillation photons (S1) and ionization electrons (S2), and classified as an ER or NR event. Due to processing and storage restrictions, instead of creating an S1 and S2 for each interaction in a given event, there is only one total S1 and S2 for the entire event, otherwise, the simulation would become extremely computationally heavy. Likewise, there is only one "global" interaction position (x,y,z) per event, corresponding to the energy weighted average position of all the interactions in the event. This simulated data, corresponding to tens to thousands of LZ lifetimes per ER background source, were officially produced by the collaboration for sensitivity and background studies during the construction of

the detector.

Most of the background events are excluded by applying a succession of selection criteria using the available data variables while maintaining a high acceptance for signal events.

For each event, several parameters are calculated like energy and location of the interaction in the TPC, the skin region and the OD among other parameters. For a full list of variables available for analysis see Appendix A.

The first selection criteria is the definition of a region of interest. As a first step, we focus on the low energy region, from 0 to 200 keV, to study the behaviour of the various backgrounds in this energy region. This cut also ensures that at least three PMTs observe S1. Additionally, it is also required that the total delayed scintillation signal, S2, is larger than 350 phe detected in the TPC region [78]. These two requirements are critical for the low energy region, but have no impact at the energy of our signals.

Finally, in the RFR (reverse field region) energy deposits from interactions only produce S1 signal. Therefore only a fraction of the energy deposited is detected. This additional S1 will merge with the one in the active region making S2/S1 smaller than if all the energy were deposited in the active region. By requiring that the energy deposited in RFR is less than that in the active region we are getting rid of events with energy at least in the same order as that of the active region - this is a reasonable cut as having half of the total energy deposited in the RFR will move the event to the outer region of the ER band, making it possible to exclude it with real data.

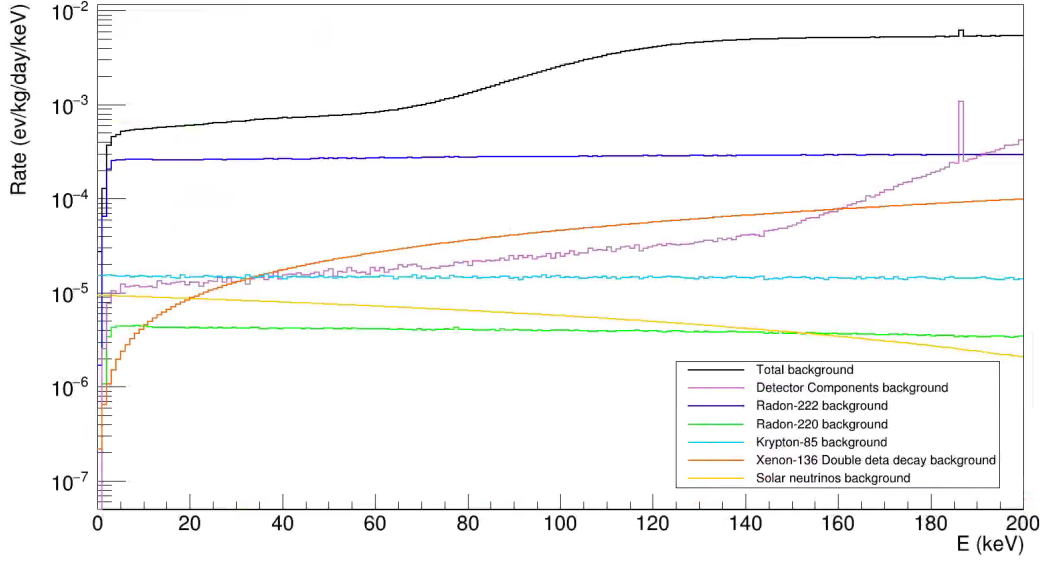


Figure 4.3: Total background and individual components in the region of interest.

Figure 4.3 shows the rate of simulated background events that survived this first cut from detector components (pink line), ^{222}Rn (dark blue line), ^{220}Rn (green line), ^{85}Kr (light blue), double beta decay of the ^{136}Xe (orange line), solar neutrinos (yellow line) and finally the sum of all these sources (black line).

The second cut is the single scatter selection. This cut is applied because we expect our signal to be point like given the position resolution of the detector, while many backgrounds will produce multi-site interactions (e.g. Compton scattering, beta decays accompanied by a de-excitation gamma). The energy weighted mean position is defined as

$$\langle x_E \rangle = \frac{\sum_i (E_i x_i)}{\sum_i E_i} \quad \langle y_E \rangle = \frac{\sum_i (E_i y_i)}{\sum_i E_i} \quad \langle z_E \rangle = \frac{\sum_i (E_i z_i)}{\sum_i E_i}, \quad (4.13)$$

where x_i , y_i and z_i are the positions of each interaction in the x, y and z direction, respectively, and E_i are the corresponding energy deposits. The energy weighted variance, in the radial and z direction, are thus defined as:

$$\sigma_r^2 = \frac{\sum_i E_i (r_i - \langle r_E \rangle)^2 \times \sum_i E_i}{(\sum_i E_i)^2 - \sum_i (E_i)^2} \quad \sigma_z^2 = \frac{\sum_i E_i (z_i - \langle z_E \rangle)^2 \times \sum_i E_i}{(\sum_i E_i)^2 - \sum_i (E_i)^2}. \quad (4.14)$$

The single scatter cut rejects multiple scattering events by requiring that the energy weighted standard deviations, σ_z and σ_r , of any event must be less than 0.2 cm in the vertical direction and less than 3.0 cm in the radial direction. These are expected to be conservative values for the resolution, even at these low energies, based on results from LUX [140].

From all of the background constituents presented in Figure 4.3, only some of them are affected by the single scatter cut, namely ^{222}Rn , ^{220}Rn , the detector components background and the ^{85}Kr . The remaining backgrounds, from neutrino interactions and the double beta decay of ^{136}Xe , produce single scatters.

The next analysis cuts also explore the topology of multi-interactions backgrounds. Both the skin and the OD can be used as vetoes, allowing the removal of events with coincident signals in the TPC and one (or both) of them. As with the single scatter cut, this removes multiple Compton interactions in the same event, and decays of internal contaminants with coincident gamma-rays that interact in one of the vetoes. Again, neutrino interactions and ^{136}Xe double beta decay are not affected by these cuts.

We used the same analysis cut used in the ^{136}Xe neutrinoless sensitivity analysis in which an event is vetoed if the energy deposited in the OD or the xenon skin is higher than 100 keV [117].

As illustrated schematically in Figure 4.4a, the beta decay of ^{214}Pb to ^{214}Bi mostly results in an excited state of ^{214}Bi . Therefore the beta decay is usually accompanied by a gamma-ray from the de-excitation of ^{214}Bi , in which case it can be effectively removed by the single scatter and veto cuts. However the ^{214}Pb can decay directly to the ground state of ^{214}Bi , with a probability of 9.2% [127], usually referred to as a "naked beta". In this case, there will not be any gamma-ray emitted, and thus it is impossible to exclude these events using the single scatter or the veto cuts.

The ^{214}Pb , from the ^{222}Rn chain, is not the only source of naked beta decays, since the ^{212}Pb , from the ^{220}Rn chain, can also generate them. As can be seen in 4.4b, the beta decay of ^{212}Pb is predominantly to an excited state of ^{212}Bi . However,

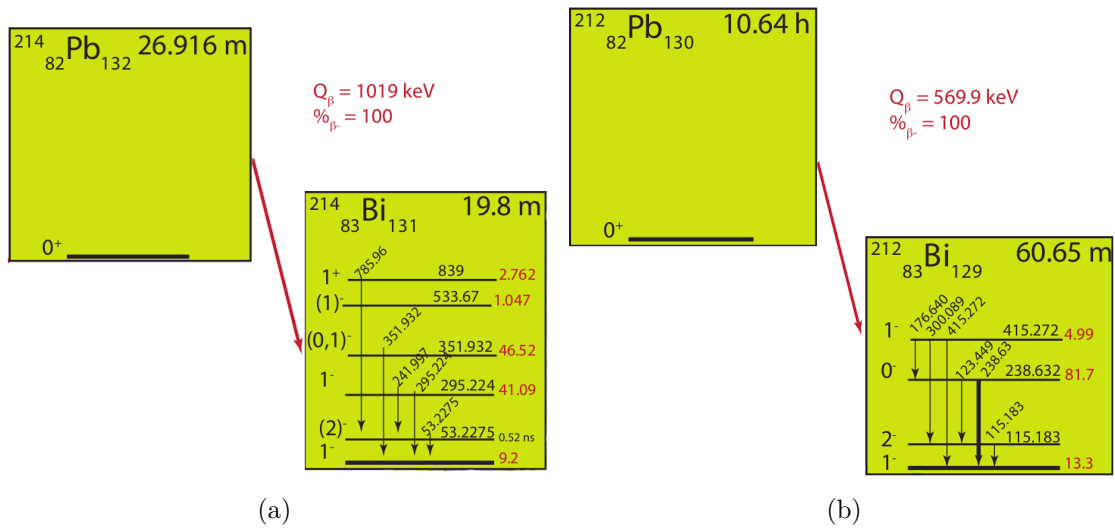


Figure 4.4: Decay scheme for ^{214}Pb , (a), and ^{212}Pb , (b).

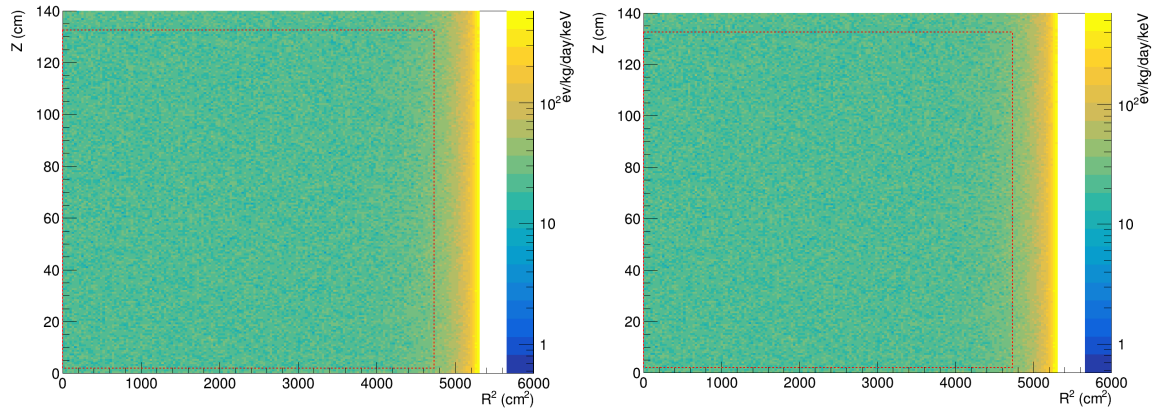
there is a 13.3% probability [128] of decaying directly to the ground state of ^{212}Bi with no emission of gamma-rays and, as in the previous case, being impossible to reject.

Most of these events, in which gamma-rays are emitted, can be removed through the single scatter cut, as can be seen in Figure 4.5b.

Despite this, not all of the released gamma-rays interact in the active volume, but they may interact in the skin or the OD. The closer to the TPC walls the decay occurs, the more likely the gamma-ray will get out of the active region without interacting, causing more events to survive the single scatter cut near the walls as we can see in Figure 4.5b. So, applying the OD and skin veto cut, the background events are highly reduced as can be seen in the plots shown in Figure 4.5c, 4.5d and 4.5e.

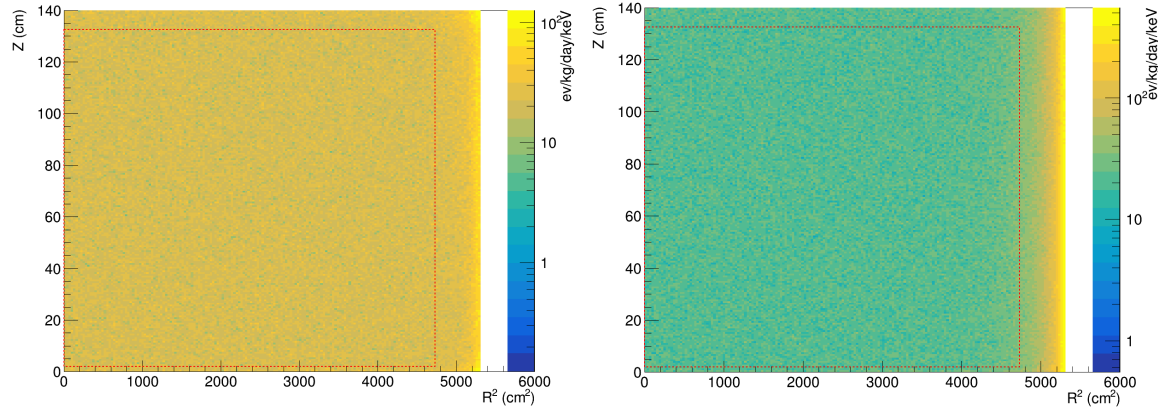
Another source of naked beta decays comes from the ^{85}Kr disintegration, which mostly occurs by a beta minus emission to the ^{85}Rb ground state, with a maximum energy of 0.675 MeV and no gamma-ray emission, as can be seen in 4.6.

There is another mode, much less probable with a branching ratio of 0.43%, which is also a beta decay but the electron carries a maximum energy of 173 keV followed by a gamma-ray emission with energy of 514 keV. Nevertheless, this mode



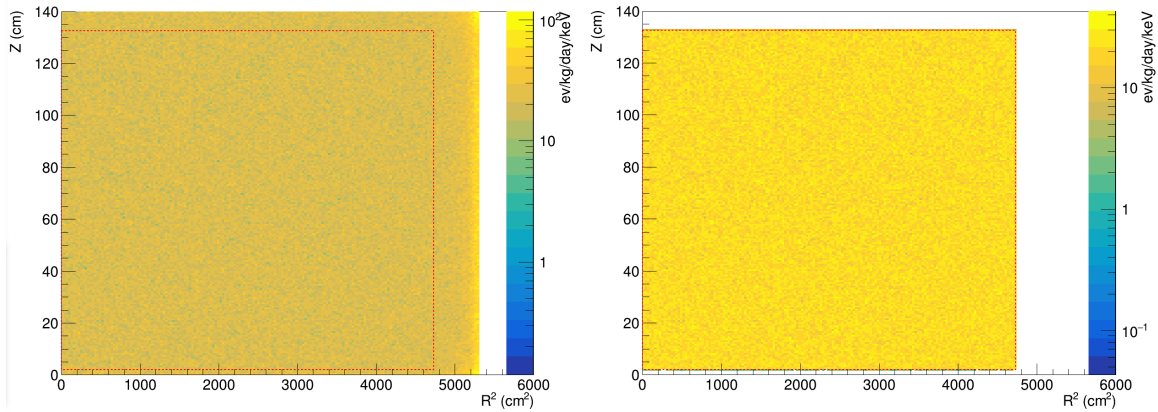
(a) All events in the region of interest.

(b) Single scatter events in the region of interest.



(c) Single scatter events in the region of interest with skin veto.

(d) Single scatter events in the region of interest with OD veto.



(e) Single scatter events in the region of interest with skin and OD veto.

(f) Events that survived all cuts.

Figure 4.5: Graphical representation of the background coming from the ^{222}Rn chain depending on the quadratic radial direction, R^2 , vs the vertical direction, z . The effects of applying the single scatter and veto cuts are visible in subfigures b)-e). Note the significant reduction in the (z) color scale with the successive application of the cuts. The fiducial volume cut is represented by a red dashed line.

is not relevant, not only because of its small branching ratio but also because due to the gamma-ray emission it can be excluded from the background through the single scatter cut very efficiently.

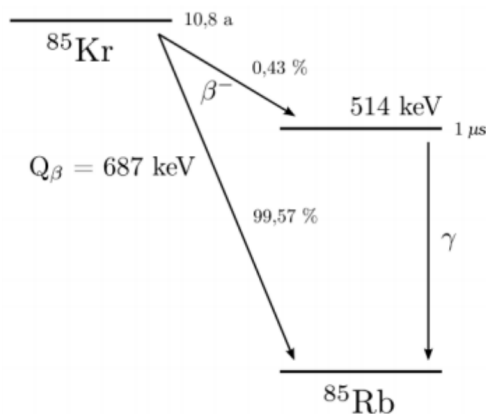


Figure 4.6: Decay scheme for ^{85}Kr .

The final cut is the fiducial cut. While a larger xenon volume supplies a greater exposure, the background rate increases significantly at the outer regions of the detector, as can be seen in Figure 4.7, in particular the external background generated by the detector components. Therefore, an optimization taking advantage of the self-shielding property of xenon needs to be considered.

The spatial distribution of the events with energies below 100 keV and passing through the single scatter and veto cuts is shown in Figure 4.7 as a function of the radial and z positions. It is clear that due to the self-shielding property of xenon, the central region has much fewer events than the edges of the TPC. It can also be seen that there are much more background at the top than at the bottom of the active volume which is due to the xenon present in the RFR. Trading off a reduced (fiducial) volume for a lower background rate will lead to an increased sensitivity to search for rare events.

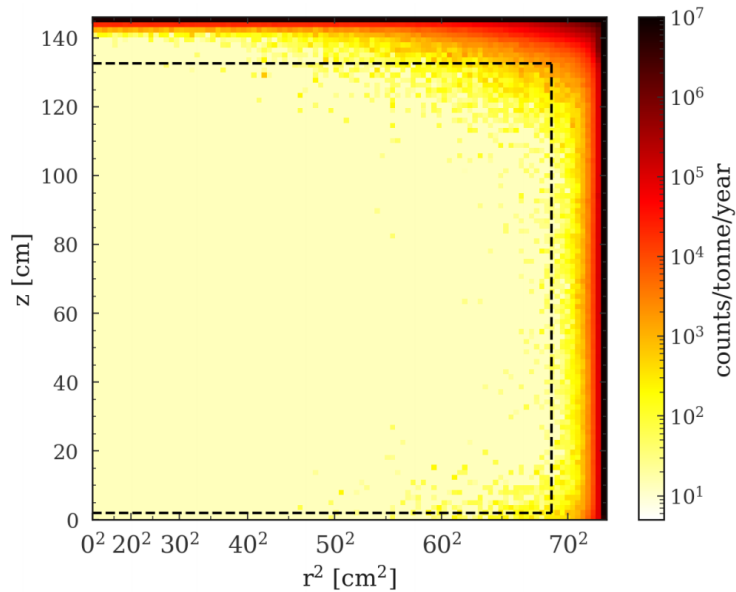


Figure 4.7: Spatial disposition of all ER backgrounds which survived to the single scatter and also the veto cuts, with energies up to 100 keV. The dashed black line represents the fiducial volume. Figure from [141].

In this work, the fiducial volume used is the same that was optimized for the WIMP search analysis [118], as our energy region of interest is similar. It is defined as a cylinder with a radius extending up to 4 cm from the TPC walls, and the height defined from 2 cm above the cathode to 13.5 cm below the gate. This corresponds to a cylinder with radius 68.8 cm and a height between 2 cm and 132.6 cm (the cathode coincides with the origin of the vertical coordinate, z). This fiducial volume corresponds to 5.6 tonnes of liquid xenon.

For the background coming from the ^{222}Rn , an additional cut must be applied. As the half-life of ^{210}Pb is significantly longer than the exposure time of the experiment ($T_{1/2} = 22.23$ years [129]), it is assumed that all of the ^{210}Pb is removed by the xenon purification system or attaches to the PTFE walls or grids before it decays, and therefore there will not be any background events from this sub-chain in the xenon bulk. Therefore, all events originating from ^{210}Pb and its progeny are removed from the analysis.

In summary, the analysis cuts applied in this work are:

- Definition of the region of interest: energy deposited being less than 200 keV; At least three PMTs observe S1 signal; At least 5 electrons are emitted

($S2 > 350$ phe) [78]; Energy deposited in the RFR is smaller than that deposited in the active region. ($(fLXeEDepER_keV + \frac{1.5}{6} fLXeEDepNR_keV) < 200 \ \&\& \ fLXeS1cTot_phe > 0 \ \&\& \ fLXeS2c_phe > 350 \ \&\& \ fRFRER_keV < fLXeEDepER_keV$)

- Single scatter cut: energy weighted sigma is less than 0.2 cm and 3.0 cm in the vertical and radial directions, respectively. ($fLXeSigmaZ_cm < 0.2 \ \&\& \ fLXeSigmaR_cm < 3.0$)
- Skin veto cut: energy deposited in the skin less than 100 keV ($fSkinEDep_keV < 100$)
- OD veto cut: energy deposited in the OD less than 100 keV ($fODEDep_keV < 100$)
- Fiducial volume cut: energy deposited inside a cylinder with radius 68.8 cm and a height between 2 cm and 132.6 cm. ($fLXeR_m < 68.8 \ \&\& \ fLXeZ_cm > 2 \ \&\& \ fLXeZ_cm < 132.6$)

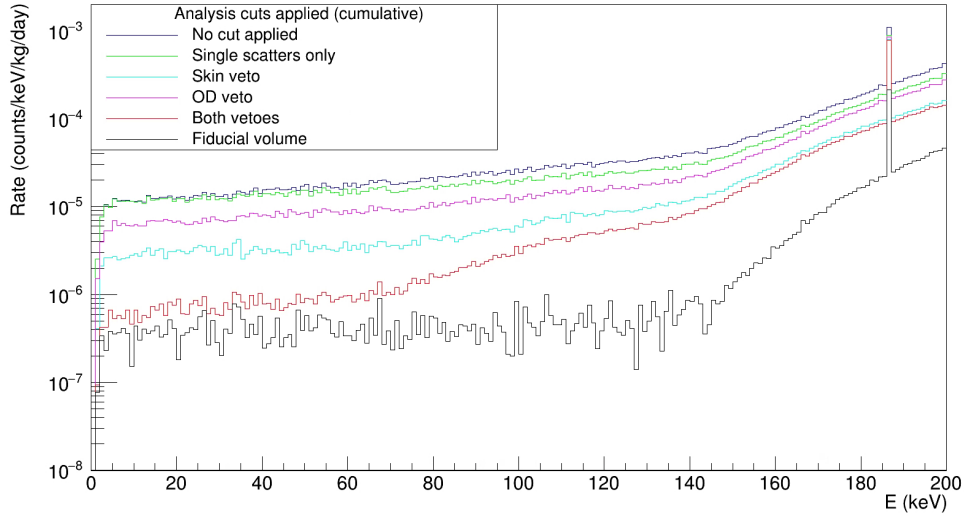


Figure 4.8: Effect of applying successive analysis cuts.

Figure 4.8 shows the effect of applying each cut in succession for the background events coming from the detector components, resulting in a decrease of almost two

orders of magnitude in the background rate in the region of interest for this study ($\lesssim 100$ keV).

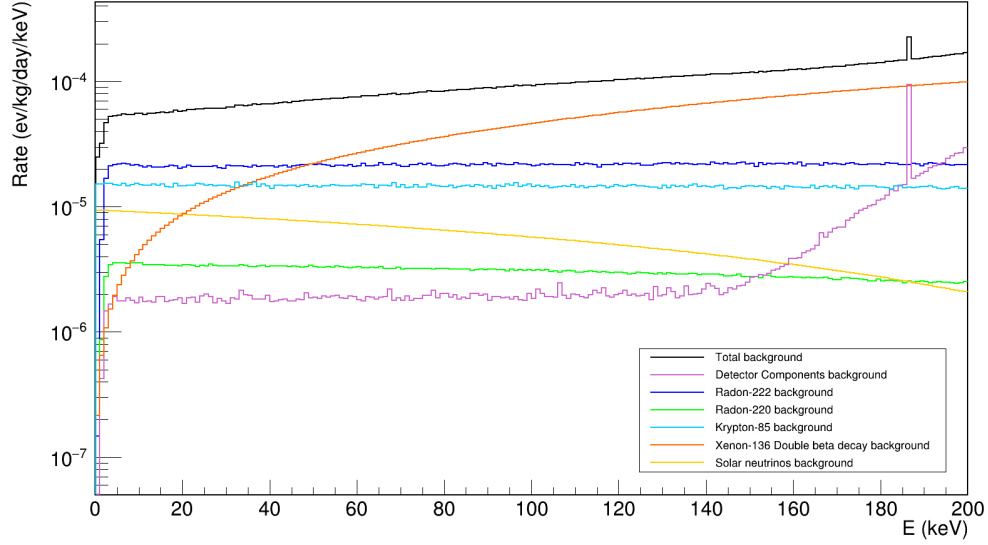


Figure 4.9: Total background and individual components.

Finally, 4.9 shows the expected energy spectrum, after all cuts, coming from all of the background sources. ^{222}Rn and the double beta decay of ^{136}Xe clearly dominate the background rate at these energies, closely followed by ^{85}Kr . With the application of the analysis cuts, the background from the detector components becomes almost negligible. Note that there is a significant increase in the rate of this background from the Figure 4.8 to Figure 4.9. This is caused by the inclusion of an upper limit of a possible ^{210}Bi population mixed in the xenon, resulting from the ^{210}Pb detaching from the walls and grids.

After establishing the expected signal for each mode of ^{124}Xe double electron capture, summing all the background sources and applying all the cuts to the simulated data we will use, in the next chapter, the Rolke method. The frequentist statistical approach of Rolke is employed to predict the sensitivity, observation and discovery potentials of the LZ detector for each mode.

Chapter 5

Statistical analysis and discovery potential projections

In this chapter, initially, it is presented and described the statistical method, Rolke, used to obtain the sensitivity, observation and discovery potentials of the LZ experiment to the three decay modes of ^{124}Xe double electron capture. Then, each mode is analyzed separately and the sensitivity, observation and discovery potentials for each of them are compared to the expected half-lives based on the XENON1T measurement. Lastly, it is presented a graphical representation of the expected background rate plus the signal of each mode, along with a table summarizing the background signal events in the ROI of each mode and the upper limits of signal events to achieve a 90% CL sensitivity, 3σ observation and 5σ discovery.

5.1 The Rolke Method

In order to determine the sensitivity, observation and discovery potentials for two neutrino double electron capture signatures the frequentist statistical approach of Rolke is employed [142]. TRolke is a C++ implementation of the Rolke method, used to calculate the frequentist confidence intervals using the profile likelihood method [142]. The package contains several routines for the calculation of upper and lower limits, taking into account uncertainties in background events estimates and signal efficiency [143]. The Rolke method provides seven different statistical

models with different combinations of binomial, gaussian, poissonian (or no uncertainties) for both the background error and the efficiency [143]. In our analysis, we assumed a gaussian error, due to the high number of background events, using its square root for the uncertainty. No systematic errors were considered for this initial analysis.

For the study of the sensitivity, a 90% CL was used. The Rolke method estimates the upper limit on the number of signal events that would still be compatible with the background level in the region of interest and its respective uncertainty at this CL. It can also provide estimates of the number of events required to claim an observation or a discovery, corresponding to 3σ and 5σ statistical significance, respectively. These limits on the number of signal events, μ , can be used to calculate the corresponding half-life of the decay by [107]:

$$T_{1/2}^{2\nu 2EC} = \frac{\ln(2)aN_A}{A} \frac{M\Delta T}{\mu}, \quad (5.1)$$

where a is the isotopic abundance for ^{124}Xe ($a = 0.095\%$), N_A is the Avogadro constant, M is the fiducial mass of xenon ($M = 5600$ kg), ΔT is the exposure time ($\Delta T \leq 1000$ days) and A is the respective molar mass ($A = 123.9$ g/mol).

For each mode, we can substitute the obtained limits on the number of signal events in Equation 5.1 and compare it to the expected half-lives in order to estimate the required exposure time, so that the LZ experiment reaches the 90% CL sensitivity, observation and discovery potentials.

However, the TRolke does not provide an uncertainty associated with its estimates. Therefore, we had to look for another approach to obtain an uncertainty associated with each value coming from TRolke.

We created a Gaussian distribution, with 500 points, where the mean value was the expected background in the ROI, for a certain decay mode and exposure time, and the standard deviation was the square root of the number of background events. Then, the TRolke was applied to each value of the Gaussian distribution in order to obtain the number of events required to reach a 90% CL sensitivity, and to claim an observation or a discovery. In the resulting Gaussian distributions the required number of signal events is the mean value and its uncertainty is the

standard deviation of the Gaussian distribution.

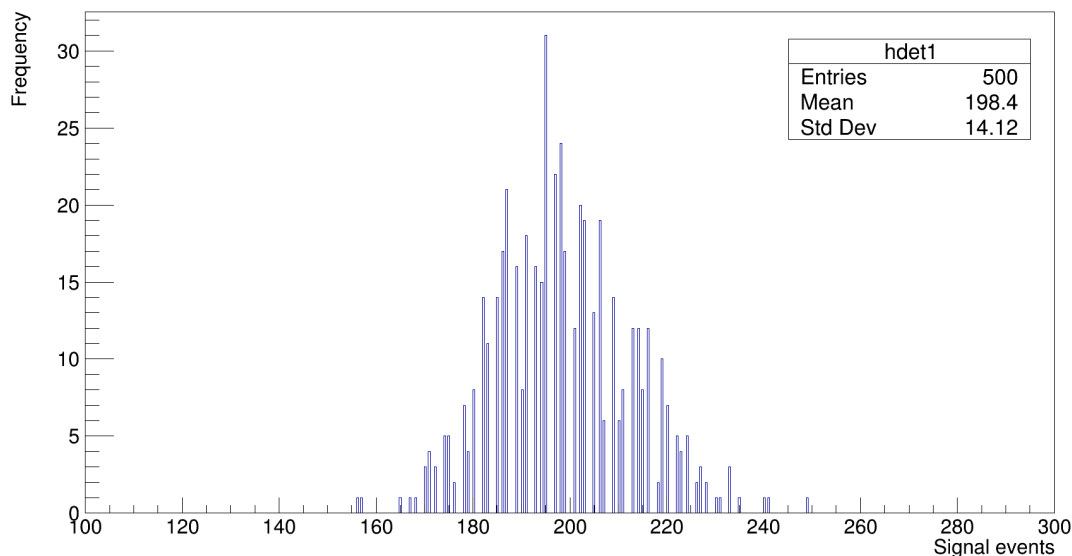


Figure 5.1: Gaussian distribution of the required number of signal events to claim a discovery of the LL-mode, for 75 days of exposing.

For instance, in Figure 5.1 it is illustrated the obtained Gaussian distribution of the required number of signal events to claim a discovery of the LL-mode, for 75 days of exposure. In this case, the required number of signal events to claim a discovery is 198 ± 14 .

5.2 Statistical Analysis of KK, KL and LL modes of ^{124}Xe Double Electron Capture

As already discussed in Section 4.1, the two-neutrino double electron capture has three main modes with different branching ratios. The most likely mode being when both electrons are captured from the K-shell (KK), with a branching ratio of 75%, followed by when one electron is captured from the K shell and the other from the L-shell (KL), with a branching ratio of 23%, and when both electrons are captured from the L-shell (LL), with a branching ratio of 1.7% [108].

The energy resolutions used in our analysis for the three decay modes, which ultimately drive the amount of background events in the respective regions of inter-

est used, follow the energy resolution curve obtained for the XENON1T detector [144]. Since it uses a similar technology to LZ and is of comparable size. Figure 5.2 shows the XENON1T fit for the energy resolution, XENON1T and LUX calibration points and the vertical lines represent the expected energy peak of each mode.

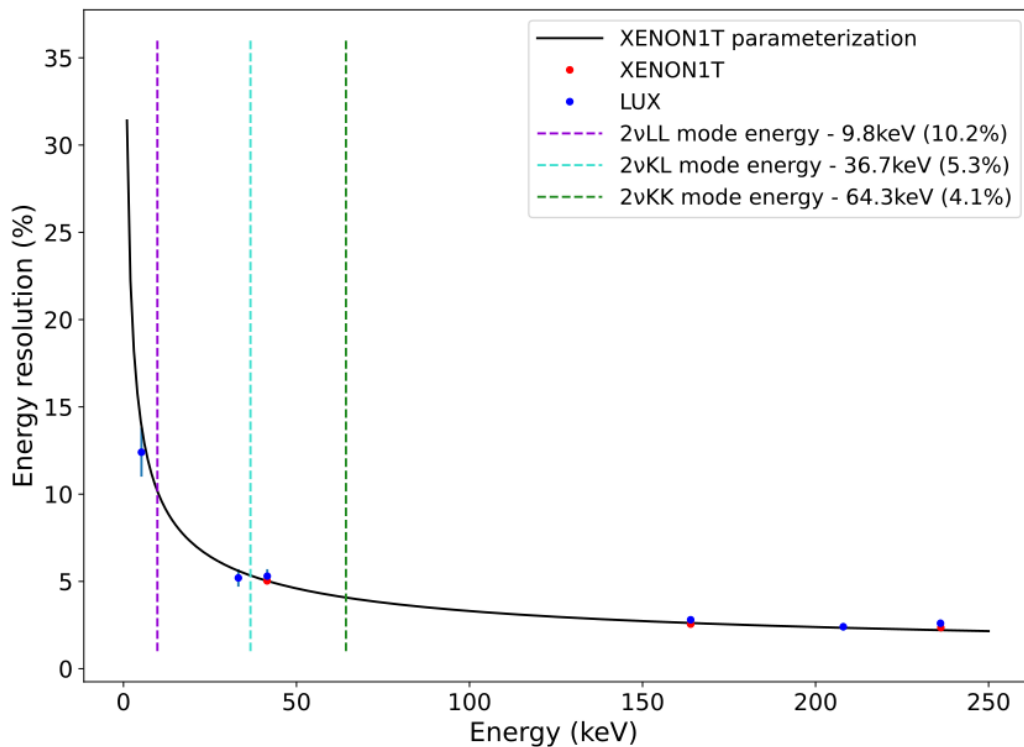


Figure 5.2: Energy resolution as a function of the energy for the LUX (blue) [145] and XENON1T (red) detectors. Uncertainties in the XENON1T data are statistical only and thus too small to be seen. The full black line corresponds to a fit using XENON1T data points with $\frac{a}{\sqrt{E}} + b$, where $a=(31.3\pm 0.7)$ and $b=(0.17\pm 0.02)$ [144]. The purple, blue and green dashed lines represent the expected energy peak of the LL-mode, the KL-mode and the KK-mode of the double electron capture of ^{124}Xe , respectively.

Taking into account all background sources, applying the cuts presented in the last chapter and also adding the signal for the three different decay modes we can obtain the expected energy spectrum represented by the black line in Figure 5.3.

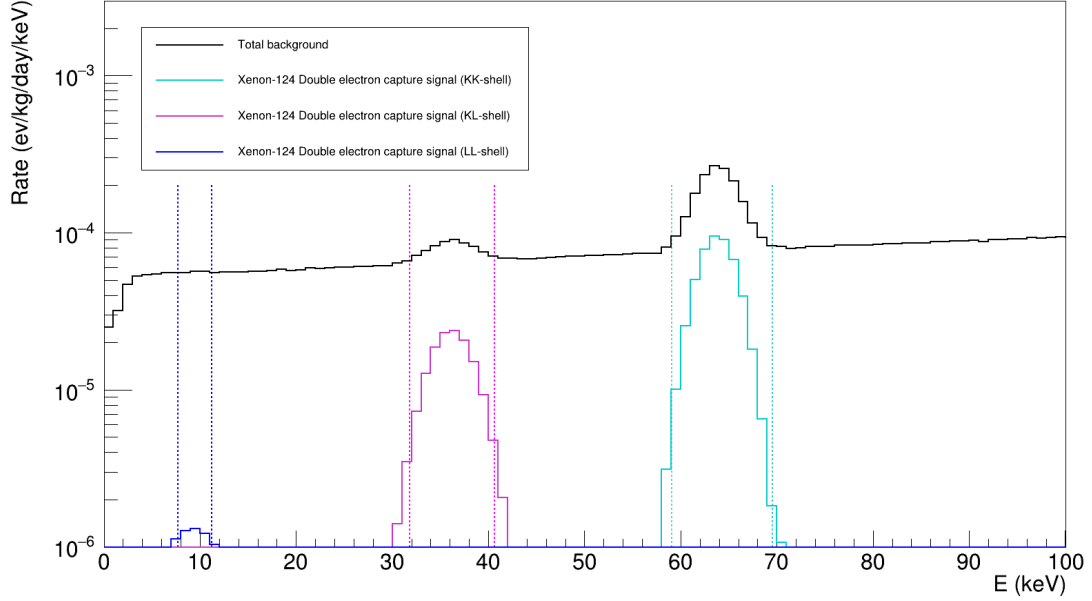


Figure 5.3: Event rate of the expected signals for the LL, KL and KK modes represented by the solid blue, pink and green lines, respectively. The vertical blue, pink and green dashed lines illustrate the 2σ energy windows. The horizontal black solid line represents the total expected spectrum, including all the background sources and the decay modes for the double electron capture of ^{124}Xe .

The expected signals for each decay mode come from Gaussian distributions with the respective deposited energy (mean value) and energy resolution (σ) of each mode. Each signal was scaled assuming half-lives of $T_{1/2}^{2\nu KK} = (1.8 \pm 0.5) \times 10^{22}$ years [106], $T_{1/2}^{2\nu KL} = (6.1 \pm 1.7) \times 10^{22}$ years, $T_{1/2}^{2\nu LL} = (8.2 \pm 2.4) \times 10^{23}$ years for the KK, KL and LL modes, respectively. The LL-mode is presented in blue, the KL-mode in pink, and the KK-mode in green. The respective regions of interest are also represented for each signal, assuming a $\pm 2\sigma$ energy window around the expected signal energy, which corresponds to an efficiency of 95.4%, and they are represented in vertical dashed lines with the associated color of each decay mode.

Table 5.1 shows the expected counts of the main background sources in the respective regions of interest for the LL ([7.81, 11.79] keV), the KL ([32.78, 40.62] keV) and the KK modes ([59.03, 69.57] keV), after application of all the analysis cuts. The expected signal counts of each decay mode in the respective region of interest is also presented. These counts correspond to an exposure time of 1000 days and to 5.6 tonnes of fiducial mass.

Table 5.1: Expected counts in the different regions of interest, for the three different decay modes, of the main background sources. The presented counts corresponds to a 1000 days of exposure of the LZ experiment in the 5.6 tonnes fiducial volume. All the analysis cuts, described in the Section 4.3, have already been applied to the counts of each background source.

Background source	Counts in region of interest (within $\pm 2\sigma$)		
	LL-mode [7.81, 11.79]keV	KL-mode [32.78, 40.62]keV	KK-mode [59.03, 69.57]keV
Detector Components	50	97	117
^{222}Rn	605	1062	1330
^{220}Rn	100	169	201
^{85}Kr	422	750	912
$2\nu 2\beta$ decay of ^{136}Xe	103	777	1744
Solar neutrinos	255	410	437
Total	1535	3267	4743
Expected signal	33	758	2709

In the KK-mode, both electrons are captured from the K-shell with the following atomic de-excitation leading to a total energy deposit of 64.6 keV in X-rays and/or Auger electrons, of which 64.3 keV can be detectable. The region of interest is defined as [59.03, 69.57] keV. This interval is defined assuming a $\pm 2\sigma$ energy window, corresponding to an efficiency of 95.4%, around the expect signal, $E=64.3$ keV. In this energy region, the energy resolution is expected to be around 4.1% [106], as can be seen in Figure 5.2.

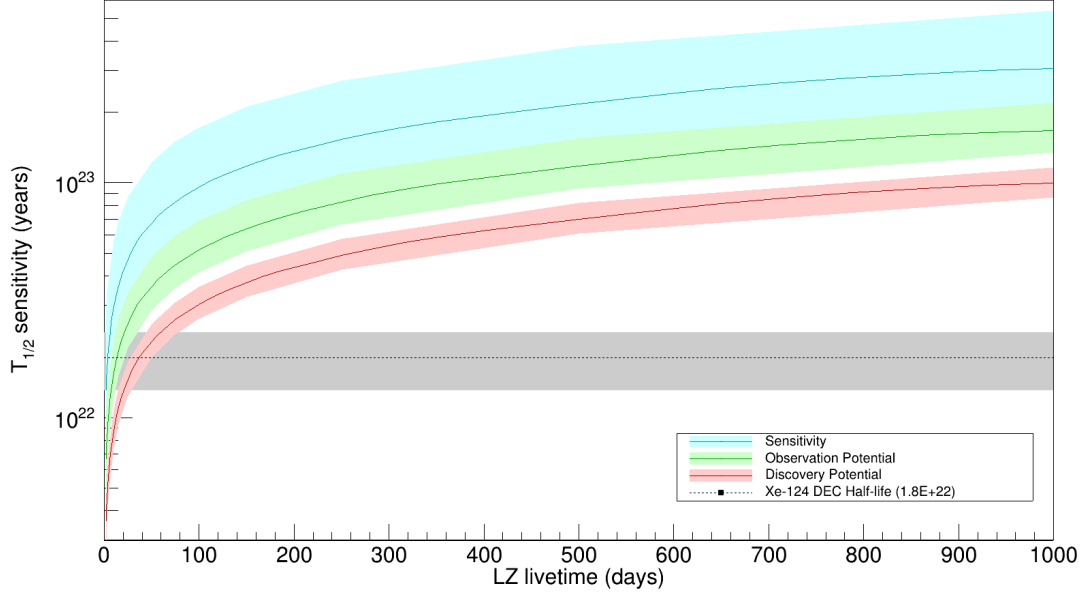


Figure 5.4: The blue, green and red lines represent the evolution of the 90% CL sensitivity, (3σ) observation potential and (5σ) discovery potential, respectively, for the KK-mode over the exposure time of LZ. The blue, green and red bands represent the $\pm 1\sigma$ uncertainty for the sensitivity, observation and discovery potentials, respectively. The half-life for the KK-mode, measured by XENON1T, is represented by the dashed black horizontal line and the respective uncertainty by the grey shaded area.

Figure 5.4 shows the expected evolution of the 90% CL sensitivity, (3σ) observation and (5σ) discovery potentials for the KK-mode in the 5.6 tonnes fiducial volume of LZ with accumulated exposure. The half-life measurement of XENON1T is also shown along with the corresponding error. LZ is expected to be able to reach the observation significance after 13_{+8}^{-6} days of exposure and claim a 5σ discovery after 38_{+22}^{-17} days.

A similar study can be made for the KL and LL-modes. For the KL-mode the expected energy signal is $E=36.7$ keV, with a corresponding region of interest of $[32.78, 40.62]$ keV, assuming an energy resolution of 5.3% which can be extrapolated from the fit in Figure 5.2. For the LL-mode the expected energy signal is $E=9.8$ keV and therefore the region of interest is defined as $[7.81, 11.79]$ keV, taking into account an energy resolution of 10.2%, also extrapolated from the fit in Figure 5.2.

The expected half-life for these decay modes can be determined from that

measured for the KK-mode and the respective branching ratios (see Section 4.1). The respective uncertainty is:

$$\delta T_{1/2}^{2\nu x} = \frac{\delta T_{1/2}^{2\nu 2EC}}{f_x}, \quad (5.2)$$

where $\delta T_{1/2}^{2\nu 2EC} = 0.4 \times 10^{22}$ years [61] and f_x is the branching ratio of each mode. These uncertainties are represented by the gray shaded bands in Figures 5.5 and 5.6.

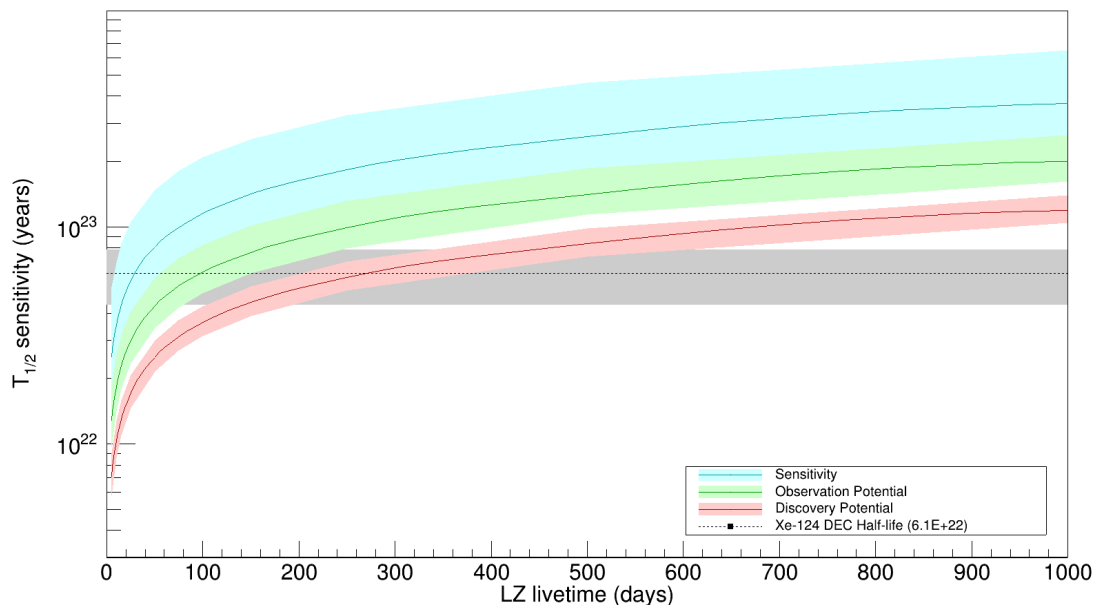


Figure 5.5: The blue, green and red lines represent the evolution of the 90% CL sensitivity, (3σ) observation potential and (5σ) discovery potential, respectively, for the KL-mode over the exposure time of LZ. The blue, green and red bands represent the $\pm 1\sigma$ uncertainty for the sensitivity, observation and discovery potentials, respectively. The expected half-life for the KL-mode, obtained from the XENON1T measurement of the KK-mode [106] with $f_x = 0.23$, is expressed by the dashed black horizontal line and the respective uncertainty, obtained through Equation 5.2, by the gray shaded area.

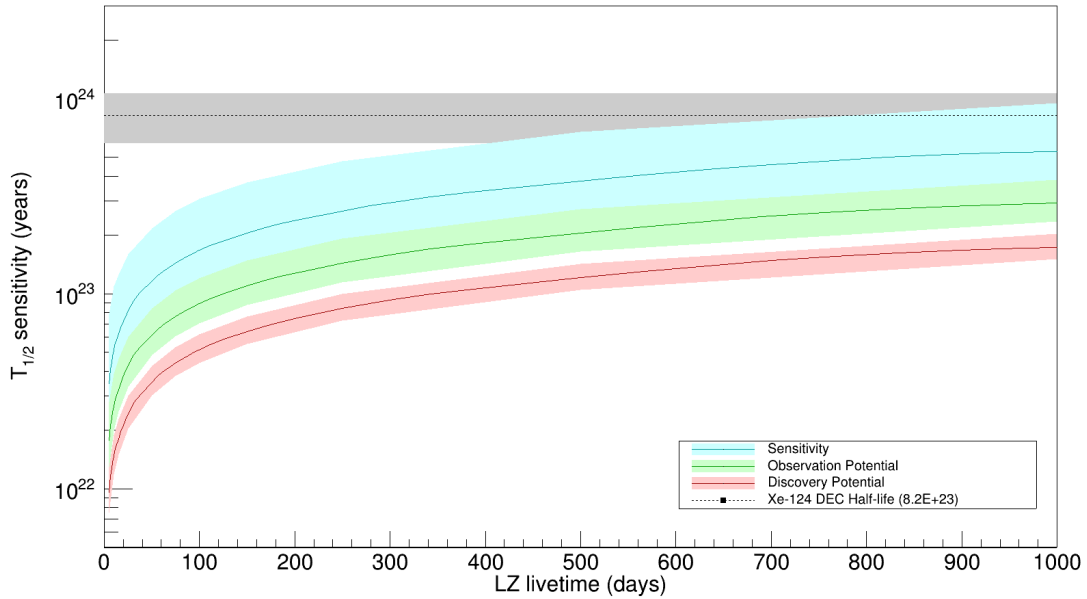


Figure 5.6: The blue, green and red lines represent the evolution of the 90% CL sensitivity, (3σ) observation potential and (5σ) discovery potential, correspondingly, for the LL-mode over the exposure time of LZ. The blue, green and red bands represent the $\pm 1\sigma$ uncertainty for the sensitivity, observation and discovery potentials, respectively. The expected half-life for the LL-mode, obtained from the XENON1T measurement of the KK-mode [106] with $f_x = 0.017$, is expressed by the dashed black horizontal line and the respective uncertainty, obtained through Equation 5.2, by the gray shaded area.

As illustrated in Figure 5.5, LZ is expected to reach the observation significance for the KL-mode after 98_{+61}^{-47} days and claim a 5σ discovery 177_{+270}^{-35} days later, which will become the longest lived nuclear process ever observed directly in a laboratory. On the other hand, as shown in Figure 5.6, LZ will never be able to claim an observation (nor discovery) for this mode with its 1000 days of exposure.

Chapter 6

Conclusions

The work presented in this thesis is focused on the several decay modes of the two neutrino double electron capture of ^{124}Xe . This decay happens when two electrons are simultaneously captured by two protons resulting into two neutrons and the emission of two electron neutrinos. The electrons are predominantly captured from the K and L shells, and thus there are three main decay modes.

In this thesis, we calculated the observed (3σ) and the discovery (5σ) potentials of the LZ experiment for each of those modes. These results were accomplished using simulated data obtained through the GEANT4 toolkit. Firstly, a set of analysis cuts was applied in order to reduce the background events as much as possible, which decreases roughly one order of magnitude in the background rate, and thus making the expected signal more noticeable among all the background. The several analysis cuts applied to the background events were: the definition of the energy region of interest; the single scatter cut; the skin and OD veto cut, and the fiducial volume cut. After these mitigations, the major sources of background come from the double beta decay of ^{136}Xe , the decay of ^{214}Pb in the ^{222}Rn chain and from ^{85}Kr , as can be seen in Figure 4.9 from Section 4.3. One of the main reasons is that both of them can not be removed by the fiducial cut, since they are mixed into the liquid xenon itself.

The XENON1T experiment recently reported the observation of the KK-mode of this decay with a significance of 4.4σ , with a half-life of $T_{1/2} = (1.8 \pm 0.5_{stat} \pm 0.1_{syst}) \times 10^{22}$ years). The number of surviving background events from the cuts

is used to obtain the sensitivity, observation and discovery potentials through the Rolke frequentist method. For the KK-mode, the LZ experiment can reach a 3σ observation after running for 13_{+8}^{-6} days considering the half-life reported by XENON1T, and a 5σ discovery with 38_{+22}^{-17} days of running. For the KL-mode the 3σ observation potential will be reached after 98_{+61}^{-47} days and the 5σ discovery potential after 275_{+172}^{-133} days. Given its much lower probability, it is not expectable that LZ can observe the LL-mode during the 1000 days run, considering the background rate in the energy region of this decay mode.

The LZ experiment will start their first science runs in 2021 and thus have its first results in 2022. There are other detectors with a xenon TPC technology that will also be able to observe this decay, such as: the XENONnT experiment, which operates at the INFN Gran Sasso Laboratory in Italy and will also start its first runs in 2021; the PandaX-4T experiment, which is located at Jinping underground laboratory in Sichuan, China. It is also expected to commence data taking in 2021, and the DARWIN experiment, which is a proposed next-generation multi-tonne dark matter detector, its final location is yet to be decided. The XENONnT and PandaX-4T experiments employ 5.9 and 6 tonnes of total xenon and the DARWIN experiment will operate a 50 tonnes total of liquid xenon.

The study of $2\nu 2EC$ decays can be employed to evaluate the accuracy of the current nuclear models. Namely, it can provide specific inputs to the calculation of nuclear matrix elements of proton-rich isotopes. Furthermore, the $2\nu 2EC$ decay shares the matrix element calculation framework with the exciting $0\nu 2EC$ decay which may provide improvements in the calculations of the unknown nuclear matrix elements of the latter.

The search for neutrinoless decay modes is the hope for finding out whether the neutrino is a Dirac or Majorana particle, even though it was discovered more than a century ago it still remains one of the least understood particles of the SM, and if the total lepton number needs to be conserved.

Over the past few years, the neutrinoless double beta decays of neutron-rich isotopes ($0\nu 2\beta^-$) have been much sought after since there are a large natural abundance of them. At the same time, the proton-rich isotopes can be very interesting as well due to its singular decay topology. Those with a Q-value higher than 2044 MeV are the ones that provide a wider search. Since they can decay through three different modes ($2\beta^+, \beta^+ EC, 2EC$) where each one has a distinct

decay topology.

Furthermore, the $0\nu 2EC$, which is expected to have a significantly higher half-life than that of the $0\nu 2\beta^-$, can have its half-life reduced by a factor of 10^6 if the decay obeys to a resonance condition, $R0\nu 2EC$. The possibility of a resonant enhancement of the $0\nu 2EC$ decay, $R0\nu 2EC$, happens when the initial and final (excited) states are energetically degenerate.

The $R0\nu 2EC$ experimental signature is a coincidence de-excitation of the atomic shell and the nucleus. The signal consists in several X-rays and/or Auger electrons which occurs when the vacancies of the captured electrons are filled and one or more gamma-rays from the de-excitation of the nucleus. Thanks to such a unique signature it may be possible to discriminate much more efficiently the background from the expected signal.

References

- [1] David Tong. “Line operators in the Standard Model”. In: *Journal of High Energy Physics* 2017.7 (2017). ISSN: 1029-8479. DOI: 10.1007/jhep07(2017)104. URL: [http://dx.doi.org/10.1007/JHEP07\(2017\)104](http://dx.doi.org/10.1007/JHEP07(2017)104).
- [2] Antonio Pich. *The Standard Model of Electroweak Interactions*. 2012. arXiv: 1201.0537 [hep-ph].
- [3] W. Pauli. “The Connection Between Spin and Statistics”. In: *Phys. Rev.* 58 (8 1940), pp. 716–722. DOI: 10.1103/PhysRev.58.716. URL: <https://link.aps.org/doi/10.1103/PhysRev.58.716>.
- [4] James D. Wells. *The Once and Present Standard Model of Elementary Particle Physics*. 2019. arXiv: 1911.04604 [physics.hist-ph].
- [5] Gregg Jaeger. “Exchange Forces in Particle Physics”. en. In: *Foundations of Physics* 51.1 (2021), p. 13. ISSN: 1572-9516. DOI: 10.1007/s10701-021-00425-0. URL: <https://doi.org/10.1007/s10701-021-00425-0> (visited on 05/31/2021).
- [6] V. A. Bednyakov, N. D. Giokaris, and A. V. Bednyakov. “On the Higgs mass generation mechanism in the Standard Model”. In: *Physics of Particles and Nuclei* 39.1 (2008), pp. 13–36. ISSN: 1531-8559. DOI: 10.1134/S1063779608010024. URL: <http://dx.doi.org/10.1134/S1063779608010024>.
- [7] Michael E. Peskin. *Lectures on the Theory of the Weak Interaction*. 2017. arXiv: 1708.09043 [hep-ph].
- [8] André de Gouvêa and Petr Vogel. “Lepton flavor and number conservation, and physics beyond the standard model”. In: *Progress in Particle and Nuclear Physics* 71 (2013). ISSN: 0146-6410. DOI: 10.1016/j.ppnp.2013.03.006. URL: <http://dx.doi.org/10.1016/j.ppnp.2013.03.006>.

- [9] Ferruccio Feruglio and Andrea Romanino. *Lepton Flavour Symmetries*. 2021. arXiv: 1912.06028 [hep-ph].
- [10] Nobelprize.org. *The Nobel Prize in Physics 2015*. Accessed: 2021-07-15. URL: <https://www.nobelprize.org/prizes/physics/2015/summary/>.
- [11] André de Gouvêa and Petr Vogel. “Lepton flavor and number conservation, and physics beyond the standard model”. In: *Progress in Particle and Nuclear Physics* 71 (2013), pp. 75–92. ISSN: 0146-6410. DOI: 10.1016/j.pnnp.2013.03.006. URL: <http://dx.doi.org/10.1016/j.pnnp.2013.03.006>.
- [12] ERNESTO A. MATUTE. “A TOPOLOGICAL VIEW ON BARYON NUMBER CONSERVATION”. In: *Modern Physics Letters A* 19 (19 2004), pp. 1469–1482. ISSN: 0217-7323. DOI: 10.1142/S0217732304013738. URL: <http://doi.org/10.1142/S0217732304013738>.
- [13] Adam Koberinski. “Parity violation in weak interactions: How experiment can shape a theoretical framework”. In: *Studies in History and Philosophy of Science Part B: Studies in History and Philosophy of Modern Physics* 67 (2019), pp. 64–77. ISSN: 1355-2198. DOI: <https://doi.org/10.1016/j.shpsb.2019.05.001>. URL: <https://www.sciencedirect.com/science/article/pii/S1355219818301047>.
- [14] G. Rajasekaran. “Fermi and the theory of weak interactions”. In: *Resonance* 19.1 (2014), pp. 18–44. ISSN: 0973-712X. DOI: 10.1007/s12045-014-0005-2. URL: <http://dx.doi.org/10.1007/s12045-014-0005-2>.
- [15] C. N. Lee T. D.; Yang. “Parity Nonconservation and a Two-Component Theory of the Neutrino”. In: *Physical Review (Series I)* 105 (5 1957), pp. 1671–1675. ISSN: 0031-899X,1536-6065. DOI: 10.1103/physrev.105.1671. URL: <http://doi.org/10.1103/physrev.105.1671>.
- [16] C.; Ambler; Hayward; Hoppe; Hudson Wu. “Experimental Test of Parity Conservation in Beta Decay”. In: *Physical Review (Series I)* 105 (4 1957), pp. 1413–1415. ISSN: 0031-899X,1536-6065. DOI: 10.1103/PhysRev.105.1413. URL: <http://doi.org/10.1103/PhysRev.105.1413>.

- [17] C.Y. Prescott et al. “Parity non-conservation in inelastic electron scattering”. In: *Physics Letters B* 77.3 (1978), pp. 347–352. ISSN: 0370-2693. DOI: [https://doi.org/10.1016/0370-2693\(78\)90722-0](https://doi.org/10.1016/0370-2693(78)90722-0). URL: <https://www.sciencedirect.com/science/article/pii/0370269378907220>.
- [18] M. Strikhanov. “Problems of the standard model and the status of the accelerator experiment”. In: *Herald of the Russian Academy of Sciences* 82 (2012). DOI: 10.1134/S1019331612030033. URL: <http://doi.org/10.1134/s1019331612030033>.
- [19] *NASA Science Universe Dark Energy, Dark Matter*. Accessed: 2021-06-05. URL: <https://science.nasa.gov/astrophysics/focus-areas/what-is-dark-energy>.
- [20] J. Ellis. “Outstanding questions: physics beyond the Standard Model”. In: *Philosophical Transactions Mathematical Physical Engineering Sciences* 370 (1961 2012), pp. 818–830. ISSN: 1364-503X,1471-2962. DOI: 10.1098/rsta.2011.0452. URL: <http://doi.org/10.1098/rsta.2011.0452>.
- [21] *Pauli’s letter of the 4th of December 1930*. Accessed: 2021-06-12. URL: <http://www.pp.rhul.ac.uk/~ptd/TEACHING/PH2510/pauli-letter.html>.
- [22] “Pauli’s Proof of the Spin-Statistics Theorem”. In: *Pauli and the Spin-Statistics Theorem*. WORLD SCIENTIFIC, Mar. 1998, pp. 345–367. DOI: 10.1142/9789812817037_0015. URL: https://doi.org/10.1142%5C%2F9789812817037_0015.
- [23] I. G. Kaplan. *Pauli Exclusion Principle and its theoretical foundation*. 2019. arXiv: 1902.00499 [quant-ph].
- [24] C. L. Cowan et al. “Detection of the Free Neutrino: a Confirmation”. In: *Science* 124.3212 (1956), pp. 103–104. ISSN: 0036-8075. DOI: 10.1126/science.124.3212.103. eprint: <https://science.sciencemag.org/content/124/3212/103.full.pdf>. URL: <https://science.sciencemag.org/content/124/3212/103>.
- [25] Nobelprize.org. *The Nobel Prize in Physics 1988*. Accessed: 2021-06-23. URL: <https://www.nobelprize.org/prizes/physics/1988/press-release/>.

- [26] K. Kodama et al. “Observation of tau neutrino interactions”. In: *Physics Letters B* 504.3 (Apr. 2001), pp. 218–224. ISSN: 0370-2693. DOI: 10.1016/S0370-2693(01)00307-0. URL: [http://dx.doi.org/10.1016/S0370-2693\(01\)00307-0](http://dx.doi.org/10.1016/S0370-2693(01)00307-0).
- [27] J. N. Bahcall and M. H. Pinsonneault. “Standard solar models, with and without helium diffusion, and the solar neutrino problem”. In: *Rev. Mod. Phys.* 64 (4 1992), pp. 885–926. DOI: 10.1103/RevModPhys.64.885. URL: <https://link.aps.org/doi/10.1103/RevModPhys.64.885>.
- [28] John N. Bahcall. “Solar Neutrinos. I. Theoretical”. In: *Phys. Rev. Lett.* 12 (11 1964), pp. 300–302. DOI: 10.1103/PhysRevLett.12.300. URL: <https://link.aps.org/doi/10.1103/PhysRevLett.12.300>.
- [29] V. Castellani et al. “Solar neutrinos: beyond standard solar models”. In: *Physics Reports* 281.5-6 (1997), pp. 309–398. ISSN: 0370-1573. DOI: 10.1016/S0370-1573(96)00032-4. URL: [http://dx.doi.org/10.1016/S0370-1573\(96\)00032-4](http://dx.doi.org/10.1016/S0370-1573(96)00032-4).
- [30] M. Honda et al. “Atmospheric neutrino flux calculation using the NRLMSISE-00 atmospheric model”. In: *Phys. Rev. D* 92 (2 2015), p. 023004. DOI: 10.1103/PhysRevD.92.023004. URL: <https://link.aps.org/doi/10.1103/PhysRevD.92.023004>.
- [31] Hans-Thomas Janka. “Neutrino Emission from Supernovae”. In: *Handbook of Supernovae* (2017), pp. 1575–1604. DOI: 10.1007/978-3-319-21846-5_4. URL: http://dx.doi.org/10.1007/978-3-319-21846-5_4.
- [32] Evgeny Akhmedov. “Relic neutrino detection through angular correlations in inverse β -decay”. In: *Journal of Cosmology and Astroparticle Physics* 2019.09 (2019), pp. 031–031. ISSN: 1475-7516. DOI: 10.1088/1475-7516/2019/09/031. URL: <http://dx.doi.org/10.1088/1475-7516/2019/09/031>.
- [33] Chiaki Yanagisawa. “Looking for cosmic neutrino background”. In: *Frontiers in Physics* 2 (2014). ISSN: 2296-424X. DOI: 10.3389/fphy.2014.00030. URL: <http://doi.org/10.3389/fphy.2014.00030>.

- [34] R. Aloisio et al. “Cosmogenic neutrinos and ultra-high energy cosmic ray models”. In: *Journal of Cosmology and Astroparticle Physics* 2015.10 (2015), pp. 006–006. ISSN: 1475-7516. DOI: 10.1088/1475-7516/2015/10/006. URL: <http://dx.doi.org/10.1088/1475-7516/2015/10/006>.
- [35] G. Bellini et al. “Geo-neutrinos”. In: *Progress in Particle and Nuclear Physics* 73 (2013), pp. 1–34. ISSN: 0146-6410. DOI: 10.1016/j.pnpnp.2013.07.001. URL: <http://dx.doi.org/10.1016/j.pnpnp.2013.07.001>.
- [36] Y. Declais et al. “Study of reactor antineutrino interaction with proton at Bugey nuclear power plant”. In: *Physics Letters B* 338.2 (1994), pp. 383–389. ISSN: 0370-2693. DOI: [https://doi.org/10.1016/0370-2693\(94\)91394-3](https://doi.org/10.1016/0370-2693(94)91394-3). URL: <https://www.sciencedirect.com/science/article/pii/S0370269394913943>.
- [37] S KOPP. “Accelerator neutrino beams”. In: *Physics Reports* 439.3 (2007), pp. 101–159. ISSN: 0370-1573. DOI: 10.1016/j.physrep.2006.11.004. URL: <http://dx.doi.org/10.1016/j.physrep.2006.11.004>.
- [38] U.F. Katz and Ch. Spiering. “High-energy neutrino astrophysics: Status and perspectives”. In: *Progress in Particle and Nuclear Physics* 67.3 (2012), pp. 651–704. ISSN: 0146-6410. DOI: 10.1016/j.pnpnp.2011.12.001. URL: <http://dx.doi.org/10.1016/j.pnpnp.2011.12.001>.
- [39] Stephen F King and Christoph Luhn. “Neutrino mass and mixing with discrete symmetry”. In: *Reports on Progress in Physics* 76.5 (2013), p. 056201. ISSN: 1361-6633. DOI: 10.1088/0034-4885/76/5/056201. URL: <http://dx.doi.org/10.1088/0034-4885/76/5/056201>.
- [40] Ziro Maki, Masami Nakagawa, and Shoichi Sakata. “Remarks on the Unified Model of Elementary Particles”. In: *Progress of Theoretical Physics* 28.5 (1962), pp. 870–880. ISSN: 0033-068X. DOI: 10.1143/PTP.28.870. eprint: <https://academic.oup.com/ptp/article-pdf/28/5/870/5258750/28-5-870.pdf>. URL: <https://doi.org/10.1143/PTP.28.870>.
- [41] Giganti; Lavignac; Zito. “Neutrino oscillations: The rise of the PMNS paradigm”. In: *Progress in Particle and Nuclear Physics* (2018), S014664101730087X. ISSN: 0146-6410. DOI: 10.1016/j.pnpnp.2017.10.001. URL: <http://doi.org/10.1016/j.pnpnp.2017.10.001>.

- [42] Ivan Esteban et al. “The fate of hints: updated global analysis of three-flavor neutrino oscillations”. In: *Journal of High Energy Physics* 2020.9 (2020). ISSN: 1029-8479. DOI: 10.1007/jhep09(2020)178. URL: [http://dx.doi.org/10.1007/JHEP09\(2020\)178](http://dx.doi.org/10.1007/JHEP09(2020)178).
- [43] A. Upadhyay and M. Batra. “Phenomenology of Neutrino Mixing in Vacuum and Matter”. In: *ISRN High Energy Physics* 2013 (2013), pp. 1–15. ISSN: 2090-7427. DOI: 10.1155/2013/206516. URL: <http://dx.doi.org/10.1155/2013/206516>.
- [44] Sunny Vagnozzi. “Weigh them all! - Cosmological searches for the neutrino mass scale and mass ordering”. PhD thesis. 2019.
- [45] Shiva King. “Measurement of the Double Beta Decay Half-Life of ^{100}Mo to the 0_1^+ Excited State, and ^{48}Ca to the Ground State in the NEMO3 Experiment”. PhD thesis. U. Coll. London, 2008.
- [46] *Feynman diagram maker*. <https://www.aidansean.com/feynman/>. Accessed: 2020-09-09.
- [47] Padraic Seamus Finnerty. “A Direct Dark Matter Search with the MAJORANA Low-Background Broad Energy Germanium Detector”. PhD thesis. North Carolina U., 2013. DOI: 10.17615/hj0v-8263.
- [48] *University of Zurich - GERmanium Detector Array (GERDA)*. <https://www.physik.uzh.ch/en/groups/audis/Research/GERDA.html>. Accessed: 2021-10-01.
- [49] J. Bernabeu, A. De Rujula, and C. Jarlskog. “Neutrinoless double electron capture as a tool to measure the electron neutrino mass”. In: *Nuclear Physics B* 223.1 (1983), pp. 15–28. ISSN: 0550-3213. DOI: [https://doi.org/10.1016/0550-3213\(83\)90089-5](https://doi.org/10.1016/0550-3213(83)90089-5). URL: <https://www.sciencedirect.com/science/article/pii/0550321383900895>.
- [50] S. Sujkowski Z.; Wycech. “Neutrinoless double electron capture: A tool to search for Majorana neutrinos”. In: *Physical Review C* 70 (5 2004), p. 052501. ISSN: 0556-2813,1089-490X. DOI: 10.1103/PhysRevC.70.052501. URL: <http://doi.org/10.1103/PhysRevC.70.052501>.

- [51] J.D. Vergados. “Lepton-violating $\beta^-\beta^-$, $\beta^+\beta^+$ decays, (e^- , e^+) conversion and double electron capture in gauge theories”. In: *Nuclear Physics B* 218.1 (1983), pp. 109–144. ISSN: 0550-3213. DOI: [https://doi.org/10.1016/0550-3213\(83\)90477-7](https://doi.org/10.1016/0550-3213(83)90477-7). URL: <https://www.sciencedirect.com/science/article/pii/0550321383904777>.
- [52] Tsuneyuki Doi Masaru; Kotani. “Neutrinoless Modes of Double Beta Decay”. In: *Progress of Theoretical Physics* 89 (1 1993), pp. 139–159. ISSN: 0033-068X,1347-4081. DOI: 10.1143/ptp.89.139. URL: <http://doi.org/10.1143/ptp.89.139>.
- [53] Jouni Suhonen et al. “Interplay of particle, nuclear and atomic physics in rare weak decays”. In: AIP, 2010. DOI: 10.1063/1.3527257. URL: <https://doi.org/10.1063/1.3527257>.
- [54] K. Blaum et al. *Neutrinoless Double-Electron Capture*. 2020.
- [55] A.S. Barabash et al. “Search for β^+ EC and ECEC processes in ^{74}Se ”. In: *Nuclear Physics A* 785.3 (2007), pp. 371–380. ISSN: 0375-9474. DOI: <https://doi.org/10.1016/j.nuclphysa.2007.01.002>. URL: <https://www.sciencedirect.com/science/article/pii/S0375947407000310>.
- [56] A.S. Barabash et al. “Search for β^+ EC and ECEC processes in ^{112}Sn and $\beta^-\beta^-$ decay of ^{124}Sn to the excited states of ^{124}Te ”. In: *Nuclear Physics A* 807.3 (2008), pp. 269–281. ISSN: 0375-9474. DOI: <https://doi.org/10.1016/j.nuclphysa.2008.04.009>. URL: <https://www.sciencedirect.com/science/article/pii/S0375947408005277>.
- [57] J. Dawson et al. “Search for double- β decays of tin isotopes with enhanced sensitivity”. In: *Physical Review C* 78.3 (2008). ISSN: 1089-490X. DOI: 10.1103/physrevc.78.035503. URL: <http://dx.doi.org/10.1103/PhysRevC.78.035503>.
- [58] M. F. Kidd, J. H. Esterline, and W. Tornow. “Double-electron capture on ^{112}Sn to the excited 1871 keV state in ^{112}Cd : A possible alternative to double- β decay”. In: *Phys. Rev. C* 78 (3 Sept. 2008), p. 035504. DOI: 10.1103/PhysRevC.78.035504. URL: <https://link.aps.org/doi/10.1103/PhysRevC.78.035504>.

- [59] K. L. Green et al. “Degeneracy at 1871 keV in ^{112}Cd and implications for neutrinoless double electron capture”. In: *Phys. Rev. C* 80 (3 2009), p. 032502. DOI: 10.1103/PhysRevC.80.032502. URL: <https://link.aps.org/doi/10.1103/PhysRevC.80.032502>.
- [60] L. Lukaszuk; Z. Sujkowski; S. Wycech. “Searching for Majorana neutrinos with double beta decay and with beta beams”. In: *The European Physical Journal A / Hadrons and Nuclei* 27 (1 Supplement 2006), pp. 63–66. ISSN: 1434-6001,1434-601X. DOI: 10.1140/epja/i2006-08-008-7. URL: <https://doi.org/10.1140/epja/i2006-08-008-7>.
- [61] Christian Wittweg et al. “Detection prospects for the second-order weak decays of ^{124}Xe in multi-tonne xenon time projection chambers”. In: *The European Physical Journal C* 80.12 (2020). ISSN: 1434-6052. DOI: 10.1140/epjc/s10052-020-08726-w. URL: <http://dx.doi.org/10.1140/epjc/s10052-020-08726-w>.
- [62] Masaru Doi and Tsuneyuki Kotani. “Neutrino Emitting Modes of Double Beta Decay”. In: *Progress of Theoretical Physics* 87.5 (1992), pp. 1207–1231. ISSN: 0033-068X. DOI: 10.1143/ptp/87.5.1207. eprint: <https://academic.oup.com/ptp/article-pdf/87/5/1207/5272207/87-5-1207.pdf>. URL: <https://doi.org/10.1143/ptp/87.5.1207>.
- [63] J. Barea, J. Kotila, and F. Iachello. “Neutrinoless double-positron decay and positron-emitting electron capture in the interacting boson model”. In: *Phys. Rev. C* 87 (5 2013), p. 057301. DOI: 10.1103/PhysRevC.87.057301. URL: <https://link.aps.org/doi/10.1103/PhysRevC.87.057301>.
- [64] Mihail Stoica Sabin; Mirea. “Phase Space Factors for Double-Beta Decays”. In: *Frontiers in Physics* 7 (2019), p. 12. ISSN: 2296-424X. DOI: 10.3389/fphy.2019.00012. URL: <http://doi.org/10.3389/fphy.2019.00012>.
- [65] Jouni Suhonen. “Double beta decays of ^{124}Xe investigated in the QRPA framework”. In: *Journal of Physics G Nuclear and Particle Physics* 40 (7 2013), p. 075102. ISSN: 0954-3899,1361-6471. DOI: 10.1088/0954-3899/40/7/075102.

- [66] Pekka Pirinen and Jouni Suhonen. “Systematic approach to β and $2\nu\beta\beta$ decays of mass $A = 100 - 136$ nuclei”. In: *Phys. Rev. C* 91 (5 2015), p. 054309. DOI: 10.1103/PhysRevC.91.054309. URL: <https://link.aps.org/doi/10.1103/PhysRevC.91.054309>.
- [67] Sabin Stoica and Mihail Mirea. “Phase Space Factors for Double-Beta Decays”. In: *Frontiers in Physics* 7 (2019), p. 12. ISSN: 2296-424X. DOI: 10.3389/fphy.2019.00012. URL: <https://www.frontiersin.org/article/10.3389/fphy.2019.00012>.
- [68] J. Kotila, J. Barea, and F. Iachello. “Neutrinoless double-electron capture”. In: *Phys. Rev. C* 89 (6 2014), p. 064319. DOI: 10.1103/PhysRevC.89.064319. URL: <https://link.aps.org/doi/10.1103/PhysRevC.89.064319>.
- [69] M.I. Krivoruchenko et al. “Resonance enhancement of neutrinoless double electron capture”. In: *Nuclear Physics A* 859.1 (2011), pp. 140–171. ISSN: 0375-9474. DOI: <https://doi.org/10.1016/j.nuclphysa.2011.04.009>. URL: <https://www.sciencedirect.com/science/article/pii/S0375947411002855>.
- [70] K. Blaum et al. “Neutrinoless double-electron capture”. In: *Rev. Mod. Phys.* 92 (4 2020), p. 045007. DOI: 10.1103/RevModPhys.92.045007. URL: <https://link.aps.org/doi/10.1103/RevModPhys.92.045007>.
- [71] D. S. Akerib et al. “Results from a Search for Dark Matter in the Complete LUX Exposure”. In: *Physical Review Letters* 118.2 (2017). ISSN: 1079-7114. DOI: 10.1103/physrevlett.118.021303. URL: <http://dx.doi.org/10.1103/PhysRevLett.118.021303>.
- [72] D.Yu. Akimov et al. “WIMP-nucleon cross-section results from the second science run of ZEPLIN-III”. In: *Physics Letters B* 709.1-2 (2012), pp. 14–20. ISSN: 0370-2693. DOI: 10.1016/j.physletb.2012.01.064. URL: <http://dx.doi.org/10.1016/j.physletb.2012.01.064>.
- [73] Kenneth Lande. “Raymond Davis, Jr. (19142006)”. In: *Bulletin of the AAS* 49.1 (Dec. 1, 2017). <https://baas.aas.org/pub/raymond-davis-jr-1914-2006>. URL: <https://baas.aas.org/pub/raymond-davis-jr-1914-2006>.

- [74] Nobelprize.org. *The Nobel Prize in Physics 2002*. Accessed: 2021-07-01. URL: <https://www.nobelprize.org/prizes/physics/2002/davis/facts/>.
- [75] D. S. Akerib et al. “Search for annual and diurnal rate modulations in the LUX experiment”. In: *Phys. Rev. D* 98 (6 2018), p. 062005. DOI: 10.1103/PhysRevD.98.062005. URL: <https://link.aps.org/doi/10.1103/PhysRevD.98.062005>.
- [76] *SLAC NATIONAL ACCELERATOR LABORATORY - Prototype of LUX-ZEPLIN Dark Matter Detector Tested at SLAC*. <https://www6.slac.stanford.edu/news/2016-06-01-prototype-lux-zeplin-dark-matter-detector-tested-slac.aspx>. Accessed: 2021-10-01.
- [77] The LZ Collaboration et al. *LUX-ZEPLIN (LZ) Conceptual Design Report*. 2015. arXiv: 1509.02910 [physics.ins-det].
- [78] B. J. Mount et al. *LUX-ZEPLIN (LZ) Technical Design Report*. 2017. arXiv: 1703.09144 [physics.ins-det].
- [79] D.S. Akerib et al. “Identification of radiopure titanium for the LZ dark matter experiment and future rare event searches”. In: *Astroparticle Physics* 96 (2017), pp. 1–10. ISSN: 0927-6505. DOI: 10.1016/j.astropartphys.2017.09.002. URL: <http://dx.doi.org/10.1016/j.astropartphys.2017.09.002>.
- [80] *SLAC NATIONAL ACCELERATOR LABORATORY - SLAC sends off woven grids for LUX-ZEPLIN dark matter detector*. <https://www6.slac.stanford.edu/news/2019-06-20-slac-sends-woven-grids-lux-zeplin-dark-matter-detector.aspx>. Accessed: 2021-10-01.
- [81] Wanda Beriguete et al. “Production of a gadolinium-loaded liquid scintillator for the Daya Bay reactor neutrino experiment”. In: *Nuclear Instruments and Methods in Physics Research Section A: Accelerators, Spectrometers, Detectors and Associated Equipment* 763 (2014), pp. 82–88. ISSN: 0168-9002. DOI: 10.1016/j.nima.2014.05.119. URL: <http://dx.doi.org/10.1016/j.nima.2014.05.119>.
- [82] W. Turner et al. *Optical Calibration System for the LUX-ZEPLIN (LZ) Outer Detector*. 2021. arXiv: 2102.06281 [physics.ins-det].

- [83] M. Mastromarco et al. “Cross section measurements of $^{155,157}\text{Gd}(n,\gamma)$ induced by thermal and epithermal neutrons”. In: *The European Physical Journal A* 55.1 (2019). ISSN: 1434-601X. DOI: 10.1140/epja/i2019-12692-7. URL: <http://dx.doi.org/10.1140/epja/i2019-12692-7>.
- [84] Tomoyuki Tanaka et al. *Gamma Ray Spectra from Thermal Neutron Capture on Gadolinium-155 and Natural Gadolinium*. arXiv: 1907.00788.
- [85] E. Aprile and T. Doke. “Liquid xenon detectors for particle physics and astrophysics”. In: *Reviews of Modern Physics* 82.3 (2010), pp. 2053–2097. ISSN: 1539-0756. DOI: 10.1103/revmodphys.82.2053. URL: <http://dx.doi.org/10.1103/RevModPhys.82.2053>.
- [86] Keiko Fujii et al. “High-accuracy measurement of the emission spectrum of liquid xenon in the vacuum ultraviolet region”. In: *Nuclear Instruments and Methods in Physics Research Section A: Accelerators, Spectrometers, Detectors and Associated Equipment* 795 (2015), pp. 293–297. ISSN: 0168-9002. DOI: <https://doi.org/10.1016/j.nima.2015.05.065>. URL: <https://www.sciencedirect.com/science/article/pii/S016890021500724X>.
- [87] D. S. Akerib et al. “Liquid xenon scintillation measurements and pulse shape discrimination in the LUX dark matter detector”. In: *Physical Review D* 97.11 (2018). ISSN: 2470-0029. DOI: 10.1103/physrevd.97.112002. URL: <http://dx.doi.org/10.1103/PhysRevD.97.112002>.
- [88] Carl Eric Dahl. “The physics of background discrimination in liquid xenon, and first results from Xenon10 in the hunt for WIMP dark matter”. PhD thesis. Princeton U., 2009.
- [89] D. S. Akerib et al. “Calibration, event reconstruction, data analysis, and limit calculation for the LUX dark matter experiment”. In: *Physical Review D* 97.10 (2018). ISSN: 2470-0029. DOI: 10.1103/physrevd.97.102008. URL: <http://dx.doi.org/10.1103/PhysRevD.97.102008>.
- [90] J Lindhard et al. “INTEGRAL EQUATIONS GOVERNING RADIATION EFFECTS. (NOTES ON ATOMIC COLLISIONS, III)”. In: *Kgl. Danske Videnskab., Selskab. Mat. Fys. Medd.* Vol: 33: No. 10 (1963). URL: <https://www.osti.gov/biblio/4701226>.

- [91] J.D. Lewin and P.F. Smith. “Review of mathematics, numerical factors, and corrections for dark matter experiments based on elastic nuclear recoil”. In: *Astroparticle Physics* 6.1 (1996), pp. 87–112. ISSN: 0927-6505. DOI: [https://doi.org/10.1016/S0927-6505\(96\)00047-3](https://doi.org/10.1016/S0927-6505(96)00047-3). URL: <https://www.sciencedirect.com/science/article/pii/S0927650596000473>.
- [92] Juris Meija et al. “Atomic weights of the elements 2013 (IUPAC Technical Report)”. In: *Pure and Applied Chemistry* 88.3 (2016). DOI: [doi:10.1515/pac-2015-0305](https://doi.org/10.1515/pac-2015-0305). URL: <https://doi.org/10.1515/pac-2015-0305>.
- [93] D.S. Akerib et al. “Simulations of events for the LUX-ZEPLIN (LZ) dark matter experiment”. In: *Astroparticle Physics* 125 (2021), p. 102480. ISSN: 0927-6505. DOI: [10.1016/j.astropartphys.2020.102480](https://doi.org/10.1016/j.astropartphys.2020.102480). URL: <http://dx.doi.org/10.1016/j.astropartphys.2020.102480>.
- [94] M.-M. Bé et al. *Table of Radionuclides*. Pavillon de Breteuil, F-92310 Sèvres, France: Bureau International des Poids et Mesures. URL: http://www.nucleide.org/DDEP_WG/Nuclides/H-3_tables.pdf.
- [95] D. S. Akerib et al. “Tritium calibration of the LUX dark matter experiment”. In: *Physical Review D* 93.7 (2016). ISSN: 2470-0029. DOI: [10.1103/PhysRevD.93.072009](https://doi.org/10.1103/PhysRevD.93.072009). URL: <http://dx.doi.org/10.1103/PhysRevD.93.072009>.
- [96] M Szydagis et al. “NEST: a comprehensive model for scintillation yield in liquid xenon”. In: *Journal of Instrumentation* 6.10 (2011), P10002–P10002. ISSN: 1748-0221. DOI: [10.1088/1748-0221/6/10/p10002](https://doi.org/10.1088/1748-0221/6/10/p10002). URL: <http://dx.doi.org/10.1088/1748-0221/6/10/P10002>.
- [97] D.S. Akerib et al. “LUXSim: A component-centric approach to low-background simulations”. In: *Nuclear Instruments and Methods in Physics Research Section A: Accelerators, Spectrometers, Detectors and Associated Equipment* 675 (2012), pp. 63–77. ISSN: 0168-9002. DOI: <https://doi.org/10.1016/j.nima.2012.02.010>. URL: <https://www.sciencedirect.com/science/article/pii/S0168900212001532>.
- [98] S. Agostinelli et al. “GEANT4—a simulation toolkit”. In: *Nucl. Instrum. Meth. A* 506 (2003), pp. 250–303. DOI: [10.1016/S0168-9002\(03\)01368-8](https://doi.org/10.1016/S0168-9002(03)01368-8).

- [99] M Szydagi et al. “Enhancement of NEST capabilities for simulating low-energy recoils in liquid xenon”. In: *Journal of Instrumentation* 8.10 (2013), pp. C10003–C10003. ISSN: 1748-0221. DOI: 10.1088/1748-0221/8/10/c10003. URL: <http://dx.doi.org/10.1088/1748-0221/8/10/C10003>.
- [100] *QuickField*. <https://quickfield.com/>. Accessed: 2021-04-08.
- [101] S.J. Haselschwardt et al. “A liquid scintillation detector for radioassay of gadolinium-loaded liquid scintillator for the LZ Outer Detector”. In: *Nuclear Instruments and Methods in Physics Research Section A: Accelerators, Spectrometers, Detectors and Associated Equipment* 937 (2019), pp. 148–163. ISSN: 0168-9002. DOI: 10.1016/j.nima.2019.05.055. URL: <http://dx.doi.org/10.1016/j.nima.2019.05.055>.
- [102] Bradley S. Meyer. “The r-, s-, and p-Processes in Nucleosynthesis”. In: *Annual Review of Astronomy and Astrophysics* 32.1 (1994), pp. 153–190. DOI: 10.1146/annurev.aa.32.090194.001101. eprint: <https://doi.org/10.1146/annurev.aa.32.090194.001101>. URL: <https://doi.org/10.1146/annurev.aa.32.090194.001101>.
- [103] Yu. M. Gavriilyuk et al. “Indications of $2\nu 2K$ capture in ^{78}Kr ”. In: *Phys. Rev. C* 87 (3 2013), p. 035501. DOI: 10.1103/PhysRevC.87.035501. URL: <https://link.aps.org/doi/10.1103/PhysRevC.87.035501>.
- [104] A. P. Meshik et al. “Weak decay of ^{130}Ba and ^{132}Ba : Geochemical measurements”. In: *Phys. Rev. C* 64 (3 2001), p. 035205. DOI: 10.1103/PhysRevC.64.035205. URL: <https://link.aps.org/doi/10.1103/PhysRevC.64.035205>.
- [105] Magali Pujol et al. “Xenon in Archean barite: Weak decay of ^{130}Ba , mass-dependent isotopic fractionation and implication for barite formation”. In: *Geochimica et Cosmochimica Acta* 73.22 (2009), pp. 6834–6846. ISSN: 0016-7037. DOI: <https://doi.org/10.1016/j.gca.2009.08.002>. URL: <https://www.sciencedirect.com/science/article/pii/S0016703709005055>.
- [106] “Observation of two-neutrino double electron capture in ^{124}Xe with XENON1T”. In: *Nature* 568.7753 (2019), pp. 532–535. ISSN: 1476-4687. DOI: 10.1038/s41586-019-1124-4. URL: <https://doi.org/10.1038/s41586-019-1124-4>.

- [107] D S Akerib et al. “Search for two neutrino double electron capture of ^{124}Xe and ^{126}Xe in the full exposure of the LUX detector”. In: *Journal of Physics G: Nuclear and Particle Physics* 47.10 (2020), p. 105105. DOI: 10.1088/1361-6471/ab9c2d. URL: <https://doi.org/10.1088/1361-6471/ab9c2d>.
- [108] E. Aprile et al. “Projected WIMP sensitivity of the XENONnT dark matter experiment”. In: *Journal of Cosmology and Astroparticle Physics* 2020.11 (2020), pp. 031–031. DOI: 10.1088/1475-7516/2020/11/031. URL: <https://doi.org/10.1088/1475-7516/2020/11/031>.
- [109] Jouni Suhonen. “Double beta decays of ^{124}Xe investigated in the QRPA framework”. In: *Journal of Physics G: Nuclear and Particle Physics* 40.7 (2013), p. 075102. DOI: 10.1088/0954-3899/40/7/075102. URL: <https://doi.org/10.1088/0954-3899/40/7/075102>.
- [110] Pekka Pirinen and Jouni Suhonen. “Systematic approach to β and $2\nu\beta\beta$ decays of mass $A = 100 - 136$ nuclei”. In: *Phys. Rev. C* 91 (5 2015), p. 054309. DOI: 10.1103/PhysRevC.91.054309. URL: <https://link.aps.org/doi/10.1103/PhysRevC.91.054309>.
- [111] E.A. Coello Pérez, J. Menéndez, and A. Schwenk. “Two-neutrino double electron capture on ^{124}Xe based on an effective theory and the nuclear shell model”. In: *Physics Letters B* 797 (2019), p. 134885. ISSN: 0370-2693. DOI: <https://doi.org/10.1016/j.physletb.2019.134885>. URL: <https://www.sciencedirect.com/science/article/pii/S0370269319305994>.
- [112] E. Aprile et al. “The XENON1T dark matter experiment”. In: *The European Physical Journal C* 77.12 (2017). ISSN: 1434-6052. DOI: 10.1140/epjc/s10052-017-5326-3. URL: <http://dx.doi.org/10.1140/epjc/s10052-017-5326-3>.
- [113] D.-M. Mei et al. “Measuring double-electron capture with Liquid Xenon Experiments”. In: *Phys. Rev. C* 89 (1 2014), p. 014608. DOI: 10.1103/PhysRevC.89.014608. URL: <https://link.aps.org/doi/10.1103/PhysRevC.89.014608>.
- [114] Frederick Gray et al. “Cosmic Ray Muon Flux at the Sanford Underground Laboratory at Homestake”. In: *Nuclear Instruments Methods in Physics Research Section A-accelerators Spectrometers Detectors and Associated*

- Equipment - NUCL INSTRUM METH PHYS RES A* 638 (2011). DOI: 10.1016/j.nima.2011.02.032.
- [115] D.-M. Mei and A. Hime. “Muon-induced background study for underground laboratories”. In: *Physical Review D* 73.5 (2006). ISSN: 1550-2368. DOI: 10.1103/physrevd.73.053004. URL: <http://dx.doi.org/10.1103/PhysRevD.73.053004>.
- [116] *Gas Encyclopedia - Air Liquide*. <https://encyclopedia.airliquide.com/xenon>. Accessed: 2021-04-15.
- [117] D. S. Akerib et al. “Projected sensitivity of the LUX-ZEPLIN experiment to the $0\nu\beta\beta$ decay of ^{136}Xe ”. In: *Physical Review C* 102.1 (2020). ISSN: 2469-9993. DOI: 10.1103/physrevc.102.014602. URL: <http://dx.doi.org/10.1103/PhysRevC.102.014602>.
- [118] D. S. Akerib et al. “Projected WIMP sensitivity of the LUX-ZEPLIN dark matter experiment”. In: *Physical Review D* 101.5 (2020). ISSN: 2470-0029. DOI: 10.1103/physrevd.101.052002. URL: <http://dx.doi.org/10.1103/PhysRevD.101.052002>.
- [119] J. Dobson, C. Ghag, and L. Manenti. “Ultra-low background mass spectrometry for rare-event searches”. In: *Nuclear Instruments and Methods in Physics Research Section A: Accelerators, Spectrometers, Detectors and Associated Equipment* 879 (2018), pp. 25–30. ISSN: 0168-9002. DOI: <https://doi.org/10.1016/j.nima.2017.10.014>. URL: <https://www.sciencedirect.com/science/article/pii/S0168900217310513>.
- [120] D. S. Akerib et al. “The LUX-ZEPLIN (LZ) radioactivity and cleanliness control programs”. In: *The European Physical Journal C* 80.11 (2020). ISSN: 1434-6052. DOI: 10.1140/epjc/s10052-020-8420-x. URL: <http://dx.doi.org/10.1140/epjc/s10052-020-8420-x>.
- [121] D.S. Akerib et al. “Measurement of the gamma ray background in the Davis cavern at the Sanford Underground Research Facility”. In: *Astroparticle Physics* 116 (2020), p. 102391. ISSN: 0927-6505. DOI: 10.1016/j.astropartphys.2019.102391. URL: <http://dx.doi.org/10.1016/j.astropartphys.2019.102391>.

- [122] M.-M. Bé et al. *Table of Radionuclides*. Pavillon de Breteuil, F-92310 Sèvres, France: Bureau International des Poids et Mesures. URL: http://www.nucleide.org/DDEP_WG/Nuclides/I-125_tables.pdf.
- [123] M.-M. Bé et al. *Table of Radionuclides*. Pavillon de Breteuil, F-92310 Sèvres, France: Bureau International des Poids et Mesures. URL: http://www.nucleide.org/DDEP_WG/Nuclides/Rn-222_tables.pdf.
- [124] M.-M. Bé et al. *Table of Radionuclides*. Pavillon de Breteuil, F-92310 Sèvres, France: Bureau International des Poids et Mesures. URL: http://www.nucleide.org/DDEP_WG/Nuclides/Rn-220_tables.pdf.
- [125] V. Balek. “Emanation thermal analysis: The present state and perspectives”. In: *Journal of Thermal Analysis and Calorimetry* 20 (2 1981), pp. 495–518. ISSN: 1388-6150,1572-8943. DOI: 10.1007/bf01912901. URL: <http://doi.org/10.1007/bf01912901>.
- [126] D. S. Akerib et al. “The LUX-ZEPLIN (LZ) radioactivity and cleanliness control programs”. In: *The European Physical Journal C* 80.11 (2020). ISSN: 1434-6052. DOI: 10.1140/epjc/s10052-020-8420-x. URL: <http://dx.doi.org/10.1140/epjc/s10052-020-8420-x>.
- [127] M.-M. Bé et al. *Table of Radionuclides*. Pavillon de Breteuil, F-92310 Sèvres, France: Bureau International des Poids et Mesures. URL: http://www.nucleide.org/DDEP_WG/Nuclides/Pb-214_tables.pdf.
- [128] M.-M. Bé et al. *Table of Radionuclides*. Pavillon de Breteuil, F-92310 Sèvres, France: Bureau International des Poids et Mesures. URL: http://www.nucleide.org/DDEP_WG/Nuclides/Pb-212_tables.pdf.
- [129] M.-M. Bé et al. *Table of Radionuclides*. Pavillon de Breteuil, F-92310 Sèvres, France: Bureau International des Poids et Mesures. URL: http://www.nucleide.org/DDEP_WG/Nuclides/Pb-210_tables.pdf.
- [130] R. Heaton et al. “Neutron production from thick-target (α,n) reactions”. In: *Nuclear Instruments and Methods in Physics Research Section A: Accelerators, Spectrometers, Detectors and Associated Equipment* 276.3 (1989), pp. 529–538. ISSN: 0168-9002. DOI: [https://doi.org/10.1016/0168-9002\(89\)90579-2](https://doi.org/10.1016/0168-9002(89)90579-2). URL: <https://www.sciencedirect.com/science/article/pii/0168900289905792>.

- [131] Jun Chen. “Nuclear Data Sheets for A=39”. In: *Nuclear Data Sheets* 149 (2018), pp. 1–251. ISSN: 0090-3752. DOI: <https://doi.org/10.1016/j.nds.2018.03.001>. URL: <https://www.sciencedirect.com/science/article/pii/S0090375218300437>.
- [132] M.-M. Bé et al. *Table of Radionuclides*. Pavillon de Breteuil, F-92310 Sèvres, France: Bureau International des Poids et Mesures. URL: http://www.nucleide.org/DDEP_WG/Nuclides/Kr-85_tables.pdf.
- [133] A.I. Bolozdynya et al. “A chromatographic system for removal of radioactive ^{85}Kr from xenon”. In: *Nuclear Instruments and Methods in Physics Research Section A: Accelerators, Spectrometers, Detectors and Associated Equipment* 579.1 (2007). Proceedings of the 11th Symposium on Radiation Measurements and Applications, pp. 50–53. ISSN: 0168-9002. DOI: <https://doi.org/10.1016/j.nima.2007.04.011>. URL: <https://www.sciencedirect.com/science/article/pii/S0168900207005700>.
- [134] J. B. Albert et al. “Improved measurement of the $2\nu\beta\beta$ half-life of ^{136}Xe with the EXO-200 detector”. In: *Phys. Rev. C* 89 (1 2014), p. 015502. DOI: [10.1103/PhysRevC.89.015502](https://doi.org/10.1103/PhysRevC.89.015502). URL: <https://link.aps.org/doi/10.1103/PhysRevC.89.015502>.
- [135] Matthew Redshaw et al. “Mass and Double-Beta-Decay Q Value of ^{136}Xe ”. In: *Physical review letters* 98 (2007), p. 053003. DOI: [10.1103/PhysRevLett.98.053003](https://doi.org/10.1103/PhysRevLett.98.053003).
- [136] John N Bahcall and Carlos Peña-Garay. “Solar models and solar neutrino oscillations”. In: *New Journal of Physics* 6 (2004), pp. 63–63. ISSN: 1367-2630. DOI: [10.1088/1367-2630/6/1/063](https://doi.org/10.1088/1367-2630/6/1/063). URL: <http://dx.doi.org/10.1088/1367-2630/6/1/063>.
- [137] Jiunn-Wei Chen et al. “Low-energy electronic recoil in xenon detectors by solar neutrinos”. In: *Physics Letters B* 774 (2017), pp. 656–661. ISSN: 0370-2693. DOI: [10.1016/j.physletb.2017.10.029](https://doi.org/10.1016/j.physletb.2017.10.029). URL: <http://doi.org/10.1016/j.physletb.2017.10.029>.
- [138] D. Akimov et al. “Observation of coherent elastic neutrino-nucleus scattering”. In: *Science* 357.6356 (2017), pp. 1123–1126. ISSN: 1095-9203. DOI: <https://doi.org/10.1126/science.1257479>.

- 10.1126/science.aao0990. URL: <http://dx.doi.org/10.1126/science.aao0990>.
- [139] Athoy et al. *DMCalc Tutorial: A package for dark matter physics calculations*. Internal LZ note. URL: <https://docs.google.com/presentation/d/1h4vPOMm-8PWiq5oPH4HYWwVuC5m0NJWgP2Qdqa10f6w/edit#slide=id.p>.
- [140] D. S. Akerib et al. “Calibration, event reconstruction, data analysis, and limit calculation for the LUX dark matter experiment”. In: *Phys. Rev. D* 97 (10 2018), p. 102008. DOI: 10.1103/PhysRevD.97.102008. URL: <https://link.aps.org/doi/10.1103/PhysRevD.97.102008>.
- [141] The LZ Collaboration et al. *Projected sensitivities of the LUX-ZEPLIN (LZ) experiment to new physics via low-energy electron recoils*. 2021. arXiv: 2102.11740 [hep-ex].
- [142] Wolfgang A. Rolke, Angel M. López, and Jan Conrad. “Limits and confidence intervals in the presence of nuisance parameters”. In: *Nuclear Instruments and Methods in Physics Research Section A: Accelerators, Spectrometers, Detectors and Associated Equipment* 551.2-3 (2005), pp. 493–503. ISSN: 0168-9002. DOI: 10.1016/j.nima.2005.05.068. URL: <http://dx.doi.org/10.1016/j.nima.2005.05.068>.
- [143] J. Lundberg et al. “Limits, discovery and cut optimization for a Poisson process with uncertainty in background and signal efficiency: TRolke 2.0”. In: *Computer Physics Communications* 181.3 (2010), pp. 683–686. ISSN: 0010-4655. DOI: 10.1016/j.cpc.2009.11.001. URL: <http://dx.doi.org/10.1016/j.cpc.2009.11.001>.
- [144] E. Aprile et al. “Energy resolution and linearity of XENON1T in the MeV energy range”. In: *The European Physical Journal C* 80.8 (2020). ISSN: 1434-6052. DOI: 10.1140/epjc/s10052-020-8284-0. URL: <http://dx.doi.org/10.1140/epjc/s10052-020-8284-0>.
- [145] D. S. Akerib et al. “Signal yields, energy resolution, and recombination fluctuations in liquid xenon”. In: *Physical Review D* 95.1 (2017). ISSN: 2470-0029. DOI: 10.1103/physrevd.95.012008. URL: <http://dx.doi.org/10.1103/PhysRevD.95.012008>.

Appendix A

Parameters of a root tree

N/A = not applicable

Table A.1: List of the variables and the respective type, units and meaning, of a root tree.

Type	Name	Units	Description
Int	iTreeNum	N/A	Tree number
Int	iNumEvtsPerTree	N/A	Number of events per tree
Int	iEvtN	N/A	Event number
UInt	fBits	N/A	Number of bits
String	fString	N/A	Isotope name
Bool	bIsUearly	N/A	Belongs or not to the early chain of ^{238}U
Float	fPrimaryParX_cm; fPrimaryParY_cm; fPrimaryParZ_cm	cm	Starting position of the primary particle
Double	fLXeTime_ns	ns	Time of the first interaction in the active region (relatively to the start of the event)
Float	fLXeS1cTot_phe	phe	Total corrected S1 signal in the active region

Continued on next page

TableA.1 – continued from previous page

Type	Name	Units	Description
Float	fLXeS1c_phe	phe	Corrected S1 signal in the active region
Float	fLXeS2c_phe	phe	Corrected S2 signal in the active region
Float	fLXeS2_phe	phe	Total S2 signal in the active region
Float	fLXeEDepER_keV	keV	Total deposited energy in the active region in the form of ERs
Float	fLXeEDepNR_keV	keV	Total deposited energy in the active region in the form of NRs
Float	fLXeEDepNR_frac800us	keV	Total deposited energy in the active region in the form of NRs, within a 800 μ s window from the first interaction
Float	fLXeEDepER_frac800us	keV	Total deposited energy in the active region in the form of ERs, within a 800 μ s window from the first interaction
Float	fLXeX_cm; fLXeY_cm; fLXeZ_cm; fLXeR_cm;	cm	Energy weighted average position of the interactions in the active region
Float	fLXeSigmaR_cm	cm	Energy weighted sigma of the interactions in the radial direction in the active region
Float	fLXeSigmaZ_cm	cm	Energy weighted sigma of the interaction in the z direction in the active region
Float	fLXeDeltaZ_cm	cm	Maximum vertical separation between interactions in the active region
Float	fRFRS1c_phe	phe	Corrected S1 signal in the RFR
Float	fRFRER_keV	keV	Total deposited energy in the form of ERs in the RFR

Continued on next page

TableA.1 – continued from previous page

Type	Name	Units	Description
Float	fRFRNR_keV	keV	Total deposited energy in the form of NRs in the RFR
Float	fRFREDepNR_frac800us	keV	Total deposited energy in the RFR in the form of NRs, within a 800 μ s window from the first interaction in the active region
Float	fRFREDepER_frac800 μ s	keV	Total deposited energy in the RFR in the form of ERs, within a 800 μ s window from the first interaction in the active region
Double	fSkinTime_ns	ns	Time of the first interaction in the skin region (relatively to the start of the event)
Float	fSkinEDep_keV	keV	Total deposited energy in the skin region
Float	fSkinEDepNR_frac800us	keV	Total deposited energy in the skin region in the form of NRs, within a 800 μ s window
Float	fSkinEDepER_frac800us	keV	Total deposited energy in the skin region in the form of ERs, within a 800 μ s window
Float	fSkinS1_phe	phe	Total S1 area in the skin region
Float	fSkinX_cm; fSkinY_cm; fSkinZ_cm; fSkinR_cm	cm	Energy weighted average position of the interactions in the skin region
Float	fSkinSigmaR_cm	cm	Energy weighted sigma of the interaction in the radial direction in the skin region
Float	fSkinSigmaZ_cm	cm	Energy weighted sigma of the interaction in the z direction in the skin region

Continued on next page

TableA.1 – continued from previous page

Type	Name	Units	Description
Double	fODTime_ns	ns	Time of the first interaction in the OD (relatively to the start of the event)
Float	fODX_cm; fODY_cm; fODZ_cm;	cm	Energy weighted average position of the interactions in the OD
Float	fODSigmaX_cm; fOD- SigmaY_cm; fODSig- maZ_cm	cm	Energy weighted sigma position of the interaction in the OD
Float	fODEDep_keV	keV	Total deposited energy in the OD
Float	fOD_frac800us	N/A	Fraction of the total energy deposited in the OD within a $800\mu\text{s}$ window from the first interaction in the active region